2018

# Nano-structure-based optical sensors fabrication and validation to gas sensing applications

Shawana Tabassum
*Iowa State University*

# Nano-structure-based optical sensors fabrication and validation to gas sensing applications

by

**Shawana Tabassum**

A dissertation submitted to the graduate faculty

in partial fulfillment of the requirements for the degree of

DOCTOR OF PHILOSOPHY

Major: Electrical Engineering

Program of Study Committee:
Ratnesh Kumar, Co-major Professor
Liang Dong, Co-major Professor
Robert J. Weber
Long Que
Meng Lu

The student author, whose presentation of the scholarship herein was approved by the program of study committee, is solely responsible for the content of this dissertation. The Graduate College will ensure this dissertation is globally accessible and will not permit alterations after a degree is conferred.

Iowa State University

Ames, Iowa

2018

# TABLE OF CONTENTS

Page

# LIST OF FIGURES

Page

# LIST OF TABLES

## NOMENCLATURE

| | |
|---|---|
| ATR | Attenuated Total Reflection |
| ChG | Chalcogenide |
| DFT | Density Function Theory |
| DI | Deionized |
| EBL | Electron Beam Lithography |
| EDS | Energy Dispersive Spectroscopy |
| EM | Electro Magnetic |
| FBG | Fiber Bragg Grating |
| FIB | Focused Ion Beam |
| FP | Fabry P*é*rot |
| FTIR | Fourier Transform Infrared |
| GMR | Guided Mode Resonance |
| GO | Graphene Oxide |
| HCPCF | Hollow Core Photonic Crystal Fiber |
| IPA | Iso Propyl Alcohol |
| ITO | Indium Tin Oxide |
| LPG | Long Period Grating |
| LOF | Lab On Fiber |
| LSPR | Localized Surface Plasmon Resonance |
| MFC | Mass Flow Controller |
| NIL | Nano-Imprint Lithography |
| PCA | Principal Component Analysis |

| | |
|---|---|
| PCF | Photonic Crystal Fiber |
| PDMS | Polydimethylsiloxane |
| PMMA | Poly (methyl methacrylate) |
| PVC | Polyvinylchloride |
| RA | Rayleigh Anomaly |
| RCWA | Rigorous Coupled Wave Analysis |
| RI | Refractive Index |
| RIU | Refractive Index Unit |
| RS | Reflection Spectroscopy |
| SA | Self Assembly |
| SEM | Scanning Electron Microscopy |
| SERS | Surface Enhanced Raman Spectroscopy |
| SPP | Surface Plasmon Polariton |
| SPR | Surface Plasmon Resonance |
| TM | Transverse Magnetic |
| TE | Transverse Electric |
| $TiO_2$ | Titanium Di-Oxide |
| UV | Ultraviolet |
| VOC | Volatile Organic Compound |
| WGM | Whispering Gallery Mode |
| ZPUA | Zipcone UA |
| 2D | Two- Dimensional |
| 3D | Three- Dimensional |

## ACKNOWLEDGMENTS

I have been fortunate to be a graduate student and meet so many lovely people at Iowa State University during my doctoral studies. I would like to thank all the people who have helped and supported me in this eventful journey.

First of all, I want to express my deepest gratitude to my advisors Professors Ratnesh Kumar and Liang Dong for their guidance and continuous encouragement throughout my Ph.D. journey. I would also like to specially thank Professor Ratnesh Kumar for his invaluable support and encouragement during my harsh times. I will be forever grateful for his strong support, guidance, and encouragement in my professional and personal life.

Thanks to all members of my thesis committee, Dr. Long Que, Dr. Robert J. weber, and Dr. Meng Lu for discussing my thesis and providing invaluable feedback to make it better.

I would like to thank my colleagues at Laboratory for Mems and Biochips research group, Dr. Qiugu Wang, Dr. Md Azahar Ali, Yifei Wang, Seval Oren, Yueyi Jiao, and my colleagues at Embedded Software, Sensors, Networks, Cyberphysical and Energy Laboratory, Bhuwan Kashyap, Madhav Pathak, Anupam Bhar, Alaa Al-Ghazo and Souvik Kundu for their friendship and assistance. It was a great pleasure to be included in this research team. I would also like to thank Leland Harker for his strong help in terms of manufacturing parts and circuits. I wish you all the best in all aspects of your life.

I would like to acknowledge the funding support from U.S. National Science Foundation under Grant CCF-1331390 and Grant IIP-1602089 and ISU's Regents Innovation Fund.

My heartfelt thanks go to my beloved parents, Md. Golam Nobi and Sharmin Sikander, for taking care of, supporting, and encouraging me in difficulties ever since the day I was born. Special thanks to my sister, Sadaf Tarannum and my brother, Shahroz Nobi, for making me laugh and giving me support.

## ABSTRACT

We present three different nano-resonant structures (nanoposts, nanoholes etc.) fabricated on either bulk substrate or micron size tip of optical fiber and one graphene oxide coated glass substrate for gas detection in visible or mid-infrared region of electromagnetic spectrum. Nanostructures provide an efficient way to control and manipulate light at nanoscale paving the way for the development of reliable, sensitive, selective and miniaturized gas sensing technologies. Moreover, the inherent light guiding property of optical fiber over long distances, their microscopic cross-section, their efficient integration capabilities with gas absorption coatings and mechanical flexibility make them suitable for remote sensing applications. The three nanostructure-based gas sensing techniques are based on the detection of surface plasmon resonance (SPR) wavelength shifts, guided mode resonance (GMR) wavelength shifts, and Rayleigh anomaly (RA) mode intensity variations. The SPR and GMR based sensors operate in the visible region of light spectrum. Later, we also integrate a heater with the GMR-based fiber-tip sensor to realize a reusable gas sensor having tunable sensor recovery time. The RA-based sensor is realized by solvent-casting of chalcogenide glass to work as mid-infrared optical resonator. Further, we utilize the dynamic variations in infrared values of graphene oxide in response to gas to realize a gas sensor.

First, we present a high-sensitivity gas sensor based on plasmonic crystal incorporating a thin layer of graphene oxide. The presented plasmonic crystal is formed by an array of polymeric nanoposts with gold disks at the top and perforated nanoholes in a gold thin film at the bottom. The thin coating of graphene oxide assembled on the top surface of mushroom plasmonic nanostructures works as the gas absorbent material for the

sensor. The optical response of the plasmonic nanostructure is altered due to different concentrations of gas absorbed in the graphene oxide coating. By coating the surface of multiple identical plasmonic crystals with different thicknesses of graphene oxide layer, the effective refractive index of the graphene oxide layer on each plasmonic crystal will be differently modulated when responding to a specific gas. This allows identifying various gas species using the principal component analysis-based pattern recognition algorithm. The present plasmonic nanostructure offers a promising approach to detect various volatile organic compounds.

Second, we report a simple yet efficient method of transferring nanopatterns to optical fiber tip. We have also demonstrated a $TiO_2$ coated GMR structure which is sensitive to changes in surrounding refractive index and provides shifts in its resonant wavelength. The GMR sensor at the fiber tip is also demonstrated to work as a gas sensor by coating it with a thin layer of graphene oxide. This simplified and rapid nanostructuring at fiber tip can contribute to remote sensing applications through the insertion of the nanopatterned fiber tips into aqueous and gaseous analytes in regions otherwise inaccessible.

Third, we present the first heater integrated nanostructured optical fiber of 200 μm diameter to realize a high-sensitivity and reusable fiber-optic gas sensor. In our GMR-enabled fiber-optic gas sensor, resonance shifts upon the adsorption of the analytes on the graphene oxide (GO) coated sensor surface. For repeated use of this sensor, a regeneration of the sensor surface is required by a complete desorption of the analyte molecules from the GO layer. In our presented design, this has been achieved by the integration of a controllable heater at the fiber tip.

Fourth, we present a straightforward analysis based on the maximum and minimum envelopes of the reflection spectra to dynamically investigate the changes in complex refractive index of graphene oxide in response to gases. The performance of graphene oxide -based gas sensors is strongly influenced by the variations in optical properties of graphene oxide when exposed to gas. The presented method does not require any complex dispersion model as compared to ellipsometry. Accordingly, the technique we employ can be leveraged to reliably evaluate the optical performance of any graphene oxide-based gas sensors in a simpler manner, when compared to ellipsometry. Furthermore, the accuracy of the derived values of complex refractive index of the graphene oxide layer has been confirmed by comparing with literature.

Finally, we report the development of a first of a kind planar resonant structure that enhances the mid-IR absorption by the analyte adsorbed on its surface, enabling highly sensitive and selective label-free detection of gas and/or biomarkers. Chalcogenide glasses ($As_2S_3$) are promising for infrared photonics owing to their transparency in visible to far infrared, where various biomolecules and gases have their characteristic absorption lines, arising from rotational-vibrational transitions. Here we present the proposed design of a nanoscale tunable planar mid-IR optical resonator, realized by solvent-casting of $As_2S_3$. Our technique of preparing nanostructure having resonance at mid-IR enables the realization of mid-IR bio as well as gas sensors.

# CHAPTER 1. GENERAL INTRODUCTION

## 1.1 Background

The continuous demand for precise detection and discrimination of large classes of bio as well as gas molecules has led to the development of more sophisticated and reliable sensing devices. To meet this demand, novel photonic devices functionalized with specific materials are being exploited. Such photonic devices utilize a variety of nanostructures for effective detection and discrimination of molecules, such as plasmonics, photonic crystals, surface enhanced Raman scattering, meta-surfaces. Moreover, lab-on-a-chip platform has been realized by combining miniaturized optical sensors with microfluidics. Thus, researchers are encouraged to combine the nanophotonic sensors with an analyte recognition coating on a conventional or non-conventional fiber-optic platform, aimed at developing high-performance miniaturized sensors operating at visible to infrared region of electromagnetic spectrum.

The next section gives details of relevant work, including: 1. Nanostructured planar substrates for optical gas sensor design and 2. Fiber-optic gas sensors design.

## 1.2 Nanostructured Planar Substrates for Optical Gas Sensor Design

Recent advances in the fabrication of materials play a substantial role in modifying and enhancing the existing sensing techniques. Micro- and nano-structured materials enable efficient control of light at nanoscale resulting in sensors with increased sensitivities, multiplexing capabilities, or both [1].

### 1.2.1 Surface Plasmon-Based Sensing Substrates

Surface plasmon resonance (SPR) probes the changes in the bulk refractive index of the surrounding medium. SPR based optical sensors are widely explored and a variety of geometries utilizing Bragg grating and Kretschmann configuration have been developed to

excite SPR [2-4]. In addition, multilayered metallic nanostructures have been demonstrated to provide improved SPR responses [5]. In contrast, localized surface plasmon resonance (LSPR) is sensitive to small changes in local dielectric environment immediately surrounding a plasmonic nanoparticle [6- 9]. These changes in dielectric environment are in turn transduced to spectral shifts. By optimizing the size and shape of nanostructures, the spectral properties can be altered, thus making the resulting structure extremely sensitive to surface binding events. Various well-controlled shapes such as nanoholes, nanowells, nanorods, nanoshells, nanostars and other nanocrystalline shapes have been employed to tailor LSPR absorption from visible to infrared regions, some of which are illustrated in Figure 1.1. The plasmonic surface is functionalized with an analyte recognition coating which is next exposed to the analyte. The specific binding of the target analyte, as dictated by the selectivity of the recognition layer coated on the plasmonic surface, changes the local refractive index adjacent to the plasmonic surface, which is then measured as a modulation in the wavelength-dependent optical properties of the structure.

### 1.2.2 Diffraction Grating-Based Sensing Substrates

Diffraction gratings are another class of optical sensors that are widely used to probe interactions occurring on the surface of or within the grating material [12, 13]. Grating-based SPR sensors has been applied for gas detection. A metal grating type configuration is attractive relative to the prism coupling, because it eliminates the need of the prism that couples the incident beam to the surface oscillation on the metal [14].

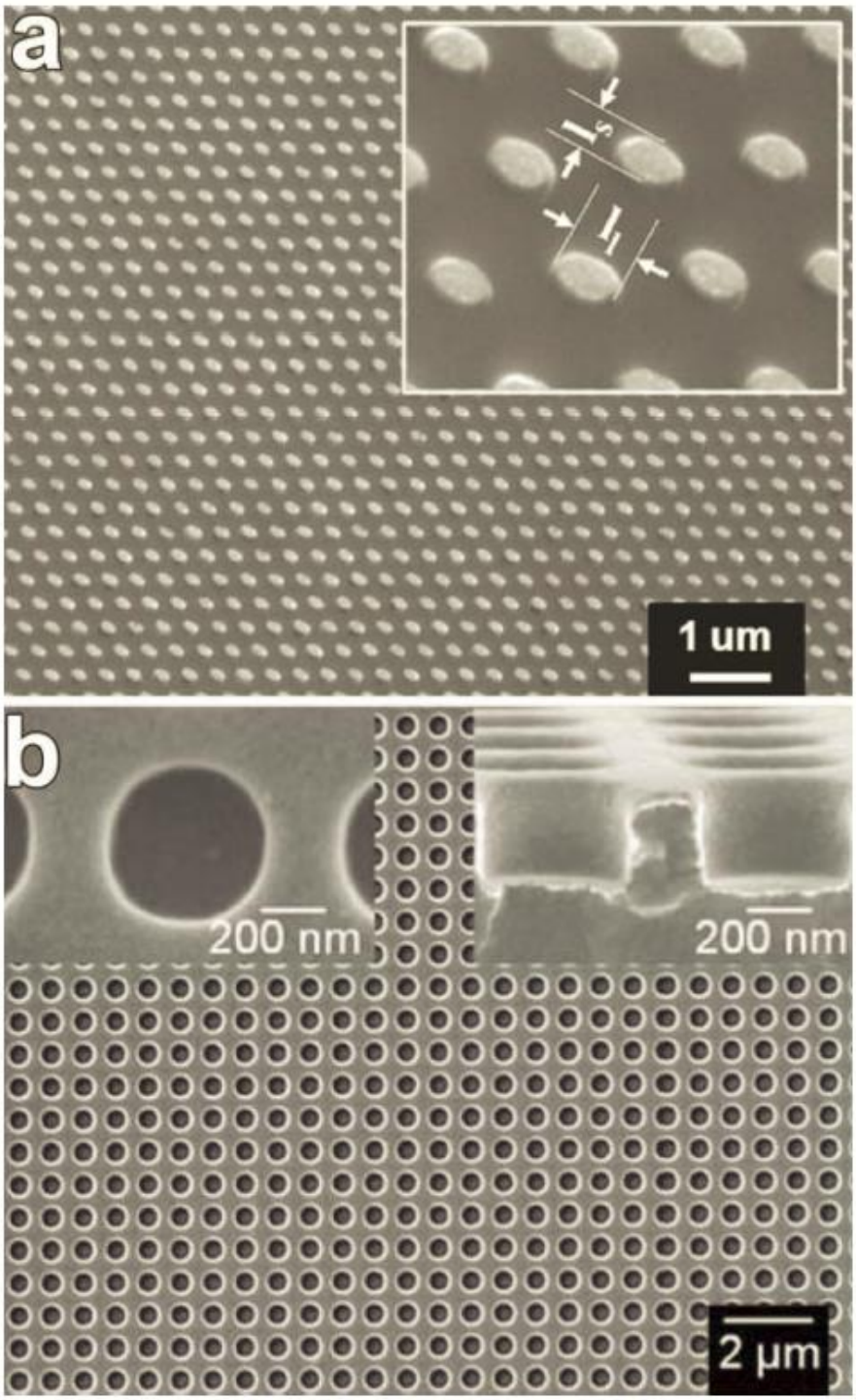


Fig. 1.1: *(a) Array of elliptical Au nanodisks on a glass wafer; inset shows higher magnification and the aspect ratio of the nanodisks [10]. (b) Scanning electron micrographs of a nanowell plasmonic crystal [11]. Left inset: Top view showing approximate nanowell diameter. Right inset: Cross-sectional view showing nanowell depth and continuous Au coverage on the surface.*

Guided Mode Resonance (GMR) is another optical resonance phenomenon where a diffracted order of grating excites a guided mode of a waveguide [15]. The GMR structure consists of a substrate, incident medium, waveguide layer and grating layer as shown in Figure 1.2a [16]. The guided mode can leak into the grating layer and form a leaky mode. If there is constructive interference between the leaky mode and the reflected light, a sharp reflection peak will be generated, and guided-mode resonance will occur. Thus, under certain phase matching conditions the interference produces a sharp peak in the reflection spectrum or a sharp dip in the transmission spectrum. Owing to the narrow line width, high efficiency [17-19] and sensitivity of the GMR peak towards change in surrounding refractive index (RI), such device is widely used for gas sensing [16], bio-sensing [20,21] and many other applications [22-24]. Guo et al. designed a three-layer AR structure waveguide grating filter to detect organic gases depending on their refractive indices [16]. Generally, when the analyte molecules get attached to the surface of a GMR structure, there is a shift in the resonant peak wavelength which can be monitored using a spectrometer [25, 26]. The wavelength shift is attributed to changes in surrounding RI due to analyte absorption on the sensor surface and this type of scanning method is called wavelength interrogation. Angular or intensity interrogation methods which involve either scanning through different incidence angles [27] or through light intensity also enables sensing capability.

### 1.2.3 Photonic Crystal-Based Sensing Substrates

Photonic crystals are periodic dielectric structures with alternating regions of high and low dielectric constants that has a bandgap thus forbidding propagation of a certain band of light frequencies. This phenomenon can be explained through Bragg's law, $m\lambda = 2\eta d\sin(\theta)$, where m is the diffraction order, $\lambda$ is the wavelength of light, d is the lattice spacing of the material, $\eta$ is the refractive index of the material and $\theta$ is the angle of the

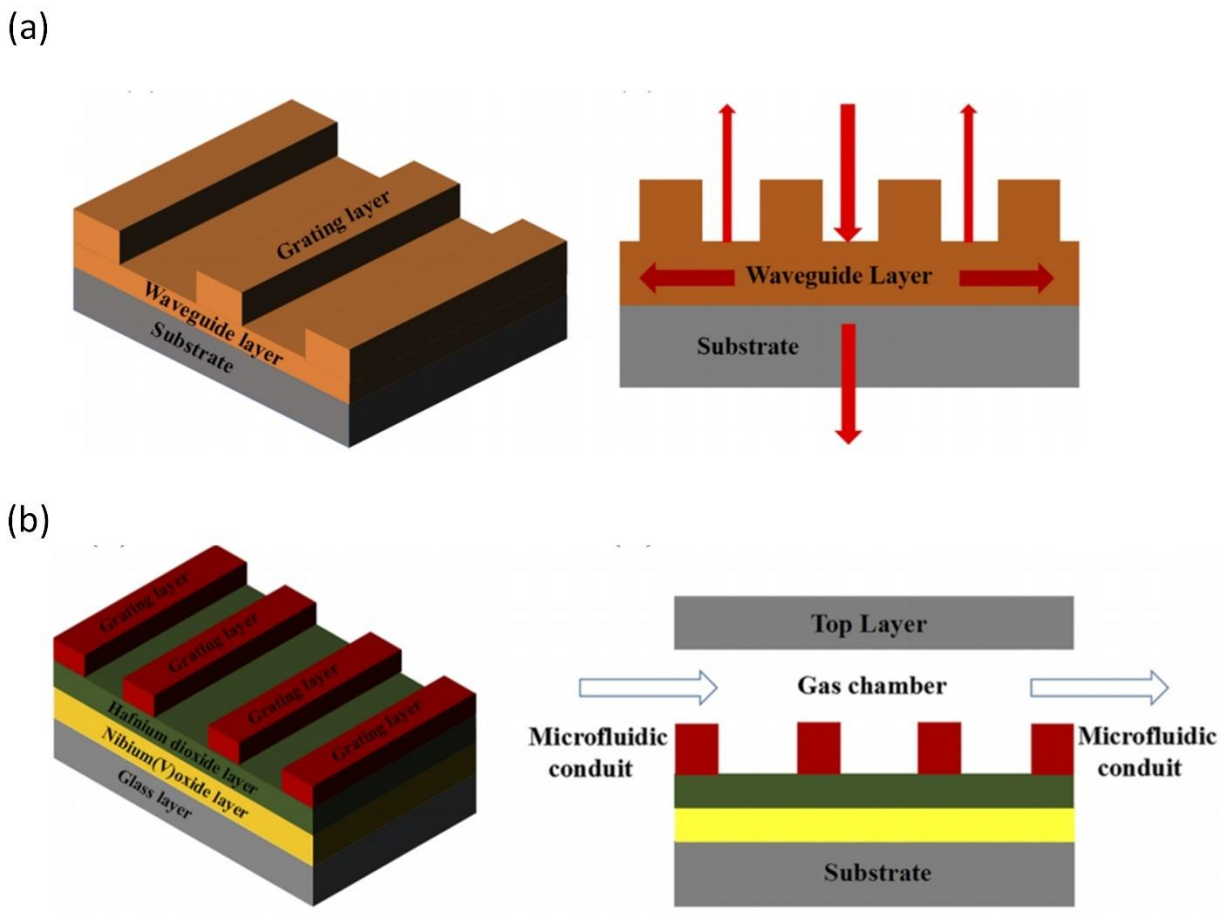


Fig. 1.2: *(a) Structure of a general guided mode resonance filter (left) and formation of guided mode resonance (right). (b) Three-layer AR structure waveguide grating filter (left) and structure of the gas detection chamber (right) [16].*

incident light [1]. 1D porous silicon photonic crystals as shown in Figure 1.3a have been developed by Sailor and coworkers using electrochemical etching of crystalline silicon [28]. Double stacked porous silicon materials have also been used for gas detection (Figure 1.3b) [29,30]. Hybrid photonic crystals have also been employed for the detection of different types of analytes. Alternating layers of $SiO_2$-$TiO_2$ [31], α-$Fe_2O_3$/$WO_3$ nanoparticle films and ZnO/$WO_3$ nanoparticle films [32] have been used for volatile organic solvent detection.

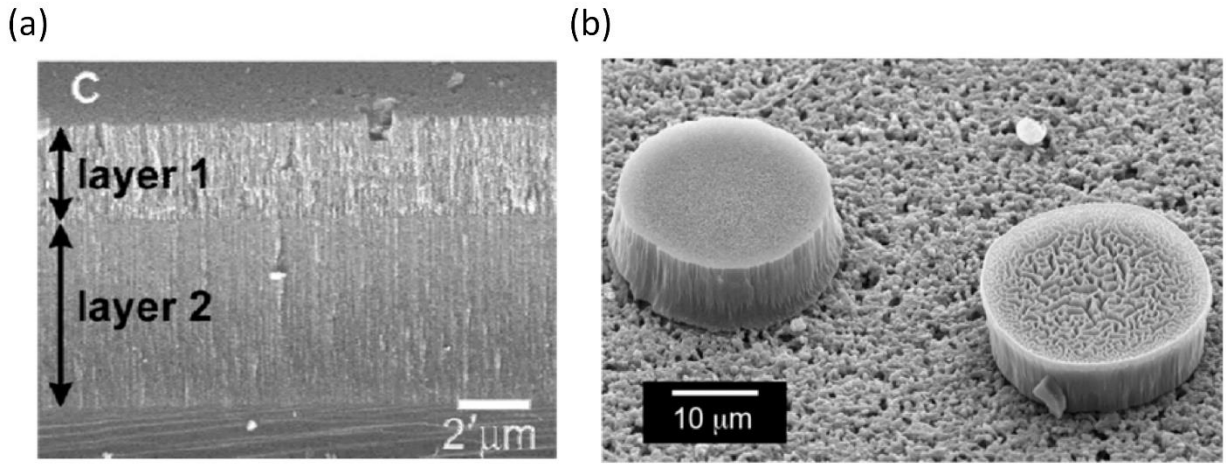


Fig. 1.3: *Scanning electron micrographs of (a) cross-section of 1D porous silicon photonic crystal [28] and (b) multilayered porous silicon surfaces [29].*

### 1.2.4 Photonic Resonator-Based Sensing Substrates

Photonic resonators are another class of sensors that couple light at nano to microscale. Light is coupled into a dielectric material via the evanescent field of a neighboring optical fiber or waveguide. The light wavelengths which are supported by the microcavity are defined by a constructive interference condition of the waves circling around the cavity: $m\lambda = 2\pi r n_{eff}$ where m is a non-zero integer, $\lambda$ is the wavelength of incident light, r is the radius of the resonator, and $n_{eff}$ is the effective refractive index of the optical mode [1]. Such devices are extremely sensitive to binding induced changes in the local dielectric environment which changes the term $n_{eff}$ and hence the resonance wavelength.

There exist many different photonic resonators that support optical frequency modes of the electromagnetic field. Because they are much smaller than conventional resonators for light they are sometimes called microresonators. In a microsphere geometry, light that travels close to the edge of the sphere is continuously reflected back inside the sphere by total internal reflection at the cavity-air interface and is thus trapped inside the sphere [30]. Constructive interference occurs if the circulating beam of light returns to the same point with the same

phase resulting in standing wave formation. Figure 1.4a shows the resonance in a microsphere [31-33]. Dielectric cylinder, ring and disks also support resonance (Figure 1.4b), but light can escape through the top and bottom of the cylinder while the sphere confines light in equatorial as well as in polar directions. Micro-ring resonators thus possess lower quality factor ($Q \sim 10^5$), but because of their planar geometry their fabrication is simpler, faster and more controllable and they require easier optical alignment [34,35]. Thus, they are suitable for practical applications and have been used for multiplexed detection of proteins [36], nucleic acids [37] etc. Microtoroids (Figure 1.4c) can offer exceptionally high quality factors and have high potential for single molecule detection [38,39]. Optical interrogation is however challenging for these devices. Optical fibers can be modified to have a bulge in the middle thus forming optical bottle resonators. The bulge in the middle provides additional confinement of light in the axial direction (Figure 1.4d) [40].

## 1.3 Optical Fibers for Gas Sensor Design

The extraordinary light guiding capabilities of optical fibers along with their microscopic cross-section, biocompatibility and potential for integration with catheters and needles, make them the ideal platform for biosensing as well as gas sensing applications [44]. Depending on the application, the tip, the outer cylindrical surface or holey core/cladding of the optical fiber can be used for the integration of functional materials as illustrated in Figure 1.5.

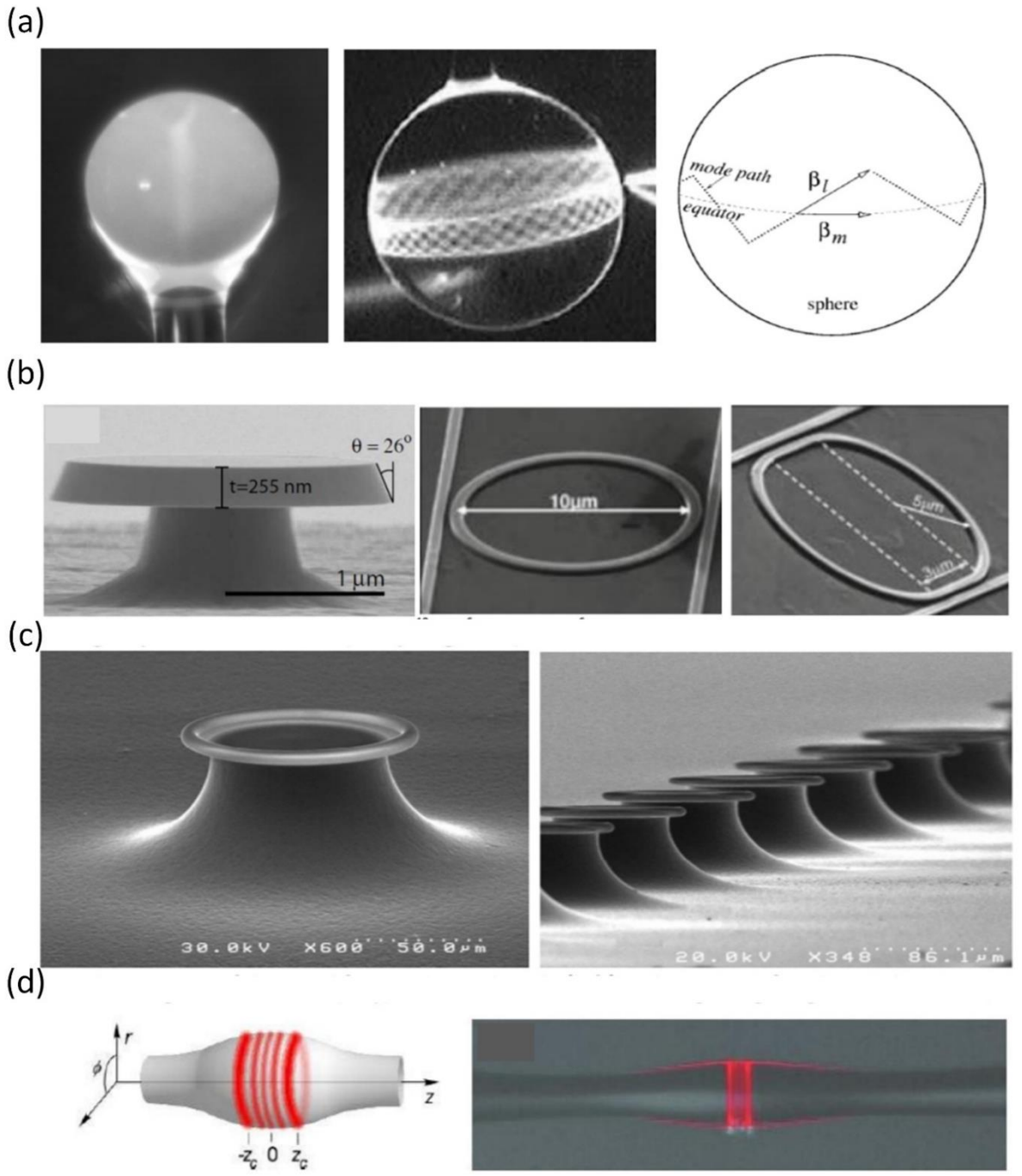


Fig. 1.4: *(a) A silica microsphere resonator with the fiber stem visible underneath the globe [32] (left). A stationary fluorescence pattern representing the intensity of a combination of whispering gallery modes in a 300$\mu$m fused silica microsphere [33] (center) and the geometrical optics approximation to whispering gallery mode propagation [31] (right). (b) Fabricated disk [41], ring [42] and racetrack [42] resonators (from left to right). (c) A toroid microcavity fabricated from a thermal oxide (left) and an array of such toroid microcavities (right) [43]. (d) Optical bottle resonator geometry (left) and a false-color micrograph of a fluorescing resonator doped with erbium ions [40].*

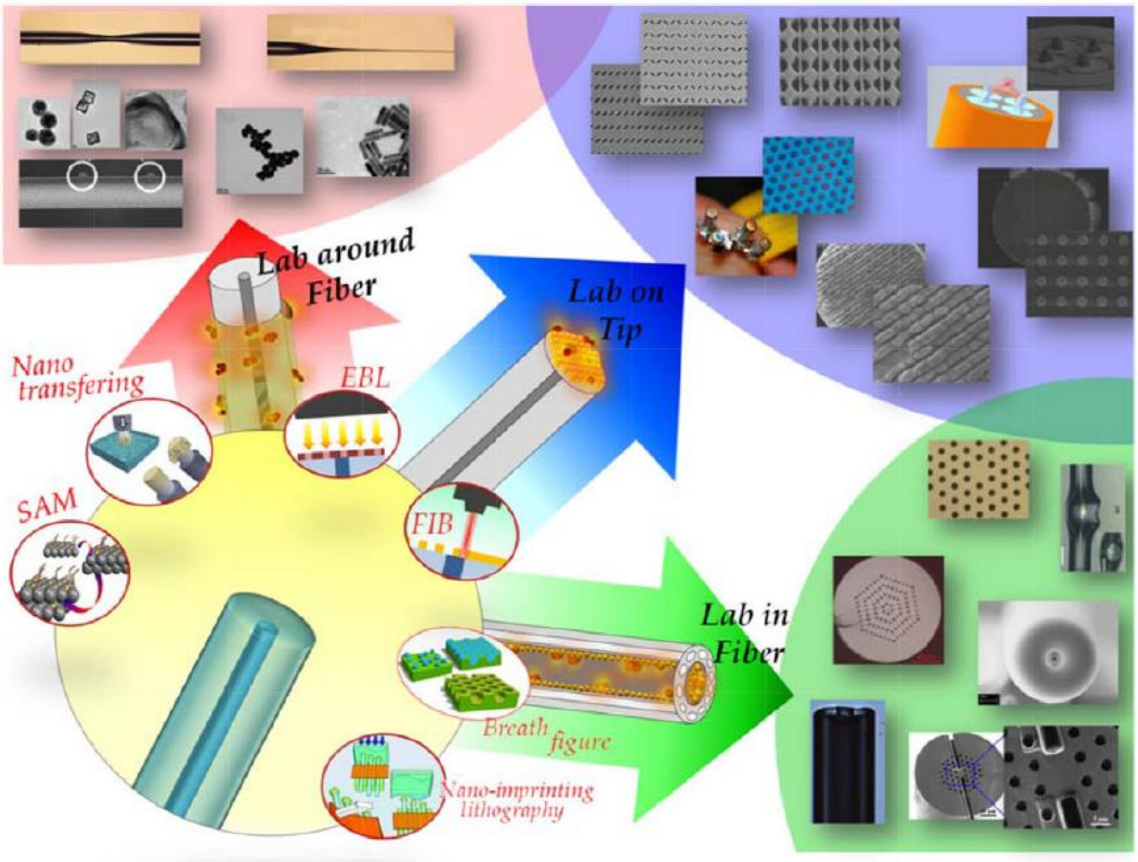


Fig. 1.5: *The lab on fiber paradigm [44]*.

### 1.3.1 Sensing on the Fiber Tip

The flat and micron-sized surface of the tip of the fiber offers promising platform for remote sensing applications. The tip can be easily functionalized with suitable functional materials for specific sensing applications. Fabrication of nanopatterns on the fiber tip are generally classified into two broad categories. The first category includes direct writing approaches wherein nanostructures are directly written on the tip of fiber. Although such fabrication methodologies lead to uniform and repeatable patterns, they impose severe requirements on fiber positioning and handling.

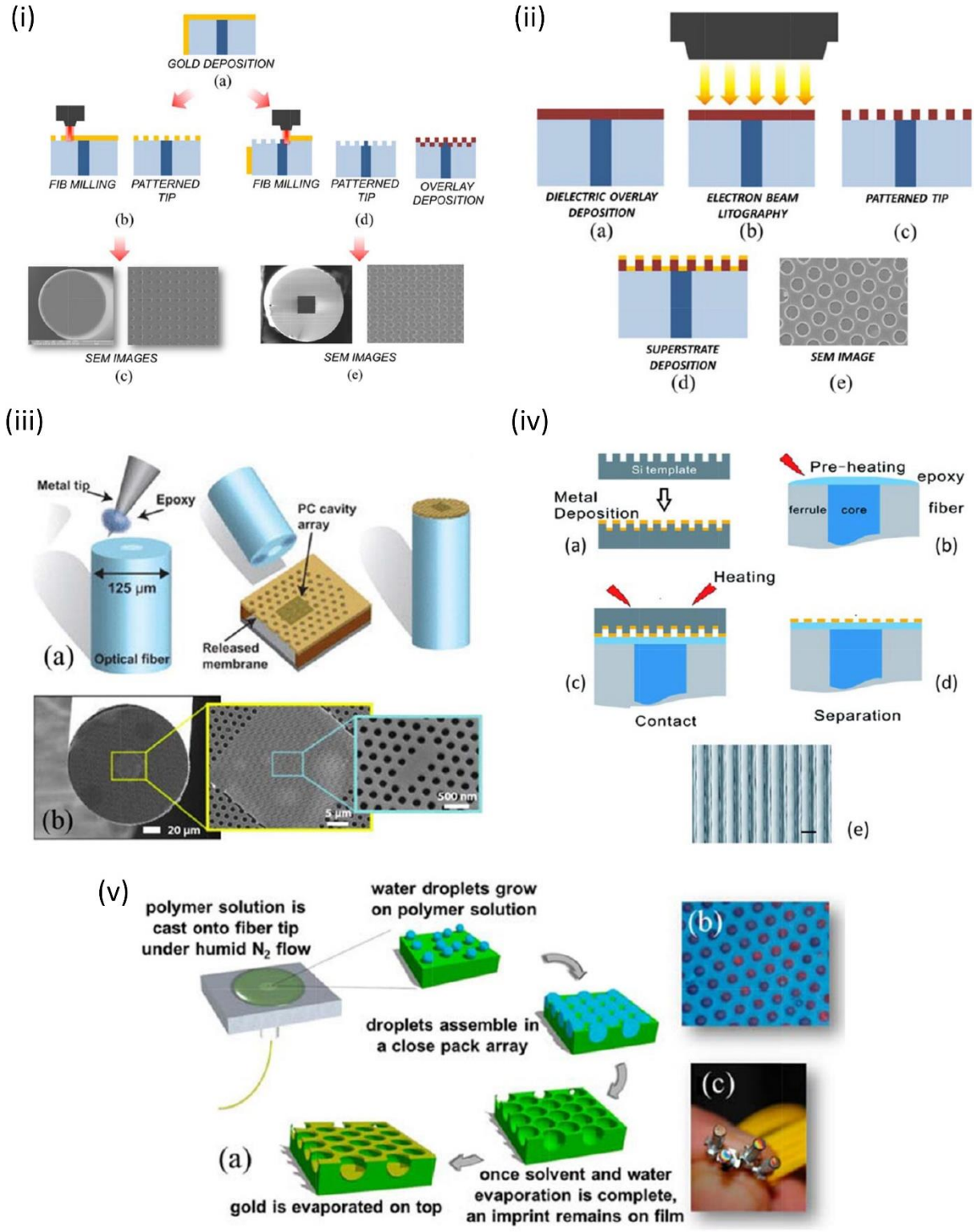


Fig. 1.6: *(i) Schematic of two FIB milling processes: (a) Au deposition; (b) milling the Au overlay (c) SEM images of a plasmonic nanostructure; (d) milling the optical fiber and overlay deposition (e) SEM images of a 'double' PC nanostructure [44]. (ii) Optical fiber tip during*

*the EBL process: (a) overlay deposition through spin coating, (b) nano-patterning of the deposited resist, (c) patterned nanostructure, (d) superstrate deposition of different functional materials and (e) SEM image of a realized device [50]. (iii) PCC optical fiber tip probe fabricated by Shambat et al. (a) A schematic representation of the epoxy transfer process [56]. (b) SEM images of the fiber PC probe [57]. (iv) Schematic of the fabrication procedure of a hybrid technique: (a) realization of a nanostructure on a Si template, (b) deposition and pre-heating of an epoxy adhesive, (c-d) contact and separation on the fiber tip to transfer the nanostructure. (e) SEM image of a realized device [58]. (v) (a) Schematic overview of the breath figure technique employed by Pisco et al.; (b) Confocal microscopy image of the patterned fiber; (c) fiber-optic prototypes [59].*

Focused ion beam (FIB) is a direct write approach in which a focused beam of ion is bombarded on the fiber tip that directly mills the fiber tip via the sputtering process as shown in Figure 1.6(i). However, FIB suffers from some drawbacks, such as unwanted ion doping into the final device, angled sidewalls of the nanopatterns and serial fabrications. So far, there are several reports in literature that use FIB for carving microcantilever sensor [45], optical tweezer [46], microchannels [47], plasmonic nanoapertures [48] and plasmonic arrays of circular and bow-tie shaped nanostructures [49] at the fiber tip. Electron beam lithography (EBL) is another powerful technique of writing patterns on fiber end facet. The fiber top is irradiated by an electron beam which modifies the chemical properties of an electron beam resist already coated on the fiber tip also illustrated in Figure 1.6(ii). EBL has been used widely to carve photonic and plasmonic crystals at the fiber tip [50-52]. However, spin coating resist at the fiber is very challenging owing to its extremely small surface area. Femtosecond laser micromachining has also been used to create micro-sized structures such as surface grating [53], Fresnel zone plate lenses [54] and SERS probes [55] at the fiber tip. The main drawback of this method is the rough surface of the patterned areas.

The second category of fiber tip patterning includes fabrication of nanostructures on a planar substrate via one of the methods described above and subsequent transferring of the nanostructures to fiber tip. The nano-transferring method does not suffer from critical handling

of the fiber as there is no direct writing step on the fiber end facet. Yet, the pattern transfer to fiber tip is a critical step which affects the fabrication yield and device performance [44]. An epoxy-based method for integrating photonic crystal cavities at the fiber tip is shown in Figure 1.6(iii) [56], [57]. The epoxy is first spread around the fiber top by means of a micromanipulator stage. The fiber tip is next pressed against the photonic crystal structure realized on a planar substrate using standard EBL. When the epoxy gets cured, the fiber tip is separated from the photonic crystal mold and the structure gets transferred to the fiber tip. Epoxy-based nanostructure transfer has also been used to realize a plasmonic sensor at the fiber tip [58] (Figure 1.6(iv)). Self assembly (SA) is an easier, faster and cheaper alternative to nanoimprint lithography. SA allows mass production of fiber tip-based sensors by creating ordered patterns on several optical fibers in parallel. Pisco et al. have used breath figure method to realize patterned optical fiber probes as shown in Figure 1.6(v) [59].

### 1.3.2 Sensing Around the Fiber

The external curved surface of the optical fiber provides large interaction length and easy access for micro and nanotechnologies. In order to make the fiber sensitive to the surrounding medium, light needs to be coupled from the core region toward the cladding. This can be done by creating a tapered region along the length of the fiber. The fiber is pulled while heated, thus the diameter along a particular region reduces down to submicron scale [60]. Light gets coupled from the core to the cladding in the tapered region. Another way of exposing the fiber core to the surrounding medium is to etch away the core which leads to the interaction of evanescent wave with outside medium [61]. Diffraction gratings can also be inscribed on the core of the fiber in contrast to fiber tapering or cladding removal [62], [63]. Two types of grating structures are written on the core, long period gratings (LPGs) and tilted fiber Bragg gratings (FBGs). The LPGs couple core modes of the fiber with co-propagating cladding

modes. As a result, several dips occur in the light transmitted out of the fiber according the phase matching conditions among the core and cladding modes. The wavelengths at which this phase matching occurs are highly sensitive to refractive index changes of the surrounding medium. Such configurations as shown in Figure 1.7 are widely used for sensing the changes of refractive index in the surrounding medium.

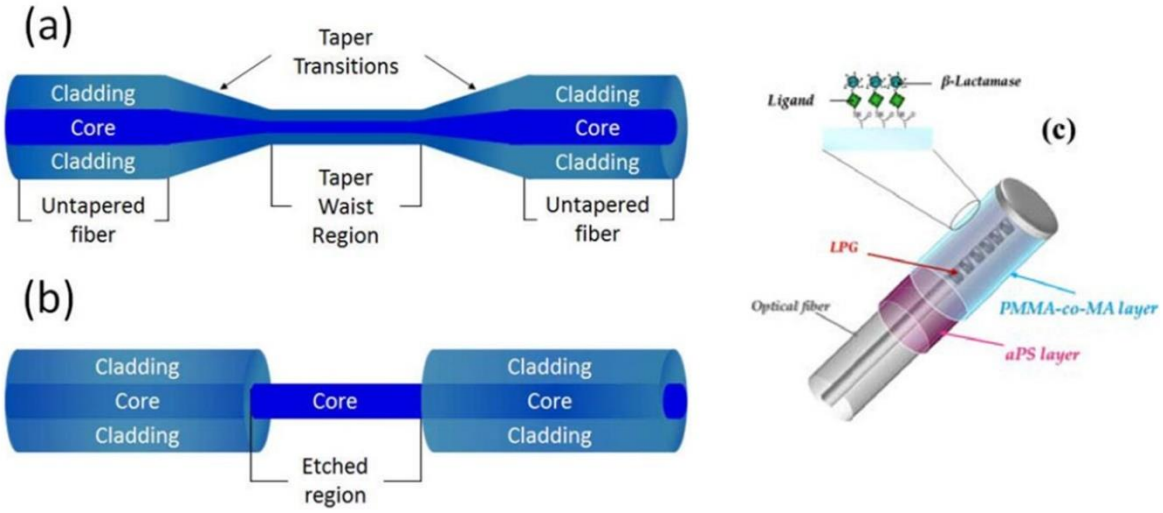


Fig. 1.7: *(a) Schematic representation of a typical tapered fiber optic manufactured with a "heat and pull" technique. (b) Etched fiber [44]. (c) Picture of a ligand coated log period grated fiber [64].*

### 1.3.3 Sensing Inside the Fiber

Air holes are introduced in the fiber running along the length of the fiber to realize "in fiber" devices. Such devices, known as photonic crystal fibers (PCFs) can be divided into two main classes. The first class, named as solid-core PCF, involves a solid core and a microstructured cladding and is based on modified total internal reflection due to the effective

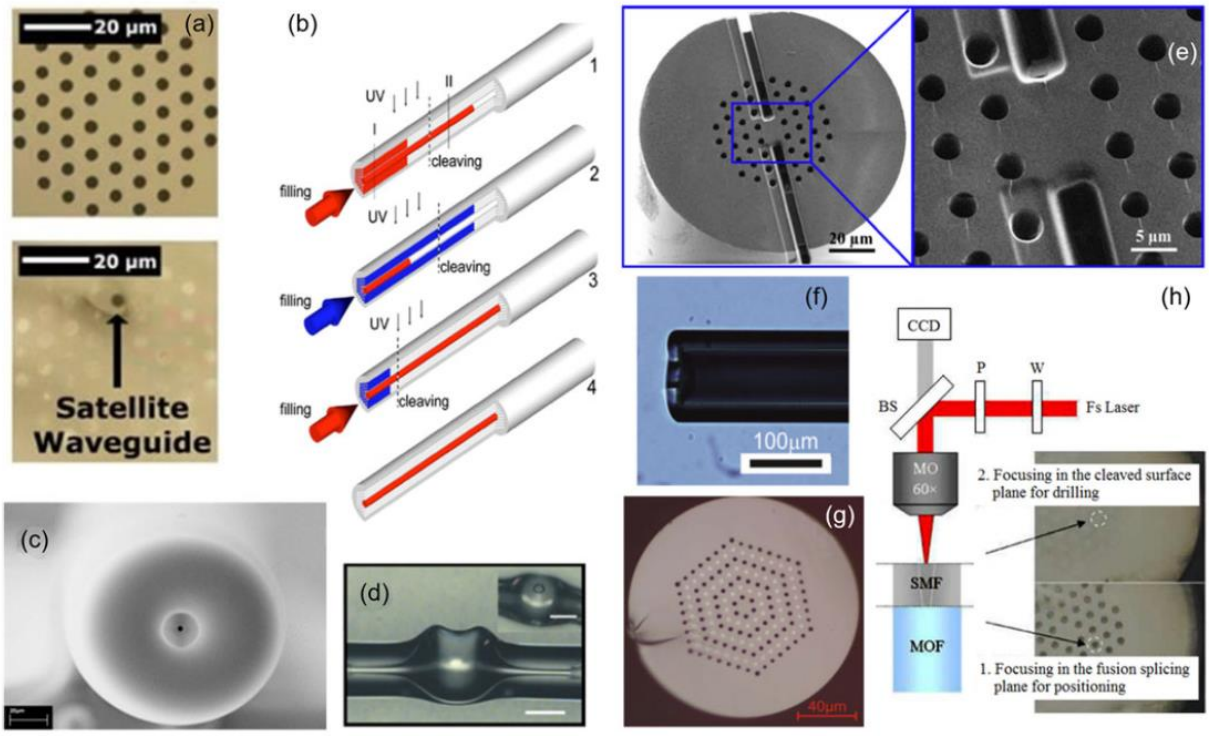


Fig. 1.8: *(a) Microscope image of a pristine PCF and of the corresponding glued PCF end facet [65]. (b) Schematics of the "injection-cure-cleave" technique of selective filling [66]. (c) Selective holes sealing by using a commercial fusion splicer [67]. d) Optical microscope images of the HOF with lateral access [68]. (e) Top view of the milled microchannels on the end facet of PCF. Zoom of the microchannel across the central air holes [69]. (f) Microscope image of a HC-PCF with cladding holes sealed via the $CO_2$ laser cleaving method [70]. (g) PCF selectively filled with toluene by the direct laser writing technique [71]. (h) Schematics of the selective filling technique based on the fs laser instrument. SEM in the insets show the cleaved fiber end images focused in the fusion splicing plane and the cleaved surface plane, respectively [72] and [44].*

RI difference between the core and cladding [44]. The second class is termed as hollow-core PCF which includes an air core and the light is confined by the photonic bandgap effect owing to the microstructured cladding. The holey structure allows realization of microfluidic photonic devices where strong light-matter interaction takes place along the entire length of the microstructured core/cladding region. Figure 1.8 shows different versatile, robust and integrated techniques of selectively filling PCF structures, such as by direct manual gluing [65], injection-cure-cleave [66], fusion splicing [67], [68], FIB milling to define microchannels

[69], $CO_2$ laser technique [70], two-photon direct laser technique [71], and femtosecond laser technique [72]. For sensing physical, chemical and biological characteristics of liquids and gases, PCF offers unparalleled sensitivity owing to the capability to directly insert the functional materials into the holes of the microstructured fiber along with the long-range interaction of analyte molecules with confined light [68].

### 1.4 Problem Statement and Novelty of This Thesis

Up to now, we have discussed different types of nanostructured surfaces realized on both large substrates and miniaturized optical fibers for liquid and gas sensing. The main areas of challenge here are lack of suitable absorption materials for selective detection of different gases and making a miniaturized yet highly sensitive sensor head that can be easily inserted into remote regions.

To overcome the above-mentioned challenges, we have first developed a plasmonic nanostructure integrated with graphene oxide and demonstrated it for gas sensing. For selective detection of gases, we have also fabricated an array of plasmonic sensors coated with different thicknesses of graphene oxide and used a pattern recognition algorithm to differentiate different gases in a gas mixture. Next, we developed a first-of-a-kind, novel guided mode resonance (GMR) -based nanostructures inscribed at the fiber tip that promotes continuous and label-free monitoring of gaseous and aqueous analytes. Instead of using the expensive direct writing approaches which are difficult to employ due to the microscopic cross-section and mechanical flexibility of the fiber tip, we have used nano-imprint lithography to inscribe nanophotonic patterns at the cleaved facet of the fiber. The GMR structure integrated with graphene oxide at the fiber tip has been demonstrated toward a first application in gas sensing. We have also presented a first-of-a-kind design to integrate a heater to the nano-patterned fiber-tip optical sensor so as to make it reusable gas sensor. The sensor has been demonstrated for

gas sensing, but by virtue of being designed on a fiber tip, it has other tremendous potential for in-vivo sensing. Since the nano-sensor is inscribed at the end facet of an optical fiber the diameter of which is only a couple of hundred micrometers, the sensing probe can be directly inserted into aqueous and gaseous analytes which are otherwise inaccessible (just like an endoscope probe it can be used for glucose monitoring as an example). Moreover, our work on using these optical nano-sensors to measure the dynamic response to gas absorption is quite novel and technical, showing the well-versed contribution in design/engineering as well as in theory/algorithmic aspects of research. Further, we developed a tunable, nano-resonant structure on chalcogenide glasses for selective detection of gases in infrared region of the EM spectrum.

### 1.5 Thesis Organizations

The following chapters represent an accumulation of three published journal papers and five conference papers.

Chapter 2 describes a high-sensitivity gas sensor based on plasmonic crystal incorporating a thin layer of graphene oxide (GO) that could detect as well as differentiate plant volatiles in ppm levels. The sensor works on the principle that gas adsorption of GO modifies the refractive index of the plasmonic structure and returns a shift in the resonance wavelength of the surface plasmon polariton excited at the GO coated plasmonic surface. To identify the gas species in a complex gas mixture, a sensor array is designed with different sensing elements coated with different thicknesses of GO. The optical responses of the different sensing elements to a gas mixture are analyzed using principal component analysis (PCA) based pattern recognition algorithm to differentiate different species of gases, providing specificity of the device. The paper, entitled “Plasmonic crystal-based gas sensor toward an optical nose design” has been published in *IEEE Sens. J.*, 17, 6210-6223 (2017).

Chapter 3 reports on a new fiber-tip GMR structure integrated with GO, toward a first application in gas sensing. This fiber tip patterning technology allows producing fiber-optic sensors for remote in-field measurements in biomedical, environmental, agricultural, and other applications The paper entitled “Nanopatterned optical fiber tip for guided mode resonance and application to gas sensing” has been published in *IEEE Sens. J.*,**17**, 7262-7272 (2017).

Chapter 4 describes the first heater integrated nanostructured optical fiber to realize a high-sensitivity and reusable fiber-optic gas sensor. The paper, entitled “Heater integrated nanopatterned optical fiber-tip to realize a reusable gas sensor”, has been published in the Proceedings of Photonic Fiber and Crystal Devices: Advances in Materials and Innovations in Device Applications XII, San Diego, CA, USA (2018).

Chapter 5 reports on an effective yet simple approach to study the dynamic variations in optical properties (such as the refractive index (RI)) of graphene oxide (GO) when exposed to gases in the visible spectral region, using the thin-film interference method. The paper, entitled “Determination of dynamic variations in the optical properties of graphene oxide in response to gas exposure based on thin-film interference” has been published in the Optics Express, 26(5), 6331-6344 (2018).

Chapter 6 reports on the first of a kind planar mid-IR resonant structure that undergoes enhanced light absorption by the analyte adsorbed on its surface, enabling highly sensitive and selective label-free detection of gas and/or biomarkers. This is a noteworthy research endeavor because 2D chalcogenide patterns have not been used for infrared gas sensing by any known public research available. The paper, entitled “Tunable mid-infrared optical resonator on nanopatterned chalcogenide glasses” has been published in the Proceedings of Infrared Sensors, Devices, and Applications VIII, San Diego, CA, USA (2018).

## 1.6 References

[1] J. W. Kemling, A. J. Qavi, R. C. Bailey, and K. S. Suslick, "Nanostructured surface for optical sensing", J. Phys. Chem. Lett., vol. 17, pp. 2934-2944, 2011.

[2] T. Srivastava, R. Jha, and R. Das, "High performance bimetallic SPR sensor based on periodic-multilayer-waveguides", IEEE Photon. Technol. Lett., vol. 23, pp. 1448-1450, 2011.

[3] K. Gazzaz, and P. Berini, "Theoretical biosensing performance of surface plasmon polariton Bragg gratings", Appl. Opt., vol. 54, pp. 1673-1680, 2015.

[4] E. Wijaya, C. Lenaerts, S. Maricot, J. Hastanin, S. Habraken, J. P. Vilcot, R. Boukherroub, and S. Szunerits, "Surface plasmon resonance-based biosensors: from the development of different SPR structures to novel surface functionalization strategies", Curr. Opin. Solid State Mater. Sci., vol. 15, pp. 208-224, 2011.

[5] J. Katyal, and R. K. Soni, "Localized surface plasmon resonance and refractive index sensitivity of metal-dielectric-metal multilayered nanostructures", Plasmonics, pp. 1171-1181, 2005.

[6] P. Englebienne, "Use of colloidal gold surface plasmon resonance peak shift to infer affinity constants from the interactions between protein antigens and antibodies specific for single or multiple epitopes", Analyst, vol. 123, pp. 1599-1603, 1998.

[7] M. D. Malinsky, K. L. Kelly, G.C. Schatz, and R. P. Van Duyne, "Chain length dependence and sensing capabilities of the localized surface plasmon resonance of silver nanoparticles chemically modified with alkanethiol self-assembled monolayers", J. Am. Chem. Soc., vol. 123, pp. 1471-1482, 2001.

[8] A. J. Haes, and R. P. Van Duyne, "A nanoscale optical biosensor: sensitivity and selectivity of an approach based on the localized surface plasmon resonance spectroscopy of triangular silver nanoparticles", J. Am. Chem. Soc., vol. 124, pp. 10596-10604, 2002.

[9] M. E. Stewart, C. R. Anderton, L. B. Thompson, J. Maria, S. K. Gray, J. A. Rogers, and R. G. Nuzzo, "Nanostructured plasmonic sensors", Chem. Rev., vol. 108, pp. 494-521, 2008.

[10] S. W. Lee, K. S. Lee, J. Ahn, J. J. Lee, M. G. Kim, and Y. B. Shin, "Highly sensitive biosensing using arrays of plasmonic Au nanodisks realized by nanoimprint lithography", ACS Nano, vol. 5, pp. 897-904, 2011.

[11] M. E. Stewart, J. Yao, J. Maria, S. K. Gray, J. A. Rogers, and R. G. Nuzzo, "Multispectral thin film biosensing and quantitative imaging using 3D plasmonic crystals", Anal. Chem., vol. 81, pp. 5980-5989, 2009.

[12] G. A. Mines, B. C. Tzeng, K. J. Stevenson, J. L. Li, and J. T. Hupp, “Microporous supramolecular coordination compounds as chemosensory photonic lattices”, Angew. Chem. Int. Edit., vol. 41, pp. 154-157, 2002.

[13] R. C. Bailey, and J. T. Hupp, “Large-scale resonance amplification of optical sensing of volatile compounds with chemoresponsive visible-region diffraction gratings”, J. Am., Chem. Soc., vol. 124, pp. 6767-6774, 2002.

[14] E. F. Melo, and E. Fontana, “Optimization of metal gratings for SPR sensing applications”, SBMO/IEEE MTT-S Int. Microwave Optoelectron. Conf., 2011.

[15] P. K. Sahoo, S. Sarkar, and J. Joseph, “High sensitivity guided-mode resonance optical sensor employing phase detection”, Sci. Rep., vol. 7, pp. 7607, 2017.

[16] L. Guo, Q. Wang, Y. Huang, and D. Zhang, “Portable organic gas detection sensor based on the effect of guided-mode resonance”, AIP Advances, vol. 7, pp. 015031, 2017.

[17] M. J. Uddin, and R. Magnusson, “Highly efficient color filter array using resonant Si3N4 gratings”, Optics express, vol. 21, pp. 12495–12506, 2013.

[18] M. J. Uddin, T. Khaleque, and R. Magnusson, “Guided-mode resonant polarization-controlled tunable color filters”, Optics Express, vol. 22, pp. 12307-12315, 2014.

[19] M. J. Uddin, and R. Magnusson, “Efficient guided-mode-resonant tunable color filters”, IEEE Photon. Technol. Lett., vol. 24, pp. 1552-1554, 2012.

[20] R. Magnusson, and S. S. Wang, “New principle for optical filters”, Appl. Phys. Lett., vol. 61, pp. 1022-1024, 1992.

[21] X. Wei, and S. M. Weiss, “Guided mode biosensor based on grating coupled porous silicon waveguide”, Optics Express, vol. 19, pp. 11330-11339, 2011.

[22] R. W. Sabnis, “Color filter technology for liquid crystal displays”, Displays, vol. 20, pp. 119-129, 1999.

[23] Q. Chen, X. Hu, L. Wen, Y. Yu, and D. R. Cumming, “Nanophotonic image sensors”, Small, vol. 1, 2016.

[24] R. Haider et al., “Free-standing subwavelength metallic gratings for snapshot multispectral imaging”, Appl. Phys. Lett., vol. 96, pp. 2211041-3, 2010.

[25] D. Wawro, S. Tibuleac, R. Magnusson, and H. Liu, “Optical fiber endface biosensor based on resonances in dielectric waveguide gratings”, Biomedical Diagnostics, Guidance, and Surgical-Assist Systems II Proc. SPIE, vol. 3911, pp. 86-94, 2000.

[26] B. Cunningham et al., "A plastic colorimetric resonant optical biosensor for multiparallel detection of label-free biochemical interactions", Sens. Actuators B, vol. 85, pp. 219-226, 2002.

[27] X. Wei, and S. M. Weiss, "Guided mode biosensor based on grating coupled porous silicon waveguide", Optics Express, vol. 19, pp. 11330-11339, 2011.

[28] C. Pacholski, M. Sartor, M. J. Sailor, F. Cunin, and G. M. Miskelly, "Biosensing using porous silicon double-layer interferometers: reflective interferometric fourier transform spectroscopy", J. Am. Chem. Soc., vol. 127, pp. 11636-11645, 2005.

[29] S. O. Meade, M. Y. Chen, M. J. Sailor, and G. M. Miskelly, "Multiplexed DNA detection using spectrally encoded porous $SiO_2$ photonic crystal particles", Anal. Chem., vol. 81, pp. 2618-2625, 2009.

[30] M. Gomilsek, and M. Ravnik, "Whispering gallery modes", 2011 at http://mafija.fmf.uni-lj.si/seminar/files/2011_2012/wgm.pdf

[31] B. E. Little, J. -P. Laine, and H. A. Haus, "Analytic theory of coupling from tapered fibers and half-blocks into microsphere resonators", J. Lightwave Technol., vol. 17, pp. 704-715, 1999.

[32] J. -P. Laine, "Design and Applications of Optical Microsphere Resonators", 2003 at http://lib.tkk.fi/Diss/2003/isbn951226448X/isbn951226448X.pdf

[33] A. Matsko, V. Iltchenko, and D. Streka, "Delaying Trains of Short Light Pulses in WGM Resonators", 2008 at https://ntrs.nasa.gov/archive/nasa/casi.ntrs.nasa.gov/20080048146.pdf.

[34] M. Iqbal, M. A. Gleeson, B. Spaugh, F. Tybor, W. G. Gunn, M. Hochberg, T. Baehr-Jones, R. C. Bailey, and L. C. Gunn, "Label-free biosensors arrays based on silicon ring resonators and high-speed optical scanning instrumentation", IEEE J. Sel. Top. Quantum Electron., vol. 16, pp. 654-661, 2010.

[35] D. X. Xu et al. "Label-free biosensor array based on silicon-on-insulator ring resonators addressed using a WDM approach", Opt. Lett., vol. 35, pp. 2771-2773, 2010.

[36] A. L. Washburn, M. S. Luchansky, A. L. Bowman, and R. C. Bailey, "Quantitative, label-free detection of five protein biomarkers using multiplexed arrays of silicon photonic microring resonators", Anal. Chem., vol. 82, pp. 69-72, 2010.

[37] A. J. Qavi, and R. C. Bailey, "Multiplexed detection and label-free quantification of microRNAs using arrays of silicon photonic microring resonators", Angew. Chem. Int. Edit., vol. 49, pp. 4608-4611, 2010.

[38] A. M. Armani, R. P. Kulkarni, S. E. Fraser, R. C. Flagan, and K. J. Vahala, "Label-free, single-molecule detection with optical microcavities", Science, vol. 317, pp. 783-787, 2007.

[39] H. K. Hunt, C. Soteropulos, and A. M. Armani, "Bioconjugation strategies for microtoroidal optical resonators", Sensor-basel, vol. 10, pp. 9317-9336, 2010.

[40] D. O'Shea, C. Junge, S. Nickel, M. Poellinger, and A. Rauschenbeutel, "Ultra-high Q whispering-gallery-mode bottle microresonators: properties and applications", 2011 at http://adsabs.harvard.edu/abs/2011arXiv1105.0351O

[41] K. Srinivasan, M. Borselli, O. Painter, A. Stintz, and S. Krishna, "Cavity Q, mode volume, and lasing threshold in small diameter AlGaAs microdisks with embedded quantum dots" Opt. Express, vol. 14, pp. 1094-1105, 2006.

[42] L. Tobing, and P. Dumon, "Fundamental Principles of Operation and Notes on Fabrication of Photonic Microresonators", Photonic Microresonator Research and Applications, vol. 156, pp. 1-27, 2010.

[43] T.J.A. Kippenberg, "Nonlinear optics in ultra-high-Q whispering-gallery optical microcavities", 2004, at https://thesis.library.caltech.edu/2487/

[44] P. Vaiano et al., "Lab on fiber technology for biological sensing applications", Laser Photonics Rev., vol. 10, pp. 922-961, 2016.

[45] D. Iannuzzi, S. Deladi, J. W. Berenschot, S. De Man, K. Heeck, and M. C. Elwenspoek, "Fiber-top atomic force microscope", Rev. Sci. Instrumen., vol. 77, pp. 106105, 2006.

[46] C. Liberale, P. Minzioni, F. Bragheri, F. De Angelis, E. Di Fabrizio, and I. Cristiani, "Miniaturized all-fiber probe for three-dimensional optical trapping and manipulation", Nat. Photonics, vol. 1, pp. 723-727, 2007.

[47] S. Kang, H. E. Joe, J. Kim, Y. Jeong, B. K. Min, and K. Oh, "Subwavelength plasmonic lens patterned on a composite optical fiber facet for quasi-one-dimensioanl Bessel beam generation", Appl. Phys. Lett., vol. 98, pp. 241103, 2011.

[48] A. Dhawan, M. D. Gerhold, and J. F. Muth, "Plasmonic structures based on subwavelength apertures for chemical and biological sensing applications", IEEE Sens. J., vol. 8, pp. 942-950, 2008.

[49] G. Andrade et al., "Surface-enhanced resonance Raman scattering using Au nanohole arrays on optical fiber tips", Plasmonics, vol. 8, pp. 1113-1121, 2013.

[50] M. Consales et al., "Lab-on-fiber technology: toward multifunctional optical nanoprobes", ACS Nano, vol. 6, pp. 3163-3170, 2012.

[51] Y. Lin, Y. Zou, and R. G. Lindquist, “A reflection-based localized surface plasmon resonance fiber-optic probe for biochemical sensing”, Opt. Express, vol. 2, pp. 478-484, 2011.

[52] M. Sanders, Y. Lin, J. Wei, T. Bono, and R. G. Lindquist, “An enhanced LSPR fiber-optic nanoprobe for ultrasensitive detection of protein biomarkers”, Biosens. Bioelectron., vol. 61, pp. 95-101, 2014.

[53] W. Shin et al., IEEE Photonics Technol. Lett., vol. 19, pp. 550-552, 2007.

[54] J. K. Kim, J. Kim, K. Oh, I. -B. Sohn, W. Shin, H. Y. Choi, and B. Lee, IEEE Photonics Technol. Lett., vol. 21, pp. 21, 2009.

[55] X. Lan, Y. Han, T. Wei, Y. Zhang, L. Jiang, H. L. Tsai, and H. Xiao, “Surface-enhanced Raman-scattering fiber probe fabricated by femtosecond laser”, Opt. Lett., vol. 34, pp. 2285-2287, 2009.

[56] G. Shambat, J. Provine, K. Rivoire, T. Sarmiento, J. Harris, and J. Vuckovic, “Optical fiber tips functionalized with semiconductor photonic crystal cavities”, Appl. Phys. Lett., vol. 99, pp. 191102, 2011.

[57] G. Shambat et al., “A photonic crystal cavity-optical fiber tip nanoparticle sensor for biomedical applications”, Appl. Phys. Lett., vol. 100, pp. 213702, 2012.

[58] P. Jia and J. Yang, “A plasmonic optical fiber patterned by template transfer as a high-performance flexible nanoprobe for real-time biosensing”, Nanoscale, vol. 6, pp. 8836-8843, 2014.

[59] M. Pisco, F. Galeotti, G. Quero, A. Iadicicco, M. Giordano, and A. Cusano, “Miniaturized sensing probes based on metallic dielectric crystals self-assembled on optical fiber tips”, ACS Photonics, vol. 1, pp. 917-927, 2014.

[60] Y. Tian, W. H. Wang, N. Wu, X. T. Zou, and X. W. Wang, “Tapered optical fiber sensor for label-free detection of biomolecules”, Sensors, vol. 11, pp. 3780-3790, 2011.

[61] V. P. Kude, and R. S. Khairnar, “Fabrication and nimerical evaluation of the tapered single mode optical fiber: detection of change in refractive index”, Indian J. Pure Appl. Phys., vol. 46, pp. 23-29, 2008.

[62] F. Baldini, M. Brenci, F. Chiavaioli, A. Giannetti, and C. Trono, “Optical fibre gratings as tools for chemical and biological sensing”, Anal. Bioanal. Chem., vol. 402, pp. 109-116, 2012.

[63] M. Consales, M. Pisco, and A. Cusano, “Lab-on-fiber technology: a new avenue for optical nanosensors”, Photonic Sensors, vol. 2, pp. 289-314, 2012.

[64] G. Quero et al., “Long period fiber grating working in reflection mode as valuable biosensing platform for the detection of drug resistant bacteria”, Sens. Actuators B Chem., vol. 230, pp. 510-520, 2016.

[65] D. K. C. Wu, B. T Kuhlmey, and B. J. Eggleton, “Ultrasensitive photonic crystal fiber refractiv eindex sensor”, Opt. Lett., vol. 34, pp. 322-324, 2009.

[66] Y. Huang, Y. Xu, and A. Yariv, “Fabrication of functional microstructured optical fibers through a selective-filling technique”, Appl. Phys. Lett., vol. 85, pp. 5182-5184, 2004.

[67] L. Xiao, W. Jin, M. Demokan, H. Ho, Y. Hoo, and C. Zhao, “Fabrication of selective injection microstructured optical fibers with a conventional fusion splicer”, Opt. Express, vol. 13, pp. 9014-9022, 2005.

[68] C. M. B. Cordeiro, E. M. dos Santos, C. H. B. Cruz, C. J. de Matos, and D. S. Ferreira, “Lateral access to the holes of photonic crystal fibers-selective filling and sensing applications”, Opt. Express, vol. 14, pp. 8403-8412, 2006.

[69] F. Wang, W. Yuan, O. Hansen, and O. Bang, “Selective filling of photonic crystal fibers using focussed ion beam milled microchannels”, Opt. Express, vol. 19, pp. 17585-17590, 2011.

[70] L. Xiao, N. V. Wheeler, N. Healy, and A. C. Peacock, “Integrated hollow-core fibers for nonlinear optofluidic applications”, Opt. Express, vol. 21, pp. 28751-28757, 2013.

[71] M. Vieweg, T. Gissibl, S. Pricking, B. T. Kuhlmey, D. C. Wu, B. J. Eggleton, and H. Giessen, “Ultrafast nonlinear optofluidics in selectively liquid-filled photonic crystal fibers”, Opt. Express, vol. 18, pp. 25232-25240, 2010.

[72] Y. Wang, C. R. Liao, and D. N. Wang, “Femtosecond laser-assisted selective infiltration of microstructured optical fibers”, Opt. Express, vol. 18, pp. 18056-18060, 2010.

# CHAPTER 2. PLASMONIC CRYSTAL BASED GAS SENSOR TOWARD AN OPTICAL NOSE DESIGN

A paper published in IEEE Sensors Journal

Shawana Tabassum, Ratnesh Kumar, and Liang Dong

## 2.1 Abstract

This paper reports a high-sensitivity gas sensor based on plasmonic crystal incorporating a thin layer of graphene oxide (GO). The plasmonic crystal consists of a periodic array of polymeric nanoposts with gold (Au) disks at the top and nanoholes in an Au thin film at the bottom. The thin GO layer coated atop the plasmonic crystal is the gas absorbent material for the sensor. Gas adsorption of GO modifies the refractive index of the plasmonic structure and returns a shift in the resonance wavelength of the surface plasmon polariton (SPP) excited at the GO coated Au surface. The differences in target gas species and their adsorption in GO lead to a difference in the resonance shift. To identify the gas species in a complex gas mixture, a sensor array is designed with different sensing elements coated with different thicknesses of GO. The optical responses of the different sensing elements to a gas mixture are analyzed using principal component analysis (PCA) based pattern recognition algorithm. The PCA separates the sensor responses to different species of gases, providing specificity of the device. The proposed sensor demonstrates a refractive index sensitivity of 449.63 nm/RIU. In addition, volatile organic compounds (VOCs) such as ethylene, methanol that serve as plant health indicators and ammonia that plays a key role in the ecosystem, are detected by the sensor. A change in a gas concentration results in a differing amount of adsorbate and correlated shift in the resonance wavelength of the device. The GO coated sensor exhibits sensitivities of 0.6 pm/ppm to gaseous ethylene, 3.2 pm/ppm to methanol, and 12.84 pm/ppm to ammonia. The

integration of plasmonic sensing element arrays with varying GO thicknesses to modulate the gas adsorption, offers a promising approach to detect different gas species in a single test.

## 2.2 Introduction

We present an "optical nose" for sensing gases, especially the ones useful as plant health indicators such as ethylene, methanol, and ammonia. Plant growth and development are profoundly influenced by several chemical substances including ethylene and methanol. Ethylene regulates cell size and cell division, initiates the fruit ripening process and accelerates senescence of leaves [1], [2]. Methanol, on the other hand, is responsible for early stages of plant leaf development [3]. Plants emit ethylene and/or methanol during different stages of development as well as when plants respond to environmental stimuli from biotic and/or abiotic stresses [4]. Measuring the presence and concentration of these gases released by plants is of utmost importance to carefully monitor the condition of fruits and vegetables, and significantly prevent their wastage due to over-ripening. Furthermore, gaseous ammonia ($NH_3$) emission from plant's foliage and shoots bears a measurable impact on the biotic as well as abiotic components of our ecosystem. Exchange of ammonia between the atmosphere and plants plays a significant role in flora decline due to for example excessive nitrogen deposition. Thus, detecting concentrations of $NH_3$ can help monitor environmental health. The importance of ethylene and methanol in plant development and of ammonia in healthy ecosystem makes it imperative to develop highly sensitive and selective gas sensors for their monitoring.

An ethylene gas sensor utilizing carbon nanotube [1] and an indium tin oxide (ITO) thin film based methanol gas sensor [5] have been reported. These sensors work on the basis of the conductance/resistance variation upon the adsorption of gas species on their surface. A number of surface plasmon resonance (SPR) based optical sensors have been reported for the detection of ammonia [6]–[8]. Numerous optical gas sensors have also been reported by

integrating optical resonators and gas absorption materials, or using optical resonators alone. Polymers such as silicone rubber, polyvinylchloride (PVC), and polytetrafluoroethylene with immobilized gas sensitive chemical reagents were used in optical sensors to detect various gases [9]. Localized surface plasmon resonance (LSPR) at the surface of gold (Au) and silver nanoparticles, and gold nanoshells allowed the detection of gas-molecular-bindinginduced changes of refractive index [10]. Au nanoparticles were also coupled with reduced graphene oxide (rGO) to generate LSPR for gas sensing [11]. Fiber-optic sensors that eliminate bulky optics and offer easy insertion of device into the sensing area have also been reported: An SPR based chlorine gas sensor was realized by applying indium oxide doped tin oxide to the surface of silver-coated optical fiber core [12]. In addition, an SPR based fiber-optic ammonia gas sensor was designed using a tin-oxide ($SnO_2$) layer over the silver-coated unclad core of the fiber [6]. Other works studied nanocomposite films of poly (methyl methacrylate) (PMMA), rGO and PMMA/rGO [7], polyaniline coated ITO thin film [8], graphene-carbon nanotubes-poly(methyl methacrylate) hybrid nanocomposite [13], and ITO thin film and nanoparticles [14] to develop SPR based fiber-optic gas sensors. Also, various photonic crystal (PC)-based resonators were developed for the detection of volatile organic compounds (VOCs) [15], under the principle of index modulation upon vapor adsorption and condensation inside the PCs. The extremely high quality factor of whispering gallery mode (WGM) was also utilized to generate resonance shift caused by specific binding of gas molecules through enhanced photon-gas molecule interactions [16]. Furthermore, chalcogenide glass waveguides have been used for gas detection due to their very high refractive index (2.0-4.0) and transparency in the mid-infrared spectral regime [17].

Notably, resonant characteristics of surface plasmon polariton (SPP)-based

nanostructures are sensitive to subtle changes in surrounding refractive index, and thus, are finding sensor applications for the detection of chemical and biological species [18]. These nanostructures are mostly limited to liquid-phase detection of biomolecules such as protein [19], DNA [20], cancer biomarkers [21] and glucose [22]. However, due to the lack of suitable absorption materials for detecting gas molecules, it remains challenging to generate a large output signal in response to minute concentration of gas. Recently, GO has led to the development of many ultrasensitive sensors owing to high surface-area-to- volume ratio [23] and sufficient functional groups (e.g., carboxyl, hydroxyl, carbonyl and epoxide) at the surface of GO nanosheets providing effective trap centers for various gas species [24]. Several electronic gas sensors have used GO and GO-based nanocomposites for gas detection [25], [26], where their electrical conductivities change upon exposure to gases. To date, there are limited reports on integrating GO as a sensing material with SPP-based nanostructures for the detection of gas molecules [27]. In addition, the utilization of principal component analysis (PCA) to separate the gas species and improve specificity is an integral feature in our sensing approach.

In this paper, we report an optical gas sensor utilizing enhanced gas adsorption ability of GO and the strong light matter interaction at the surface of lithographic plasmonic nanoposts. The plasmonic nanostructures are composed of an array of nanoposts with Au disks at the top and perforated nanoholes in an Au thin film at the bottom. The nanostructures are coated with a thin layer of GO nanosheets to form a sensitive adsorption surface for gas molecules, and support the excitation of SPPs at the dielectric/Au interface with a high refractive index sensitivity. More importantly, to distinguish different types of gaseous species, an array of nanostructured sensors is designed, where the surface of each individual sensor is

coated with a different thickness of GO. Depending on the GO coating thickness, the amount of gas molecules absorbed by GO varies, leading to a different modulation for the effective refractive index of GO at different sensing elements when responding to a specific gas species. This allows for the selective identification of gas species by integrating a pattern recognition algorithm such as PCA algorithm [28]. This work resulted in the publications [27] and [29].

## 2.3 Sensor Design and Working Principle

The GO coated plasmonic crystal sensor is shown in Fig. 2.1a. The nanoposts made of a ZPUA (ZIPCONE™ UA) polymer have a square lattice with the period of 500 nm, the diameter of 250 nm, and the height of 210 nm. The surface of the sensor is coated by 5 nm thick titanium and 50 nm thick Au. The device was formed using soft lithography based replica nanomolding process. The details of fabrication processes appear in Supplementary Materials. To enhance the specificity of this sensor to different gas species, an array of three sensors was formed on the same substrate, by coating with three different thicknesses of GO: 16.3 nm, 32.6 nm, and 48.9 nm. This sensor array was used to examine the response of the sensors to gaseous ethylene, methanol and ammonia.

### 2.3.1 Working Principle

When gas molecules are adsorbed at the surface of GO nanosheets, the hydroxyl and carboxyl groups at the basal planes and edges of GO form oxo- or hydroxo-bridges with the gas molecules. This results in free electron transfers between the GO nanosheets and gas molecules. The change in conductivity of GO in response to its interaction with gas molecules can be written as [30],

$$\Delta\sigma_{GO}(t) = \Delta\sigma_{max,GO}\ \frac{cK}{1+cK}\left[1-\exp\left(-\frac{1+cK}{K}\ kt\right)\right] \qquad (2.1)$$

where $\Delta\sigma_{GO}$ is the change in conductivity of GO, $\Delta\sigma_{max,GO}$ is the maximum change in conductivity with sufficient gas exposure, $K$ is binding equilibrium constant, $k$ is surface reaction rate constant, $c$ is the concentration of gas and $t$ is the time for gas exposure. The refractive index of GO, $\eta_{GO}$ is calculated from the following equation [31], [32],

$$\eta_{GO} = \left(\frac{1}{2\omega\varepsilon_0 t_{GO}}\right)^{1/2}\left(-\sigma_{GO,i} + \sqrt{4{\sigma_{GO,r}}^2 + {\sigma_{GO,i}}^2}\right)^{1/2} \quad (2.2)$$

where, $\omega$ is the angular frequency, $\varepsilon_0$ = 8.85x10$^{-12}$ F/m and $t_{GO}$ is thickness of the GO nanosheet. It can be observed from (2.1) and (2.2) that $\eta_{GO}$ is related to gas concentration $c$, and higher the value of $c$, higher the value of $\eta_{GO}$. These equations explain how $\eta_{GO}$ varies when the GO nanosheet is exposed to gases of varying concentrations. The variation in $\eta_{GO}$ causes shifts in the resonance wavelengths of surface plasmons, as explained below, and that shift is what we measure experimentally.

Under normal incidence, the free space light to excite a SPP at the dielectric/metal interface for a square lattice is given by the following equation [33]:

$$\lambda_{SPP} = \frac{\Lambda}{\sqrt{i^2+j^2}}\sqrt{\frac{\varepsilon_d\varepsilon_m}{\varepsilon_d+\varepsilon_m}}\ , \quad (2.3)$$

where $\varepsilon_d$ and $\varepsilon_m$ are the dielectric constants of the dielectric and the metal (Au in our work), respectively, $\Lambda$ is the lattice period, and $(i, j)$ is the order of SPP. For the proposed structure, $\Lambda$ = 500 nm and when the Au nanostructures are coated with a thin layer of GO nanosheets, $\varepsilon_d = (\eta_{GO})^2$. Hence, in presence of adsorbed gases with concentration $c$, $\eta_{GO}$ varies according to the Equations (2.1) and (2.2), causing $\varepsilon_d$ to vary, which in turn causes $\lambda_{SPP}$ to shift. The relative permittivity of Au, $\varepsilon_m \equiv \varepsilon_m(\lambda)$ depends on wavelength and is taken from the experimental data [34]. Equation (2.3) can be used to determine the resonance $\lambda_{SPP}$ under the influence of index modulation of the surrounding medium. The equation cannot be solved directly because

relative permittivity of Au is a function of wavelength, and so the wavelength appears on both sides of the equation. In order to compute the SPP resonance wavelength, left and right hand sides of (2.3) are plotted as a function of wavelength. From the intersection of the two curves, the calculated SPP resonance $\lambda_{SPP}$ for $(i, j) = (1, 0)$ at the air/Au interface is 546.7 nm.

## 2.4 Experimental Results and Analysis

### 2.4.1 Characterization of Au/GO Coated Nanopatterns

A schematic of the GO coated sensor is given in Fig. 2.1a. The scanning electron microscopy (SEM) analysis was performed to provide a comprehensive characterization of the GO coated plasmonic nanostructure (Fig. 2.1b-d). The top-view SEM image of the bare nanopatterns (without Au or GO coating) is shown in Fig. 2.1b. After coating the device with a 50 nm thick Au layer followed by a coating of 0.2 mg/ml GO dispersion solution, a $70^0$ tilt-view SEM image of the device was taken (Fig. 2.1c). The boundary between GO coated and uncoated device is clearly visible in Fig. 2.1c. It is also confirmed from the SEM image that the GO nanosheet is conforming to the structure beneath it. In order to reveal the thickness of the GO nanosheets, a $70^0$ tilt-view SEM image was captured at the edge of the device where GO nanosheets got detached from the device surface (Fig. 2.1d).

### 2.4.2 Bulk Refractive Index Change Characterization

A bifurcated optical fiber (BIF 400-VIS-NIR, Ocean Optics) was used to illuminate the sensor from a white light source (150 watt quartz halogen lamp, Luxtec Fiber Optics) through a collimator (F220SMA-A, Thorlabs), and collect the reflected light from the sensor into a spectrometer (USB-4000, Ocean Optics). We measured the reflectance spectra with normal incident light. When the bare (without GO coating) plasmonic nanostructure was exposed to air, a reflectance dip appeared at 547.1 nm (Fig. 2.2a, D1). Next, we performed the bulk refractive index sensitivity measurement of the Au-coated nanoposts without GO coating (Fig.

2.2a). Water (η = 1.33), acetone (η = 1.363), ethanol (η = 1.365), isopropyl alcohol (IPA) (η = 1.377), and chloroform (η = 1.44) were dropped on the top of the device and covered with a glass coverslip (Fig. 2.2a). As the surrounding medium changed from air to water, acetone, ethanol, IPA or chloroform, the resonance wavelength shifted from 547.1 nm (D1) to 688 nm (D2), 700.8 nm (D3), 702.5 nm (D4), 710.5 nm (D5) or 741.5 nm (D6) respectively (Fig. 2.2a). Thus, the sensor exhibited a refractive index sensitivity of 449.63 nm/RIU, shown in Fig. 2.2a inset.

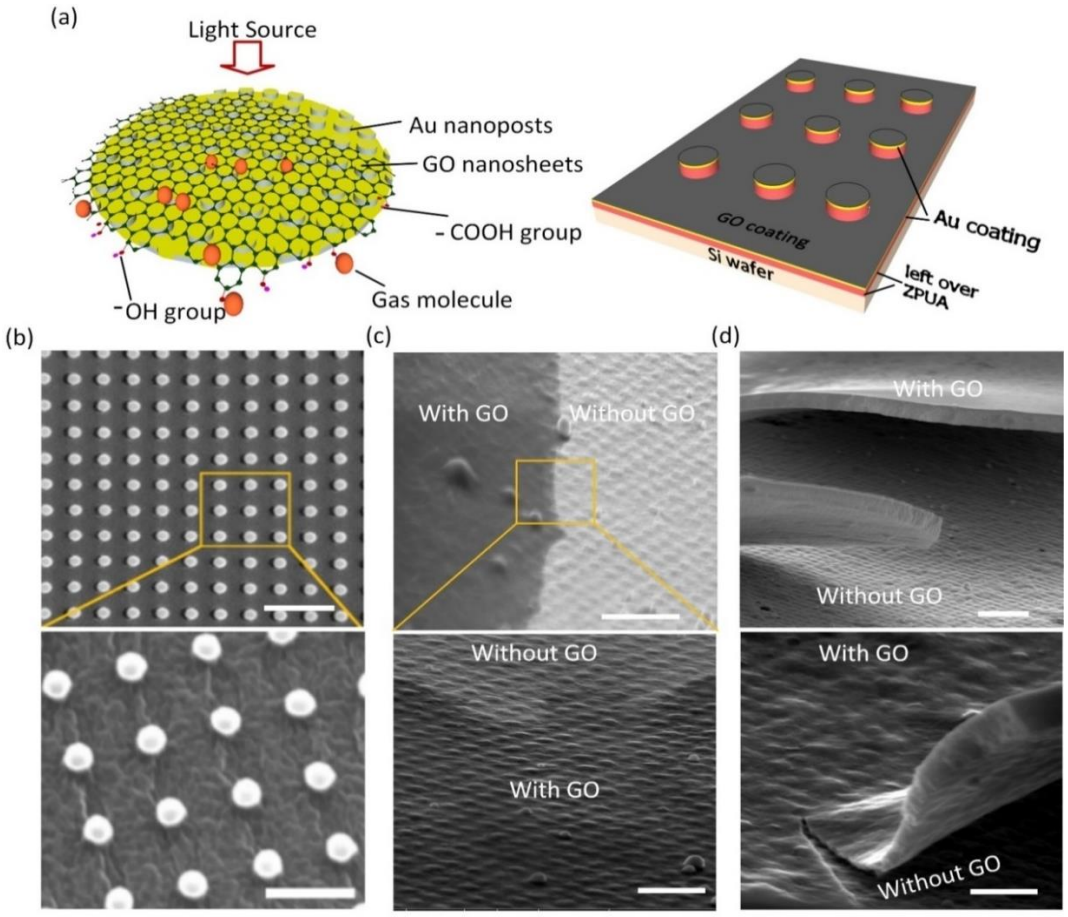


Fig. 2.1: *(a) Schematic illustration of the GO coated plasmonic crystal sensor. (b) Top-view scanning electron microscopy (SEM) images of an array of polymer nanoposts (lattice constant = 500 nm, post diameter = 250 nm, post height = 210 nm) without Au coating. Scale bars represent 1 µm (top panel) and 500 nm (bottom panel). (c) $70^0$ tilt-view of the nanopost array deposited with Au/GO coating. Scale bars represent 2 µm (top panel) and 1 µm (bottom panel). (d) $70^0$ tilt-view of the GO nanosheet separated from the nanopost surface at the edge. Scale bars represent 2 µm (top panel) and 1 µm (bottom panel).*

### 2.4.3 Optical Simulations

Finite element analysis method was used to carry out full wave numerical simulations with the commercial COMSOL software. Fig. 2.2b shows the experimental and simulated reflection spectra of the plasmonic nanostructure with and without the GO coating. A certain thickness (300 nm) of left-over ZPUA polymer beneath the nanoposts (Fig. 2.1a) was also incorporated in order to simulate the actual device. The resonance dip at $\lambda_{Vs1}$ = 547.1 nm for the bare structure (without GO) corresponds to the excitation of (1,0) SPP at the air/Au interface. This is confirmed by the standing wave feature above the Au nanodisk and below the Au film as can be seen in the simulated electric field distribution (Fig. 2.2c). Moreover, it can be observed that the resonant field penetrates approximately 100 nm to the surrounding dielectric (e.g. air), which helps determine the thickness of GO coating to be used for gas adsorption and its interaction with the electric field distribution. Accordingly, the maximum thickness of the GO coating that we used was 48.9 nm, well below the observed field penetration depth into air of 100 nm. The strong interaction between the LSPRs at the Au nanodisk and Au film results in a Fabry-P*é*rot (FP) resonance at $\lambda_{Vs2}$ = 725 nm (Fig. 2.2c). Such FP resonance has also been observed in [35] – [37]. The dip at $\lambda_{Vs3}$ = 905 nm is due to a relatively weaker coupling between the LSPRs mentioned above (Fig. 2.2c). The three reflectance dips in the simulated spectrum ($\lambda_{Vs1,}$ $\lambda_{Vs2,}$ and $\lambda_{Vs3}$) correspond to the three dips ($\lambda_{Ve1,}$ $\lambda_{Ve2,}$ and $\lambda_{Ve3}$) in the experimental reflectance spectrum (Fig. 2.2b). However, the simulated reflectance dip $\lambda_{Vs2}$ is slightly blue shifted with respect to the experimentally observed dip $\lambda_{Ve2}$. This may be attributed to the unknown thickness of left-over ZPUA in real device below the nanoposts. Because of the enhanced penetration of (1, 0) SPP resonant field into the surrounding dielectric compared to the LSPR fields, the shift in (1, 0) SPP resonance wavelength was measured in response to changes in surrounding refractive indices. After

coating the device with a 16.3 nm thick GO layer, the (1, 0) SPP resonance wavelength of the device shifted from $\lambda_{Vs1}$ = 547.1 nm (bare structure without any GO coating) to $\lambda_{Vs4}$ = 550.1 nm (with GO coating) as shown in Fig. 2.2b. The figure also confirms that the measured and simulated results agree well with each other.

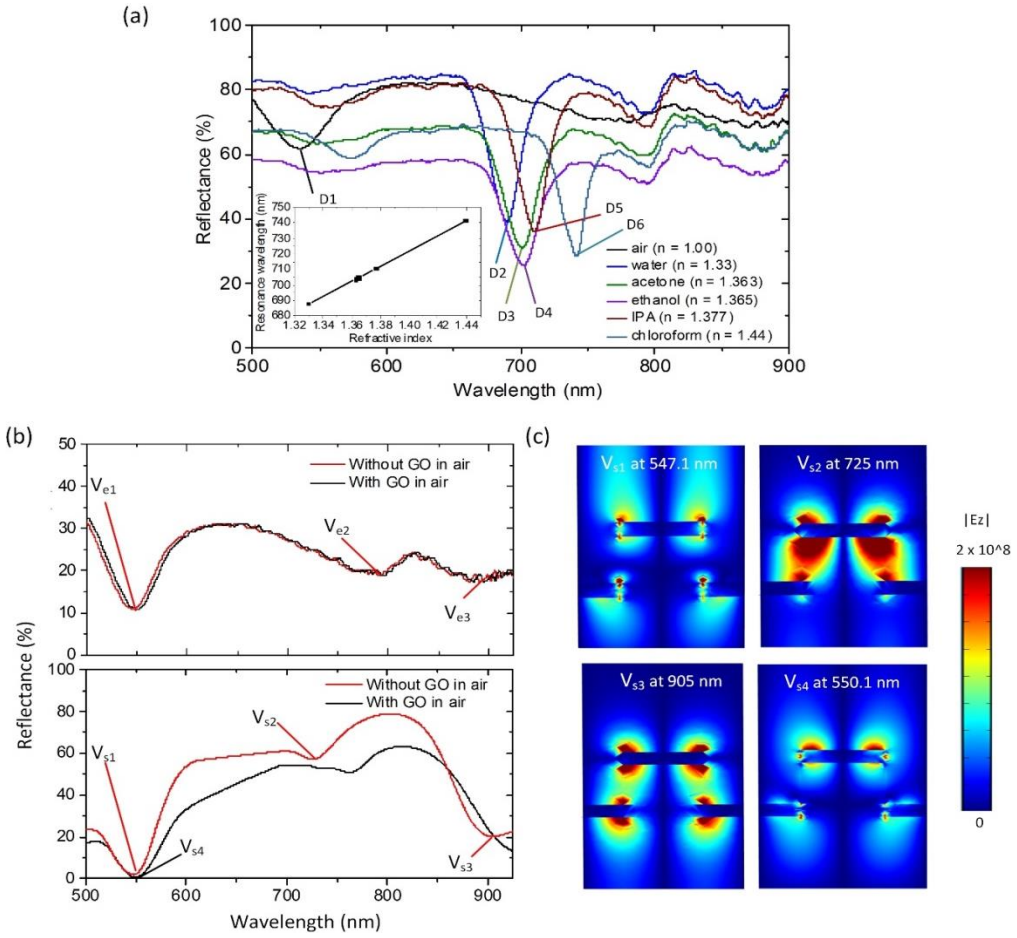


Fig. 2.2: *Reflectance spectra of bare structure (without GO) in response to air ($\lambda_{D1}$ = 547.1 nm), water ($\lambda_{D2}$ = 688 nm), acetone ($\lambda_{D3}$ = 700.8 nm), ethanol ($\lambda_{D4}$ = 702.5 nm), IPA ($\lambda_{D5}$ = 710.5 nm) and chloroform ($\lambda_{D6}$ = 741.5 nm). The inset shows refractive index sensitivity curve. (b) The measured (upper panel) and simulated (lower panel) reflection spectra of the plasmonic nanostructure without and with a 16.3 nm thick GO coating under normal incidence of light. $V_{s1}$, $V_{s2}$, $V_{s3}$ and $V_{s4}$ in the simulated spectra indicate the reflection features of interest. $\lambda_{Vs1}$ = 547.1 nm, $\lambda_{Vs2}$ = 725 nm, $\lambda_{Vs3}$ = 905 nm and $\lambda_{Vs4}$ = 550.1 nm. (c) Simulated cross-sectional electric field distribution at the SPP resonant wavelength of 547.1 nm, 725 nm and 905 nm without any GO coating, and at the SPP resonance wavelength of 550.1 nm with a 16.3 nm thick GO coating. The color bar shows field intensity.*

## 2.5 Application to Gas Sensing

The GO coated plasmonic nanostructure was demonstrated to function as a gas sensor. To achieve selectivity, a combination of GO layer thickness variations together with a PCA based pattern recognition was employed. Varying the thickness provided varying reflection spectra responses that contained the signature of the gas species, whose extraction was achieved via the PCA. An array of three sensors was designed to have different response characteristics to gases owing to different thicknesses of the GO coating, namely, 16.3 nm, 32.6 nm, and 48.9 nm.

### 2.5.1 Chemical Interaction of Gases with GO

The hydroxyl, carboxyl and the epoxy groups present at the basal planes and edges of GO play a significant role in capturing gas molecules. The binding mechanism of $NH_3$, methanol and ethylene gases at GO nanosheets is illustrated in Fig. 2.3. $NH_3$ interacts with carboxyl groups as either Bronsted (Fig. 2.3a) or Lewis (Fig. 2.3b) acids [38]. $NH_3$ also reacts with the epoxy groups via nucleophilic substitution (Fig. 2.3c) and forms amide [38]. In a moist environment, water molecules form hydrogen bonds with the hydroxyl and epoxy groups present between GO layers leading to less amount of $NH_3$ adsorption. In dry condition (in the absence of $H_2O$ molecules), $NH_3$ binding with the hydroxyl and epoxy groups is significantly enhanced. Methanol also works as a nucleophile that attacks the carboxyl groups at GO and forms ester (Fig. 2.3d) [39]. When the GO nanosheets are exposed to ethylene, it attacks the hydroxyl groups at GO via nucleophilic substitution (Fig. 2.3e) [40].

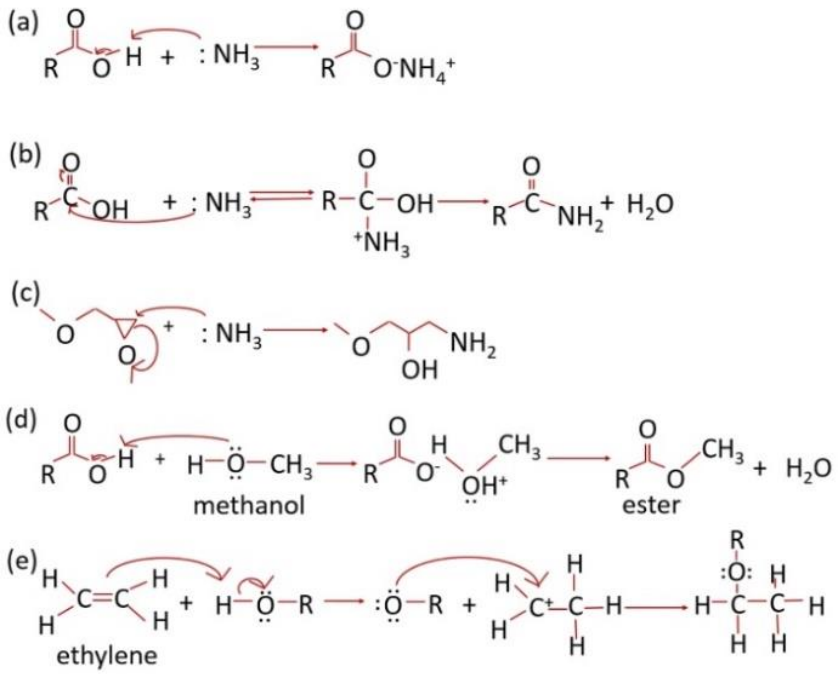


Fig. 2.3: *Mechanism of interaction of $NH_3$ (a,b,c), methanol (d), and ethylene (e) gases with the functional groups present at GO nanosheets.*

### 2.5.2 Experimental Setup

The experimental setup for gas sensing using the GO coated plasmonic sensor is shown in Fig. 2.4. The gas species (pre-diluted with nitrogen) flowed from cylinders into an aluminum gas chamber which contained the sensor. The sensor was illuminated from a white light source through a bifurcated fiber and the reflected light was collected by a spectrometer. Inside the chamber, the testing gas was further diluted by the carrier nitrogen gas. The gas flow rate was controlled by a mass flow controller (MFC) (GFC17, Aalborg). Ethylene with concentrations of 500 ppm, 666.66 ppm and 750 ppm, methanol with concentrations of 250 ppm, 333.33 ppm and 375 ppm and $NH_3$ with concentrations of 100 ppm, 117 ppm and 120 ppm were tested. A constant flow rate of dry nitrogen (10 ml/min) was maintained inside the closed chamber and flow rate of ethylene, methanol and/or $NH_3$ was varied to modify the concentration of the test gases at regular intervals using the MFCs. The main purpose of using dry nitrogen is to drive

away moisture from the chamber, so that moisture does not produce any false spectral shifts of the sensor.

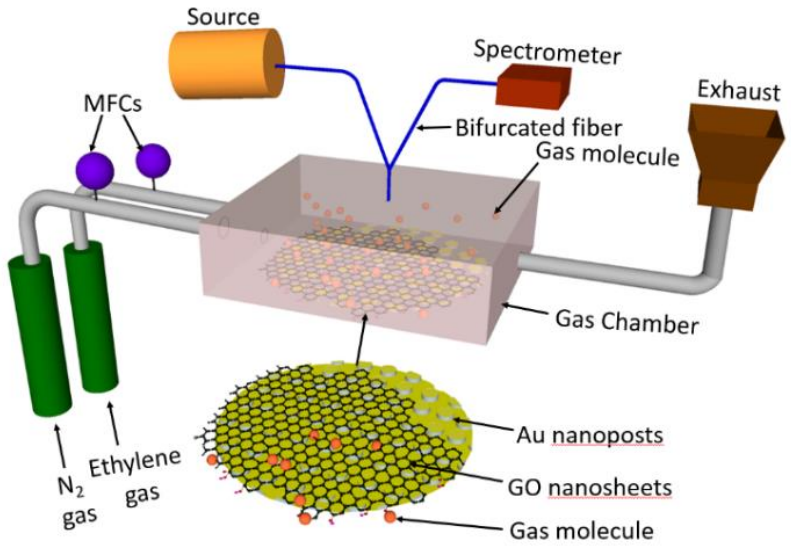


Fig. 2.4: *Schematic illustration of experimental setup for gas sensing using GO coated plasmonic nanostructure.*

### 2.5.3 Gas Sensing Results

Figure 2.5 shows the reflection spectra of the three sensors array before and after being exposed to ethylene, methanol and $NH_3$ at different concentrations. With a change in local dielectric environment, a shift in resonant wavelength was observed. The thicker the GO coating, the higher the dielectric permittivity in the vicinity of the metal surface, and hence the higher the resonance wavelength shift. With 16.3 nm, 32.6 nm, and 48.9 nm GO coatings, resonance wavelength red-shifted from 547.1 nm to 550.1 nm, 554.2 nm and 555.25 nm respectively (Fig. 2.5a). When only nitrogen was introduced into the chamber, the resonance wavelength red-shifted to 550.7 nm, 555.66 nm, and 556.1 nm for 16.3 nm, 32.6 nm, and 48.9 nm GO coatings respectively (Fig. 2.5a). When the sensor response was saturated in presence of nitrogen, ethylene was flown into the chamber. In the presence of ethylene gas, a red shift of the SPR wavelength occurred for all the three sensing elements. For example, with 48.9 nm

GO coating, resonance wavelength shifts of 0.42 nm, 0.1 nm, and 0.17 nm were observed when the sensor was exposed to 500 ppm, 666.66 ppm, and 750 ppm of gaseous ethylene respectively. Similarly, results were obtained for methanol and $NH_3$ gases (Fig. 2.5b-c).

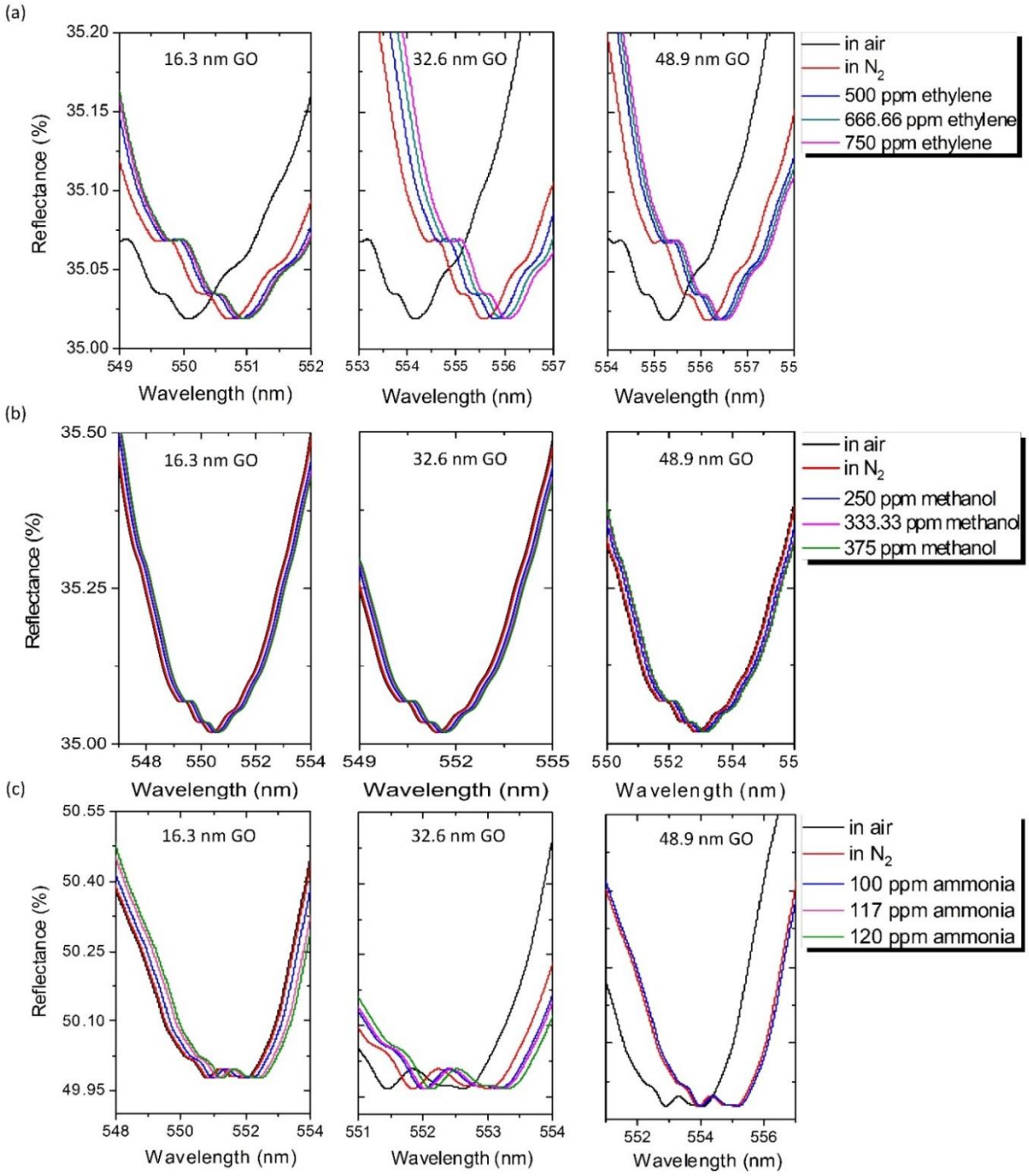


Fig. 2.5: *Reflectance spectra of plasmonic crystal gas sensors with three different thicknesses of GO when exposed to gaseous (a) ethylene, (b) methanol and (c) $NH_3$.*

### 2.5.4 Sensitivity Studies

Sensitivity of the sensor is defined as the shift in resonance wavelength per unit change in the gas concentration. Fig. 2.6 shows resonance wavelength shifts with a change in gas concentration for three different thicknesses of GO coating. The sensitivities of the sensor to gaseous ethylene, methanol and $NH_3$ with 16.3 nm GO coating (Fig. 2.6) were found to be approximately 0.6 pm/ppm, 3.2 pm/ppm and 12.84 pm/ppm respectively.

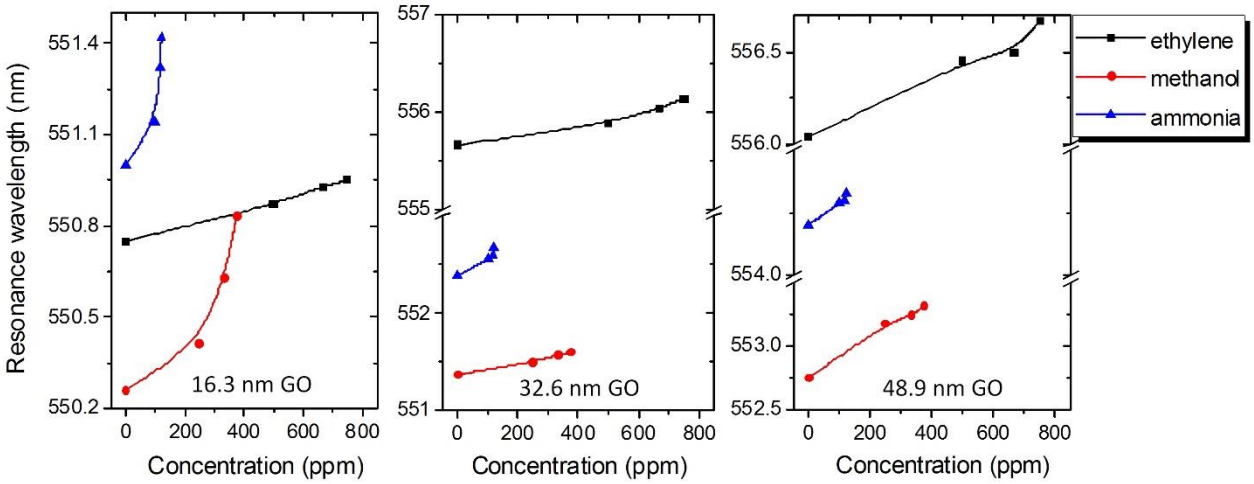


Fig. 2.6: *Resonance wavelength shifts of three plasmonic crystal gas sensors with different thicknesses of GO as a function of concentration of gaseous ethylene, methanol and $NH_3$.*

A fiber-tip based FP sensor reported in literature exhibits a sensitivity of 3.53 pm/ppm to methanol vapor [41] which is close to ours. In another work, an optical fiber long-period-grating gas sensor exhibited a sensitivity of 0.2 pm/ppm for methanol gas [42] which is almost 16 fold less compared to our sensor. Also several SPR based fiber-optic ammonia gas sensors have been reported using $Ag/SnO_2$ thin films with a sensitivity of 2.15 nm/ppm [6], using PMMA/rGO nanocomposite with sensitivity of 1 nm/ppm [7], using Indium tin oxide (ITO) and bromocresol purple with sensitivity of 1.891 nm/ppm [43]. The sensitivities of these sensors are higher than ours, but our plasmonic sensor offers other advantages. Firstly, it is superior in terms of fabrication methods: It employs inexpensive and simple nanomolding

process to fabricate the nanopattern-based SPR structure. Moreover, in order to selectively identify gas species, by simply varying the thicknesses of the GO coatings on the sensing elements in a sensor array, it is possible to differentiate a gas from the others in a gaseous mixture, by applying pattern recognition algorithms. There is no need of changing the structures of the nanoposts that otherwise will require costly nanoscale master molds, or varying compositions of gas absorbing materials. In contrast, in the aforementioned fiber-optic SPR based sensors [6], [7], [43], different composition of coating materials needs to be employed in order to selectively detect different gas species, requiring additional fabrication steps. Finally, to our knowledge, no ethylene detection sensor has been reported based on the principle of optical resonance wavelength shift.

### 2.5.5 Control and Reversibility Studies

We further studied the dynamic response of the sensor coated with 32.6 nm of GO nanosheets (Fig. 2.7a-c). During the entire experiment, dry nitrogen was kept flowing at a constant rate into the enclosed chamber. First, when nitrogen was introduced into the chamber, the sensor response became saturated at a resonance shift of 0.2 nm (Fig. 2.7a). After that, the sensor was exposed to varying concentrations of ethylene gas. We observed resonance shifts of 0.15 nm and 0.23 nm for 500 ppm and 666 ppm of ethylene gas respectively (Fig. 2.7a). With 750 ppm and 800 ppm of gaseous ethylene, resonance shifts of 0.05 nm and 0.05 nm were observed, respectively (Fig. 2.7a). As the gas concentration increased to 750 ppm, less amount of resonance shift was exhibited as compared to the shift observed for 500 ppm and 666 ppm of ethylene, perhaps because the gas molecules already remaining in the GO layer inhibited further interaction and hence adsorption of newer gas molecules. Hence, at higher concentration of ethylene gas no resonance shift will be observed which implies that the sensor has a fixed operation range. With 32.6 nm GO coating, the total shifts in resonance in response

to gaseous ethylene, methanol and ammonia were found to be 0.45 nm, 0.45 nm and 0.3 nm respectively (Fig. 2.7a-c). For comparison, we also performed the control dynamic measurements of the *bare* substrate (*without* any GO coating) (Fig. 2.7d-f). It is apparent from Fig. 2.7d that the bare sensor exhibits a much smaller total resonance shift of 0.01 nm in response to ethylene (which is 45 times smaller compared to that with GO coating). Figures 2.7e-f also show smaller resonance shifts in response to methanol (which is 10 times smaller compared to that with GO coating) and ammonia gases (which is 5 times smaller compared to that with GO coating). These measurements demonstrate a much higher sensitivity when coated with the GO nanosheets, thereby justifying our use of GO coating as a gas adsorption layer. The response time of the GO coated sensor, when exposed to certain concentrations (500 ppm, 666 ppm, 750 ppm, and 800 ppm) of ethylene, was approximately 40 s. The response time is mainly determined by the adsorption of gas molecules at the low or high-energy binding sites of GO nanosheets. The low energy $sp^2$ carbon domains lead to faster adsorption of molecules, while the vacancies, defects, and oxygen-containing functionalities act as high-energy binding sites with slower adsorption rate [26]. Also, the diffusion of the gas molecules to reach the active portion of the plasmonic nanostructure adds to the delay [44]. Weak dispersive forces allow the adsorption of gas molecules on $sp^2$-bonded carbon atoms of the GO layer. However, single and double hydrogen bonds are formed when gas molecules are captured at defect sites such as carboxylic acid group, requiring binding energies of several hundred meV/molecule [26]. When the gas flow (ethylene, methanol or $NH_3$) was turned off and the chamber was purged with dry $N_2$ gas, a partial recovery of the sensor was observed. This is likely because only the gas molecules bound to the low- energy binding sites of GO nanosheets are released during the purging with dry $N_2$, while the gas

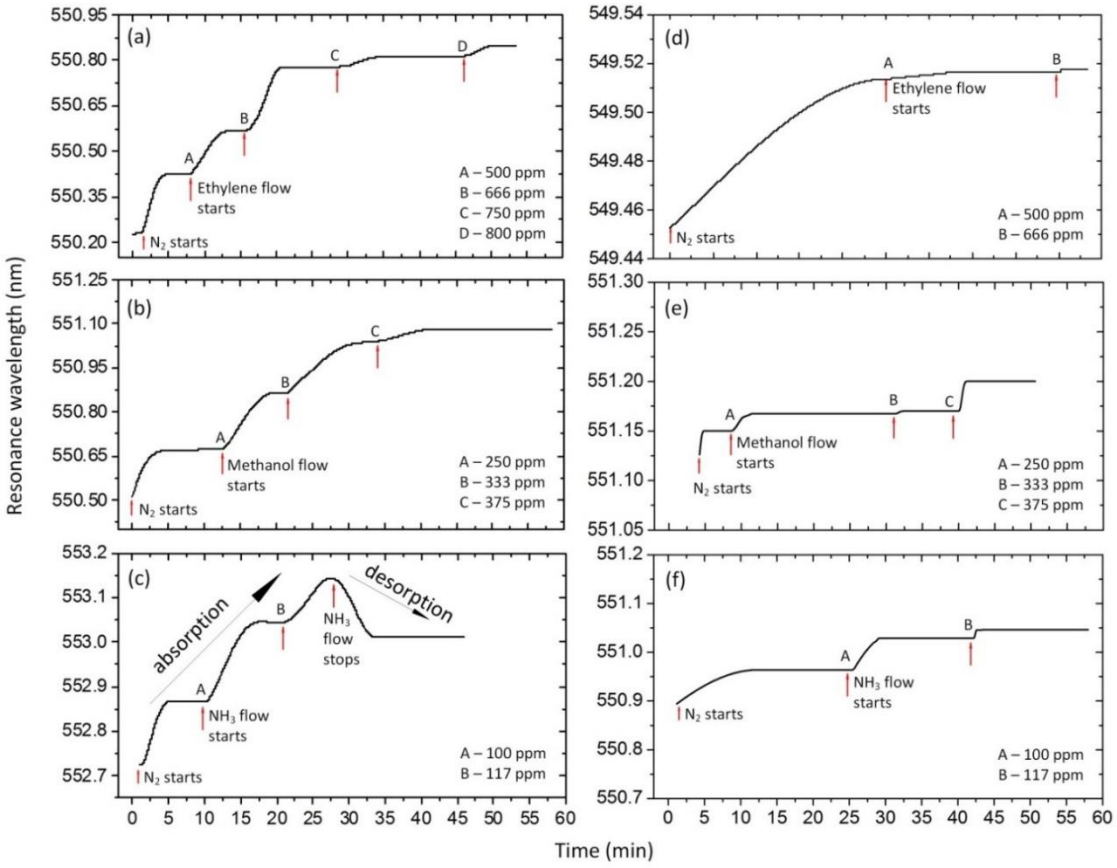


Fig. 2.7: *Monitoring the real-time adsorption of (a) ethylene, (b) methanol and (c) ammonia into the plasmonic nanostructure with 32.6 nm thick GO coating. Control dynamic experiments in response to (d) ethylene, (e) methanol and (f) ammonia without any GO coating. A, B, C and D represent the instants at which gas was introduced into the enclosed chamber.*

molecules captured by the high-energy binding sites remain adsorbed at the GO nanosheets. This is also confirmed by noting that the resonance wavelength did not return to the baseline upon turning off the gas flow as shown in Fig. 2.7c. This is not unexpected, and indeed a similar behavior was observed for GO covered optical nano-antenna structure exposed to gaseous analytes in [44]. A complete release of the bounded gases from the sensor surface requires a moderate heating. In our case, to prepare for a new cycle of the dynamic response, the device was thermally treated on a hot plate at $70^0$ C for 4 hours, allowing for a complete desorption of the gas molecules from the GO layer

### 2.5.6 Optimization of GO Thickness

We performed gas sensing experiments for different concentrations of GO dispersion solution in order to find an optimum GO solution providing maximum shift in resonance wavelength. It can be observed from Fig. 2.8 that with an increase in the concentration of GO dispersion solution, the resonance wavelength increases until a certain value of GO solution concentration, and then decreases. Experiments were conducted for gaseous ethylene in the concentration range of 500 ppm to 750 ppm and gaseous methanol in the concentration range of 250 ppm to 375 ppm. The maximum value of total shift in resonance wavelength was found to be 0.9 nm for ethylene with 0.75 mg/ml GO dispersion solution and 0.56 nm for methanol with 0.15 mg/ml GO dispersion solution.

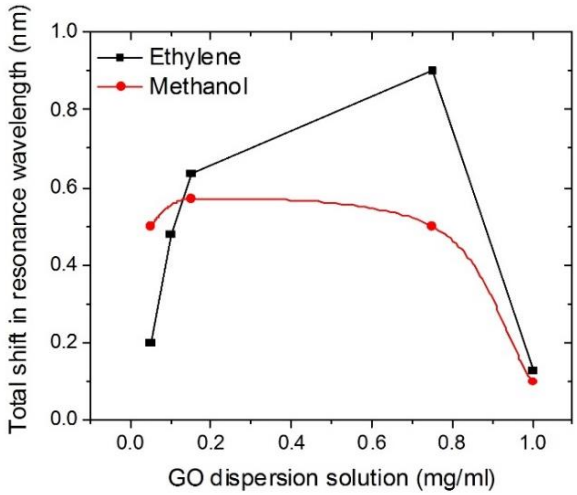


Fig. 2.8: *Variation of total shift in resonance wavelength with the concentration of GO dispersion solution for ethylene gas concentration ranging from 500 ppm to 750 ppm and methanol gas concentration ranging from 250 ppm to 375 ppm.*

### 2.5.7 Specific Gas Identification Using PCA Based Separation

The plasmonic nanostructure has been demonstrated to be sensitive to different gases such as ethylene, methanol and $NH_3$, but selectivity between different gases remains to be addressed owing to the interaction of GO nanosheets with all the gases which results in

corresponding resonance wavelength shifts as shown in Fig. 2.5. A multivariate analysis named PCA was used to extract selective response out of the SPR spectra of three identical sensors coated with three different thicknesses of GO. The responses of all the three sensors were collected, and a PCA method was applied to transform the data, allowing the separation of different gases, as the data corresponding a specific gas appeared in a single cluster upon the PCA based transformation. In our case, the PCA takes a multidimensional dataset and reduces it into a two-dimensional dataset, without crucial loss of information. For our experiments, the data matrix contained the response of each sensor with a different GO thickness to a certain gas and concentration. Utilizing the PCA, the data matrix was reduced to two principal components PC1, PC2, as plotted in Fig. 2.9. This figure demonstrates a clear separation of the three gas species in the three clusters, indicating the individual gases without overlap. Therefore, the PCA algorithm allows the identification of analytes with a set of three sensors with three different thicknesses of GO coated on the sensor surface. Certainly, other thickness levels can be introduced to be able to separate a larger number of species of gases. Thus, in our setting there is no need to change the compositions of the gas-absorbing films, only different GO thicknesses were needed, obtained via varying the concentrations of GO dispersion solutions using simple dip coating method.

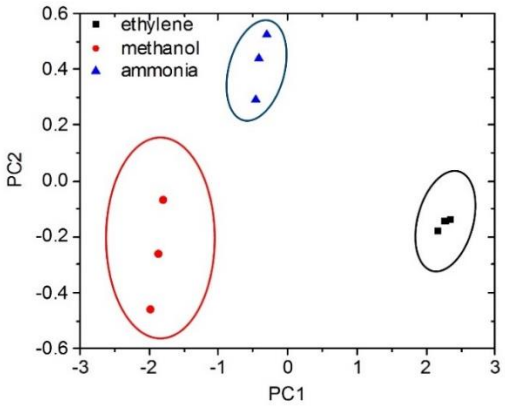


Fig. 2.9: *Pattern analyses based on PCA using three different sensors.*

## 2.6 Comparison to Related Optical Sensors

We presented a periodic nanopatterns based plasmonic gas sensor exhibiting spectral resonance shift in response to a change in surrounding refractive index in presence of gases, as well as a sensor array with varying thicknesses of GO layers to enable selective identification of gas species, aided by the PCA method. The sensor leverages the striking properties of GO nanosheets and plasmonic nanoposts to transduce gas molecule binding events into optical responses. Previously, sensors have been reported that work based on the principle of LSPR [10]. Generally, LSPR sensors display less sensitivity to changes in the bulk refractive index compared to the propagating SPR sensors [45]. The performance of the LSPR sensors also depends greatly on the nanoparticle composition, size, shape and orientation. A variety of chemical syntheses and lithographic techniques have also been adopted to manipulate these parameters with relatively complex and expensive fabrication methods. On the other hand, most of the existing SPR based sensors with GO layers are dedicated to biomolecules detection in liquids [19], [21]. Our sensor employs the SPR principle to probe gaseous species using a nanopost-based plasmonic structure obtained by an inexpensive nanomolding process. Our device allows for easy excitation of surface plasmons without using complex optics as in [46]. Moreover, by simply varying the thicknesses of GO layer on identical sensing elements in a sensor array, it is possible to differentiate a gas from the others in a gas mixture, using a PCA algorithm. There is no need of varying the structures of nanoposts as such that otherwise will require costly nanoscale master molds. Similarly, there is also no need of varying compositions of gas absorbing materials that are commonly used in electronic nose devices [47] - [49]. Only different concentrations of GO dispersion solutions are required to obtain different GO thicknesses via a simple dip coating. This makes the device fabrication process simpler, cost effective, yet functional.

## 2.7 Conclusion

This paper presented a gas sensor using nanoposts-based plasmonic nanostructures coated with a thin GO layer as a resonance tuning in the presence of subtle concentration changes of gas molecules. The sensor exhibits sensitivities of 0.6 pm/ppm to gaseous ethylene, 3.2 pm/ppm to methanol and 12.84 pm/ppm to $NH_3$ gases respectively. An array of sensors was built with the same nanoposts structure but with varying thicknesses of the GO coating. The different responses of the sensors to a gas mixture were collected and a PCA based pattern recognition algorithm was applied to generate a distinct signal cluster for each gas analyte in the mixture. The gas sensor technology reported in this paper will support detection of various gases released from a multitude of sources in the agricultural, biomedical, environmental, and manufacturing fields.

## 2.8 References

[1] B. Esser, J. M. Schnorr, and T. M. Swager, "Selective detection of ethylene gas using carbon nanotube-based devices: utility in determination of fruit ripeness", Angew. Chem. Int. Ed., vol. 51, pp. 5752-5756, 2012.

[2] G. E. Schaller, "Ethylene and the regulation of plant development", BMC Biology, vol. 9, 2012.

[3] R. Fall, and A. A. Benson, "Leaf methanol - the simplest natural product from plants", Trends in Plant Sci., vol. 1, pp. 296-301, 1996.

[4] W. Jud, E. Vanzo, Z. Li, A. Ghirardo, I. Zimmer, T. D. Sharkey, A. Hansel, and J. -P. Schnitzler, "Effects of heat and drought stress on post-illumination bursts of volatile organic compounds in isoprene-emitting and non-emitting poplar", Plant, Cell and Environ., vol. 39, pp. 1204-1215, 2016.

[5] N. G. Patel, P. D. Patel, and V. S. Vaishnav, "Indium tin oxide (ITO) thin film gas sensor for detection of methanol at room temperature", Sens. Actuators: B, vol. 96, pp. 180-189, 2003.

[6] A. Pathak, S. K. Mishra, and B. D. Gupta, "Fiber-optic ammonia sensor using Ag/$SnO_2$ thin films: optimization of thickness of $SnO_2$ film using electric field distribution and reaction factor", Appl. Optics, vol. 54, pp. 8712-8721, 2015.

[7] S. K. Mishra, S. N. Tripathi, V. Choudhary, and B. D. Gupta, “SPR based fibre optic ammonia gas sensor utilizing nanocomposite film of PMMA/reduced graphene oxide prepared by in situ polymerization”, Sens. Actuators: B Chem., vol. 199, pp. 190-200, 2014.

[8] S. K. Mishra, D. Kumari, and B. D. Gupta, “Surface plasmon resonance based fiber optic ammonia gas sensor using ITO and polyaniline”, Sens. Actuators: B Chem., vol. 171-172, pp. 976-983, 2012.

[9] T. E. Brook, and R. Narayanaswamy, “Polymeric films in optical gas sensors”, Sens. Actuators: B, vol. 51, pp. 77-83, 1998.

[10] C. -S. Cheng, Y. -Q. Chen, and C. -J. Lu, “Organic vapour sensing using localized surface plasmon resonance spectrum of metallic nanoparticles self assemble monolayer”, Talanta, vol. 73, pp. 358-365, 2007.

[11] M. Cittadini, M. Bersani, F. Perrozzi, L. Ottaviano, W. Wlodarski, and A. Martucci, “Graphene oxide coupled with gold nanoparticles for localized surface plasmon resonance based gas sensor”, Carbon, vol. 69, pp. 452-459, 2014.

[12] S. K. Mishra, and B. D. Gupta, “Surface plasmon resonance-based fiber optic chlorine gas sensor utilizing indium-oxide-doped tin oxide film”, J. of Lightwave Tech., vol. 33, pp. 2770-2776, 2015.

[13] S. K. Mishra, S. N. Tripathi, V. Choudhary, and B. D. Gupta, “Surface plasmon resonance-based fiber optic methane gas sensor utilizing graphene-carbon nanotubes-poly(methyl methacrylate) hybrid nanocomposite”, Plasmonics, vol. 10, pp. 1147-1157, 2015.

[14] S. K. Mishra, S. P. Usha, and B. D. Gupta, “A lossy mode resonance-based fiber optic hydrogen gas sensor for room temperature using coatings of ITO thin film and nanoparticles”, Meas. Sci. Technol., vol. 27, pp. 045103, 2016.

[15] H. Xu, P. Wu, C. Zhu, A. Elbaz, and Z. Z. Gu, “Photonic crystal for gas sensing”, J. of Mater. Chem. C, vol. 1, pp. 6087-6098, 2013.

[16] N. A. Yebo, P. Lommens, Z. Hens, and R. Baets, “An integrated optic ethanol vapor sensor based on a silicon-on-insulator microring resonator coated with a porous ZnO film”, Opt. Express, vol. 18, pp. 11859-11866, 2010.

[17] Z. Han, P. Lin, V. Singh, L. Kimerling, J. Hu, K. Richardson, A. Agarwal, and D. T. H. Tan, “On-chip mid-infrared gas detection using chalcogenide glass waveguide”, Appl. Phys. Lett., vol. 108, pp. 141106, 2016.

[18] J. N. Anker, W. P. Hall, O. Lyandres, N. C. Shah, J. Zhao, and R. P. V. Duyne, “Biosensing with plasmonic nanosensors”, Nat. Mater., vol. 7, pp. 442-453, 2008.

[19] N. -F. Chiu, T. -Y. Huang, and H. -C. Lai, “Graphene oxide based surface plasmon resonance biosensors”, InTech, ch. 8, 2013.

[20] J. I. L. Chen, Y. Chen, and D. S. Ginger, “Plasmonic nanoparticle dimers for optical sensing of DNA in complex media”, J. AM. Chem. Soc., vol. 132, pp. 9600-9601, 2010.

[21] M. A. Ali, S. Tabassum, Q. Wang, Y. Wang, R. Kumar, and L. Dong, “Plasmonic-electrochemical dual modality microfluidic sensor for cancer biomarker detection”, 2017 IEEE 30th International Conference on Micro Electro Mechanical Systems (MEMS), Las Vegas, pp. 390-393, 2017.

[22] K. Aslan, J. R. Lakowicz, and C. D. Geddes, “Nanogold plasmon resonance-based glucose sensing. 2. Wavelength-ratiometric resonance light scattering”, Anal. Chem., vol. 77, pp. 2007-2014, 2005.

[23] D. Chen, H. Feng, and J. Li, “Graphene oxide: preparation, functionalization, and electrochemical applications”, Chem. Rev., vol. 112, pp. 6027-6053, 2012.

[24] S. S. Nanda, D. K. Yi, and K. Kim, “Study of antibacterial mechanism of graphene oxide using Raman spectroscopy”, Sci. Rep., vol. 6, pp. 28443, 2016.

[25] G. Lu, L. E. Ocola, and J. Chen, “Gas detection using low-temperature reduced graphene oxide sheets”, Appl. Phys. Lett., vol. 94, pp. 083111, 2009.

[26] J. T. Robinson, F. K. Perkins, E. S. Snow, Z. Wei, and P. E. Sheehan, “Reduced graphene oxide molecular sensors”, Nano Lett., vol. 8, pp. 3137-3140, 2008.

[27] S. Tabassum, Q. Wang, W. Wang, S. Oren, M. A. Ali, R. Kumar, and L. Dong, “Plasmonic crystal gas sensor incorporating graphene oxide for detection of volatile organic compounds”, 2016 IEEE 29th International Conference on Micro Electro Mechanical Systems (MEMS), Shanghai, pp. 913-916, 2016.

[28] N. A. Joy, M. I. Nandasiri, P. H. Rogers, W. Jiang, T. Varga, S. V. N. T. Kuchibhatla, S. Thevuthasan, and M. A. Carpenter, “Selective plasmonic gas sensing: $H_2$, $NO_2$, and CO spectral discrimination by a single Au-$CeO_2$ nanocomposite film”, Anal. Chem., vol. 84, pp. 5025-5034, 2012.

[29] S. Tabassum, R. Kumar, and L. Dong, “Plasmonic crystal-based gas sensor toward an optical nose design”, IEEE Sens. J., vol. 17, pp. 6210-6223, 2017.

[30] C. Y. Lee, and M. S. Strano, “Understanding the dynamics of signal transduction for adsorption of gases and vapors on carbon nanotube sensors”, Langmuir, vol. 21, pp. 5192-5196, 2005.

[31] A. Vakil, and N. Engheta, “Transformation optics using graphene”, Science, vol. 332, pp. 1291-1294, 2011.

[32] B. Yao, Y. Wu, Y. Cheng, A. Zhang, Y. Gong, Y. -J. Rao, Z. Wang, and Y. Chen, "All-optical Mach-Zehnder interferometric $NH_3$ gas sensor based on graphene/microfiber hybrid waveguide", Sens. Actuators B: Chem., vol. 194, pp. 142-148, 2014.

[33] H. F. Ghaemi, T. Thio, and D. E. Grupp, "Surface plasmons enhance optical transmission through subwavelength holes," Phys. Rev. B, vol. 58, pp. 6779-6782, 1998.

[34] E. D. Palik, "Handbook of optical constants of solids", New York, NY, USA: Academic, 1985.

[35] Y. Shen, J. Zhou, T. Liu, Y. Tao, R. Jiang, M. Liu, G. Xiao, J. Zhu, Z. -K. Zhou, X. Wang, C. Jin, and J. Wang, "Plasmonic gold mushroom arrays with refractive index sensing figures of merit approaching the theoretical limit", Nat. Commun., vol. 4, pp. 2381, 2013.

[36] J. Xu, P. Kvasnička, M. Idso, R. W. Jordan, H. Gong, J. Homola, and Q. Yu, "Understanding the effects of dielectric medium, substrate, and depth on electric fields and SERS of quasi-3D plasmonic nanostructures", Opt. Express, vol. 19, pp. 20493-20505, 2011.

[37] Q. Wang, W. Han, P. Liu, and L. Dong, "Electrically tunable quasi-3-D mushroom plasmonic crystal", J. of Lightwave Tech., vol. 34, pp. 2175-2181, 2016.

[38] M. Seredych, and T. J. Bandosz, "Mechanism of ammonia retention on graphite oxides: role of surface chemistry and structure", J. Phys. Chem. C, vol. 111, pp. 15596-15604, 2007.

[39] D. R. Dreyer, S. Park, C. W. Bielawski, and R. S. Ruoff, "The chemistry of graphene oxide", Chem. Soc. Rev., vol. 39, pp. 228-240, 2010.

[40] A. J. Roche, "Ch08 Reacns of alkenes (landscape).doc", Rutgers University.

[41] J. Liu, Y. Sun, and X. Fan, "Highly versatile fiber-based optical Fabry-P*é*rot gas sensor", Opt. Express, vol. 17, pp. 2731-2738, 2009.

[42] J. Hromadka, B. Tokay, S. James, R. P. Tatam, and S. Korposh, "Optical fibre long period grating gas sensor modified with metal organic framework thin films", Sens. Actuators B: Chem., vol. 221, pp. 891-899, 2015.

[43] S. K. Mishra, S. Bhardwaj, and B. D. Gupta, "Surface plasmon resonance-based fiber optic sensor for the detection of low concentrations of ammonia gas", IEEE Sens. Journal, vol. 15, pp. 1235-1239, 2015.

[44] B. Mehta, K. D. Benkstein, S. Semancik, and M. E. Zaghloul, "Gas sensing with bare and graphene-covered optical nano-antenna structures", Sci. Rep., vol. 6, pp. 21287, 2016.

[45] A. J. Haes, and R. P. V. Duyne, “A unified view of propagating and localized surface plasmon resonance biosensors”, Anal. Bioanal. Chem., vol. 379, pp. 920-930, 2004.

[46] E. Kretschmann, and H. Raether, “Radiative decay of non radiative surface plasmons excited by light”, Z. Naturforsch, vol. 23, pp. 2135-2136, 1968.

[47] A. Berna, “Metal oxide sensors for electronic noses and their application to food analysis”, Sens., vol. 10, pp. 3882-3910, 2010.

[48] N. E. Barbri, A. Amari, M. Vinaixa, B. Bouchikhi, X. Correig, and E. Llobet, “Building of a metal oxide gas sensor-based electronic nose to assess the freshness of sardines under cold storage”, Sens. Actuators B: Chem., vol. 128, pp. 235-244, 2007.

[49] M. O’Connell, G. Valdora, G. Peltzer, and R. M. Negri, “A practical approach for fish freshness determinations using a portable electronic nose”, Sens. Actuators B: Chem., vol. 80, pp. 149–154, 2001.

# CHAPTER 3. NANOPATTERNED OPTICAL FIBER TIP FOR GUIDED MODE RESONANCE AND APPLICATION TO GAS SENSING

A paper published in IEEE Sensors Journal

Shawana Tabassum, Ratnesh Kumar, and Liang Dong

## 3.1 Abstract

This paper reports on an efficient and convenient method of patterning nanostructures on the cleaved facet of an optical fiber to realize a high-performance fiber-optic gas sensor. The fabrication method utilizes an ultraviolet assisted nanoimprint lithography to transfer nanoscale patterns from a pre-formed stamp to the fiber tip. The novelty of this work lies in utilizing simpler fabrication steps with better control over angle of contact at the fiber tip, which leads to rapid and precise formation of nanostructures with well-defined features. A periodic array of polymer nanoposts are formed at the fiber tip and coated with titanium dioxide to serve as a guided mode resonant (GMR) device. A gas sensor is realized by coating the GMR structure with a thin layer of graphene oxide (GO) nanosheets. We have utilized the resonance sensitivity of the nanopatterned fiber-tip gas sensor to surrounding refractive index. The abundant functional groups available at GO provides an effective adsorption surface for gas molecules. Microscopic imaging and spectroscopic studies are conducted to illustrate the structural and optical properties, and gas-sensing performance of the sensor. Volatile organic compounds such as ethylene and methanol, associated with crop plant health, are detected by the sensor. The sensor provides sensitivities of 0.92 pm/ppm and 1.37 pm/ppm for ethylene and methanol vapors, respectively, with a three-fold enhancement in sensitivity and 50% reduction in response time compared to the non-GO coated counterpart. The sensor has good stability and reproducibility, having a great potential in fiber-optic remote sensing applications.

## 3.2 Introduction

Nanostructuring is one of the most explored platforms in the nanophotonics area due to its light control property at the nanoscale. There are several studies for nanopatterning by incorporating metal or metal oxide to realize sub-wavelength structures for resonant field confinement and enhancement [1], [2]. Some of these structures have been employed for sensing applications such as liquid-phase detection of proteins [3], DNA [4], glucose [5], and cancer biomarkers [6], and gas-phase detection of various molecules [7-9]. However, the relatively large overall device size of these structures and the complex optical coupling systems do not allow them to be easily inserted into remote regions (as in endoscopy). The ability of creating high-resolution nanopatterns on the micron size tip of optical fiber has a potential of remote sensing applications, with different detection devices such as diffraction gratings, photonic crystals, and micro-ring resonators. Yet, the number of studies on patterning the tips of optical fibers and utilizing them as a sensing mechanism is limited. This paper reports on our contributions in the above context.

The implementation of fiber-tip based sensor can offer numerous advantages, especially in terms of elimination of bulky optics and easy insertion of the device to sensing area. The microscopic cross-section size and high mechanical flexibility of optical fibers allow in-vivo, remote diagnostic detection. A number of approaches have been pursued wherein the fiber end facet has been modified to realize structures capable of detecting analyte molecules. For example, localized surface plasmon resonance based fiber-tip probes have been realized for ultrasensitive detection of protein biomarkers [10], [11]. A fiber tip-based Fabry-Perot gas sensing probe composed of a silver layer and a vapor-sensitive polymer layer has also been developed for detection of methanol, acetone, and hexanol vapors [12]. In addition, a combination of fiber tip-based evanescent field and quartz-enhanced photoacoustic sensor has

been recently utilized to detect carbon monoxide [13]. However, due to the lack of suitable absorption materials for detecting gas molecules, the sensitivity to surrounding gas concentrations remains a challenge. Recently, graphene oxide (GO) has been utilized in the development of highly sensitive sensors as it possesses many unique properties such as high surface-area-to-volume ratio [14], [15] and variety of functional groups (e.g., carboxyl, hydroxyl, carbonyl and epoxide) at the GO surface, providing traps for gas species [16]. Although GO and GO-based nanocomposites have been used extensively on conventional planar substrates for sensing gas species [17]-[19], few studies exist on integrating GO nanosheets at the optical fiber tip to explore sensing applications [20]. In this paper we report below our findings on GO-layer induced enhanced sensitivity, towards the fiber-optic measurement of gas concentrations.

Several fabrication processes have been reported to pattern unconventional substrates including optical fiber tips. The standard technologies, such as electron beam lithography (EBL) [10], [21], reactive ion etching [10], [22], and liftoff [11] were utilized to pattern nanostructures on fiber facets. Although these methods can produce repeatable patterns, spin coating resist and etching are challenging on fiber facets because of their small size, non-planarity and mechanical flexibility. An alternative approach used evaporation to deposit resist at the fiber tip, which eliminated the need of spin coating the resist [23]. However, the requirements of specialized vacuum equipment and resist made the process intricate. Obtaining a thin and uniform resist layer for high resolution patterning at fiber tip using EBL remains a challenge. In addition, the focused ion beam (FIB) was employed as a direct writing approach to efficiently mill a regular lattice of nanoholes [24] and microchannels [25] on fiber facets. However, the fabrication process is not defect free due to unwanted ion doping and angled

sidewalls of the patterned structure [25]. Moreover, due to the serial FIB milling process, fabricating complex patterns at the fiber tip is time consuming. Furthermore, nanoskiving technique [26] was explored to pattern an array of metallic nanostructures on a fiber tip. However, the mechanical stress and the structural folding induced during nanoskiving make the yield of this process low [26]. Recently, nanoimprint lithography (NIL) [27] emerged as an attractive patterning technique due to its ultrahigh resolutions, simplicity, and cost-effectiveness. Since NIL relies on direct mechanical deformation of resist material, it can achieve resolution limit down to sub-10nm region. These features of NIL make it a good candidate for fiber tip patterning. An ultraviolet (UV) based NIL method has already been reported for fiber tip patterning, but it requires non-trivial inclined UV incidence making the process tedious [28]. Our paper reports some key improvements, summarized at the end of this section.

In this paper, we demonstrate a simple and efficient method to inscribe high-resolution nanophotonic patterns on the cleaved facets of optical fibers using UV assisted NIL [29], [30]. The nanostructured patterns are made of SU8 photoresist and coated by a thin layer of titanium dioxide ($TiO_2$) in order to form a fiber optic sensor utilizing guided mode resonance (GMR) and its shift when exposed to analytes. The resonance shift is due to the leaky modes of the GMR structure that allows for the interaction with the analyte on its structure surface. The incident light energy is coupled to these radiated leaky modes. Since the deposited $TiO_2$ at the fiber tip acts as a light confinement layer, the device works as a high contrast grating in which the optical field associated with the GMR modes is evanescently confined near the surface. The successful transfer of nanostructures of different forms to the fiber tip is confirmed by scanning electron microscopy (SEM) and optical spectroscopy. To our knowledge, this is the

first guided mode resonant structure that has been integrated on a fiber tip. This fiber tip patterning technology allows producing fiber-optic sensors for remote in-field measurements in biomedical, environmental, agricultural, and other applications. This work resulted in the publications [31] and [32].

Measurements of the GMR resonance shift in the presence of the gas analytes near the fiber tip surface are performed to validate the workability of the nanostructures as a fiber-optic sensor. The GMR device is further coated with a thin layer of GO nanosheets to enhance gas adsorption at the fiber tip. Sensitivity and reproducibility studies are also performed for the proposed sensor. In summary, the contributions of this work are as follows:

- Simple and efficient process for nanopatterning the optical fiber tip.
- A comprehensive physics-based explanation of the functioning of the device as the light passes through the fiber and hits the $TiO_2$ coated grated waveguide structure at the fiber tip.
- A complete characterization of $TiO_2$ coated nanopatterns transferred to the fiber tip.
- Utilization of the GO-coated GMR structure to monitor surrounding refractive index changes in response to the changing concentrations of the analytes.
- Application to gas sensing and characterization for methanol and ethylene.

### 3.3 Device Fabrication

The device fabrication process starts from preparing a flat-cleaved fiber tip and a transparent master mold with patterns made on a glass wafer. First, an array of nanoposts was formed on a glass wafer using soft lithography based replica nanomolding process. Next, the nanopatterns were transferred from the glass to the fiber tip using a low-viscous UV curable resist. This UV-NIL technique circumvents the need to apply the lithography processes directly

to smaller fiber facet. Instead, a larger carrier wafer was processed first, and then using UV-NIL, the nanostructures were transferred from the carrier to the fiber tip.

### 3.3.1 Mold Preparation

Preparation of a glass wafer mold carrying nanoposts consists of a number of steps depicted in Fig. 3.1(a-d), followed by their transfer to the fiber tip as in Fig. 3.1 (e-g).

First, a polydimethylsiloxane (PDMS) mold was formed from a silicon (Si) master mold. The Si master mold with nanopatterns was silanized by (tridecafluoro-1, 1, 2, 2-tetrahydrooctyl)-1-trichlorosilane (T2492-KG, United Chemical Technologies) in a desiccator under vacuum condition for 20 min. Subsequently, an s-PDMS precursor solution was prepared by mixing Sylgard 184 (Dow Corning) and curing agent at the weight ratio of 10:1 and degassed in a vacuum desiccator for 20 min. The s-PDMS mixture was then poured onto the top surface of silanized Si mold and cured on a hotplate at 65$^{o}$C for 2 hrs (Fig. 3.1a). After that, the PDMS slab containing a square array of nanoholes was peeled from the Si mold (Fig. 3.1b). Next, a UV curable polymer (ZIPCONE™ UA or ZPUA) was used to imprint the nanopatterns from the PDMS mold to the glass wafer [Fig. 3.1(c-d)]. At first, the glass wafer was spin coated with an adhesive layer of Transpin at 3000 rpm for 40s and subsequently heated at 200 $^{0}$C for 5 min. This step is required to enhance the adhesion ability of ZPUA to glass wafer resulting in complete transfer of ZPUA nanoposts to the glass. Next, ZPUA was dropped on the PDMS mold (Fig. 3.1c) and the mold was then placed on top of the glass wafer. Then the wafer was exposed to UV light for 5 min at an intensity of 3.3 mW/cm$^{2}$ (Fig. 3.1d). Separation of the PDMS mold from the glass resulted in nanoposts transferred to the glass wafer.

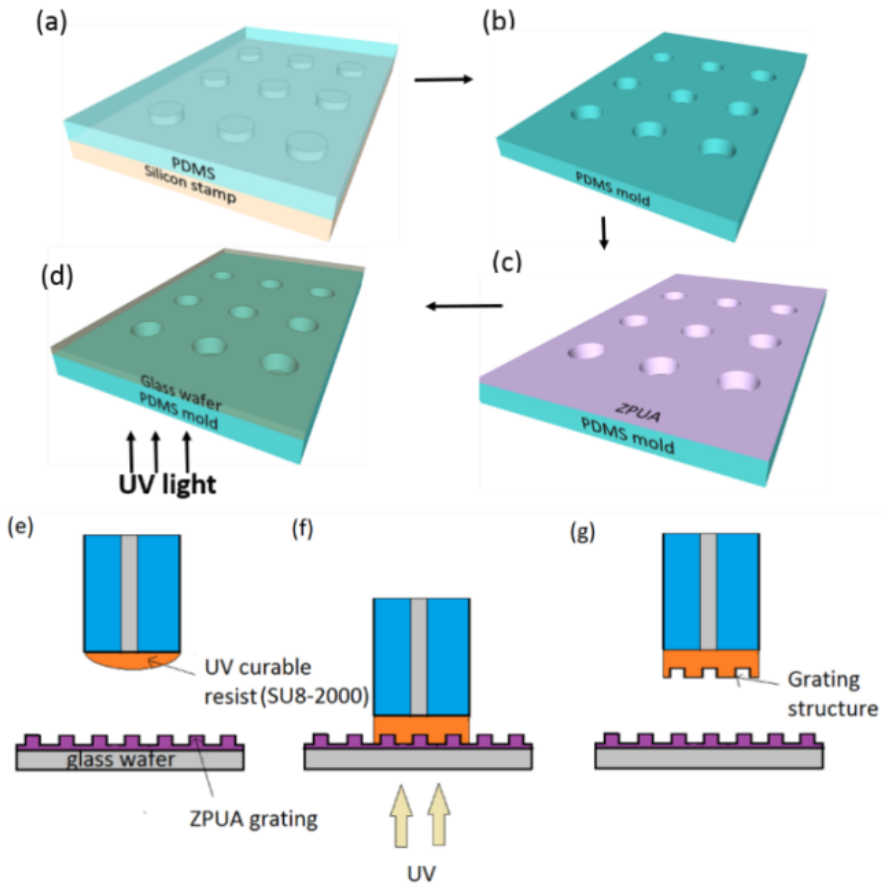


Fig. 3.1: *Fabrication process. (a) PDMS is poured on the silicon stamp and then thermally cured. (b) PDMS is peeled off the stamp. (c) ZPUA is poured on the PDMS mold. (d) The PDMS mold is pressed against the glass wafer and exposed to UV radiation. (e) The fiber tip is dipped into SU8-2000. (f) The fiber is pressed against the grating structure and is subject to UV irradiation. (g) The mold is released from the fiber tip.*

### 3.3.2 Transferring Patterns to Fiber Tip

The first step was to strip the polymer jacket of the fiber with a fiber stripper and to clean the fiber facet using isopropyl alcohol (IPA). The next step was to cleave the stripped multimode fiber (FT200EMT, Thorlabs) using a fiber cleaver to obtain a flat fiber tip. Further, the glass wafer with ZPUA nanoposts was treated with an anti-adhesion coating by salinization in vacuum ($10^{-5}$ mTorr) using trichloro(1H,1H,2H,2H-perfluoro-octyl) silane. The anti-adhesion treatment minimized the adhesion between the glass wafer and the UV-curable resist, thus facilitating easy release of the fiber tip from the mold. The next step was to use a low-

viscous UV curable resist (SU8-2000) to transfer the patterns from the ZPUA mold to the fiber tip. For that, the fiber was first dipped into SU8-2000, and then mounted on an XYZ stage (Fig. 3.1e). It was then gradually approached towards the mold until the tip touched the mold, resulting in filling the grating cavities with the resist (Fig. 3.1f). Subsequently, the fiber tip was exposed to UV light with the intensity of 14 $mW/cm^2$ for 15 min. After the UV irradiation, the fiber tip was lifted from the mold (Fig. 3.1g).

The critical steps of the process flow include selecting a low viscous UV curable resist and finding the optimum UV intensity and exposure time. Highly viscous resist only partially fills the nanoholes resulting in incomplete pattern transfer to fiber tip. Other reports [27] used an opaque substrate such as Si wafer to form the master mold, which required an oblique UV incidence to polymerize the photoresist. As the UV exposure energy needed is sensitive to the angle between the mold and the fiber tip, the energy-control is relatively poor in that setting. In contrast, the energy is more controllable in our case, owing to a transparent mold and a normal incidence light for polymerization.

Next, to form a fiber-tip GMR device, a 160 nm-thick $TiO_2$ layer was deposited using e-beam evaporation at the fiber tip. The $TiO_2$ coated nanopatterned fiber tip was further coated with GO nanosheets to allow gas adsorption and sensing, by measuring a GMR-shift. To prepare GO suspension solution, GO nanosheets were mixed in deionized water (DI-$H_2O$) and sonicated for 90 min. This solution was then diluted to make a certain concentration. The surfaces of three fiber-tip sensors were made hydrophilic by using oxygen plasma treatment before drop-coating with different amounts of GO solutions. A GO dispersion solution with concentration of 0.1 mg/ml (0.1 mg of GO in 1 ml of DI-$H_2O$) was prepared. Three identical fiber-tip sensors were drop-coated by 5 µl of one layer, two layers and three layers of 0.1 mg/ml

GO dispersion solution respectively. These sensors were then dried at room temperature for one hour.

### 3.4 Working Principle and Mathematical Characterization

The nanopatterns at the fiber tip were designed to have a period of 500 nm, the hole diameter of 250 nm, and the hole height of 210 nm. The nanoholes coated with the 160 nm-thick $TiO_2$ layer acts as a GMR device as light passes from the fiber to the $TiO_2$ layer and is then detected by the detector. Resonance occurs when there is a phase matching of excitation light with a GMR mode. This significantly enhances the near-field intensity associated with the GMR modes and is also sensitive to the changes in the surrounding refractive index.

As shown in Fig. 3.2, the present structure is a three-layered dielectric waveguide-grating composed of a polymer layer (SU-8) of refractive index $\eta_{su8} = 1.6$, a grated $TiO_2$ layer of average refractive index $\eta_{avg}$ , and a surrounding medium (air) of refractive index $\eta_{air} = 1$ (air). The grated layer consists of alternating high index ($\eta_H = \eta_{TiO2} = 2.49$) and low index ($\eta_L = \eta_{air} = 1$) materials. $\eta_{avg}$ can be expressed by the following equation [33]:

$$\eta_{avg} = \sqrt{\eta_L^2 + f(\eta_H^2 - \eta_L^2)}, \qquad (3.1)$$

where $f$ is the *fill factor* (fraction of the grating containing the high refractive index material). For the proposed structure, $f = 0.5$ and hence $\eta_{avg} = 1.904$. The average refractive index $\eta_{avg}$ of the grating structure must be greater than that of the substrate and the medium above to allow total internal reflection and light confinement. The sub-wavelength grating couples the incident light into a strongly confined mode of the waveguide structure, leading to a guided mode resonance. The resonance wavelength and the angle of total internal reflection due to the guided mode can be obtained by ignoring the material dispersion. For transverse-electric (TE) polarization, the wave propagation in an asymmetric waveguide grating can be expressed by

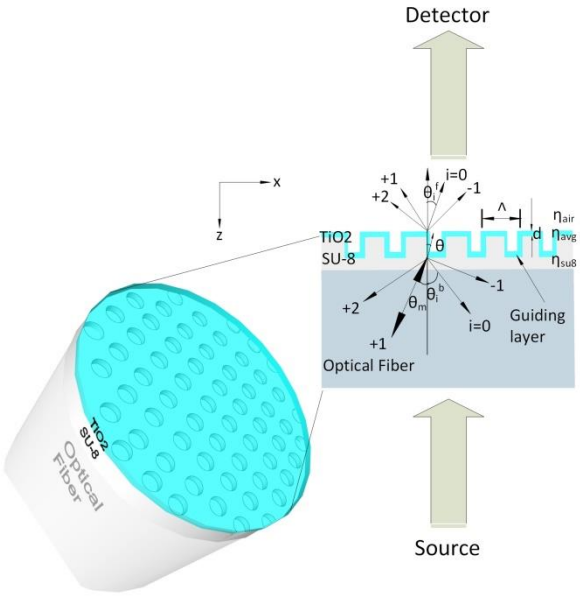


Fig. 3.2: *Schematic representation of planar waveguide-grating at the optical fiber tip, where the angles, $\theta_m$ is of incident light, $\theta_i^b$ is of the ith backward-diffracted wave, and $\theta_i^f$ is of the ith forward-diffracted wave.*

the coupled-wave equation as follows [34]:

$$\frac{d^2E_i(z)}{dz^2} + [\beta^2\eta_{avg}^2 - \beta^2(\eta_{avg}\sin\theta - i\frac{\lambda}{\Lambda})^2]E_i(z) + \frac{1}{2}\beta^2\Delta\eta^2[E_{i+1}(z) + E_{i-1}(z)] = 0 \quad (3.2)$$

where $E_i(z)$ is the electric-field amplitude of the ith space harmonic, $\lambda$ is wavelength of incident light, $\Lambda$ is grating period, $\beta = \frac{2\pi}{\lambda_{GMR}}$ is the propagation constant in the waveguide ($\lambda_{GMR}$ the corresponding wavelength), $\theta$ is internal angle of incidence in the waveguide (Fig. 3.2), and $\Delta\eta = (\eta_H - \eta_L)$ denotes the modulation of the grating structure.

Our goal is to determine the values for $\theta$ and $\beta = \frac{2\pi}{\lambda_{GMR}}$ to know the critical angle and the propagation constant in the grated waveguide. We will first find $\theta$, which actually depends on the allowed mode angles within the fiber core, through which the light passes first. Let $\theta_m$ denote the $m$th mode angle within the fiber core which, in our design, is a multimode fiber (FT200EMT, Thorlabs) with core refractive index, $\eta_{core} = 1.45$ and cladding refractive index,

$\eta_{clad}$ = 1.39. This results in a weakly guided fiber with a fractional refractive index change $\Delta$, calculated from the equation in [35], to be:

$$\Delta = \frac{\eta_{core}^2 - \eta_{clad}^2}{2\eta_{core}^2} = 0.04 << 1 \qquad (3.3)$$

In such a weakly guided fiber, the grouped-together modes behave as linearly polarized modes, which leads to their following characteristic equation [35]:

$$-\sqrt{1-b}\,\frac{J_{m-1}(V\sqrt{1-b})}{J_m(V\sqrt{1-b})} = \sqrt{b}\,\frac{K_{m-1}(V\sqrt{b})}{K_m(V\sqrt{b})}, \qquad (3.4)$$

where $J_m$ is the Bessel function of the first kind, $K_m$ is the modified Bessel function of the second kind, $V = 2\pi\frac{a}{\lambda}\sqrt{\eta_{core}^2 - \eta_{clad}^2}$ with the fiber core diameter $2a = 200\mu m$, and $b = \frac{\eta_{eff}^2 - \eta_{clad}^2}{\eta_{core}^2 - \eta_{clad}^2}$ with $\eta_{eff} = \eta_{core} \sin\theta_m$.

It can be seen that the only unknown in Eq. (3.4) is the mode angle $\theta_m$ in the fiber. This equation can be solved graphically by plotting right and left hand sides versus $b$ and finding the intersections. From the value of $b$, the allowed mode angles $\theta_m$ inside the fiber core can be determined. Next the angle $\theta$ can be found using the following equation, of the grating, that relates the two angles:

$$\eta_H \sin\theta - \eta_{core} \sin\theta_m = i\frac{\lambda}{\Lambda} \qquad (3.5)$$

Note for the ith space harmonic guided wave to exist in the grated waveguide structure, the angle must also satisfy:

$$\max(\eta_{air}, \eta_{su8}) \leq \eta_{avg} \sin\theta - i\frac{\lambda}{\Lambda} < \eta_{avg} \qquad (3.6)$$

Once $\theta$ is known by solving (3.5) and also satisfying the constraint of (3.6), an eigenvalue equation can be employed to find $\beta$. For the case of TE polarization, the eigenvalue of the modulated waveguide is given by [36]:

$$\tan(k_i d) = \frac{k_i(\gamma_i + \delta_i)}{k_i^2 - \gamma_i \delta_i}, \qquad (3.7)$$

where $d$ is the thickness of the $TiO_2$ layer, $k_i = \sqrt{\beta^2 \eta_{avg}^2 - \beta_i^2}$, $\gamma_i = \sqrt{\beta_i^2 - \beta^2 \eta_{air}^2}$, $\delta_i = \sqrt{\beta_i^2 - \beta^2 \eta_{su8}^2}$, and $\beta_i = \beta(\eta_{avg} \sin\theta - i\frac{\lambda}{\Lambda})$ denotes the effective propagation constant of waveguide grating. On the other hand, for the transverse-magnetic (TM) polarization, the eigenvalue can be expressed as [36]:

$$\tan(k_i d) = \frac{\eta_{avg}^2 k_i(\eta_3^2 \gamma_i + \eta_1^2 \delta_i)}{\eta_1^2 \eta_3^2 k_i^2 - \eta_{avg}^2 \gamma_i \delta_i} \qquad (3.8)$$

Eq. (3.7) for TE modes or Eq. (3.8) for TM modes can be solved numerically to find $\beta$, which is the only remaning unknown in those equations. This in turn can be used to find the guided mode resonance wavelength, $\lambda_{GMR} = \frac{2\pi}{\beta}$. It can be observed that any changes in the surrounding refractive index $\eta_L$ will lead to a change in $\eta_{avg}$, causing a shift of resonant wavelength and establishing our working principle.

## 3.5 Results and Discussion

### 3.5.1 Characterization of Nanopatterns at Fiber Tip

The fiber tip was observed under a stereomicroscope (Leica, 205FA). The corresponding reflective color patterns from the grating patterned at the fiber tip for different incident angles were observed (Fig. 3.3).

The SEM analysis was performed to characterize the nanopatterns transferred to the fiber tip (Fig. 3.4). The square lattice of nanoholes at the fiber tip with pitch of 500 nm and groove depth of 210 nm (Fig. 3.4b), was used as a gas sensor (described later in the Application to Gas Sensing section). It was also confirmed from this SEM image that full coverage of the nanoholes is achieved when coated with a 160 nm-thick $TiO_2$ layer (Fig. 3.4c). Figure 3.4d

shows the $TiO_2$ coated nanoholes further covered with 0.5 mg/ml dispersion solution of GO nanosheets, and verifies the uniformity and adherence of the GO coating on the fiber tip. The reproducibility of our process was confirmed by fabricating $TiO_2$/GO layered nanoholes at the tips of three identical optical fibers, as shown in Figs. 3.4d-f. In addition, four other types of nanostructures were transferred to optical fiber tips using the same fabrication steps as illustrated in Figs. A.1a-A.1d presented at the end, in an appendix. Fig. A.1a illustrates the nanoposts having pitch of 500 nm and groove depth of 150 nm with triangular lattice, whereas Figs. A.1b, A.1c and A.1d depict, respectively, the nanoholes (pitch of 700 nm and groove depth of 150 nm) with triangular lattice, nanoposts (pitch of 500 nm and groove depth of 210 nm) with square lattice, and linear nanostamps (pitch of 700 nm and groove depth of 150 nm). To visualize the complete structure transferred to the fiber tip, a $75^0$ tilted view of the linear stamps was captured to reveal the height of the nanostamps at the tip (Fig. A.1e). Moreover, the height of remaining polymer beneath the nanoposts was also observed, which was approximately 880 nm (Fig. A.1f). This clearly demonstrates the versatility of our pattern transfer process (as explained in the Device Fabrication section) to realize different types of nanostructures at the fiber tip.

For sensing purposes, only the fiber tip patterned with square lattice of nanoholes (Fig. 3.4) was utilized. Different structures were designed, mainly to establish the fabrication capability of our process, and also to conduct an initial structural optimization with respect to sensor sensitivity.

Further, we conducted Raman spectroscopy to characterize the GO coating at the fiber tip. The Raman spectrum of GO depicts the characteristic peaks of D and G at 1354 $cm^{-1}$ and 1598 $cm^{-1}$ respectively (Fig. 3.5). The G band is associated with C-C bond stretch in $sp^2$ carbon

domains and the D band appears due to the presence of disorders in the GO nanosheets as also explained in [37].

### 3.5.2 Bulk Refractive Index Change Characterizations

The optical properties of the GMR structure at the fiber tip were measured by coupling a white light from a halogen light source (150 watt quartz halogen lamp, Luxtec Fiber Optics) into the multimode fiber carrying nanopatterns at the tip. The device fiber was next coupled to another multimode fiber through a slotted mating sleeve (ADAF1, Thorlabs). The transmitted light was collected from the multimode fiber into a spectrometer (USB4000, Ocean Optics) (Fig. 3.6).

The measured transmission spectrum for a 2D nanohole array, with square lattice at the fiber tip coated with a 160 nm-thick layer of $TiO_2$, is shown in Fig. 3.7a, where the interaction of light with the grating structure resulted in a dip $D_{e1}$. Note that another dip, $D_{e2}$ occurred in the measured spectra. However, it can be observed that with a change in surrounding refractive index, only the first dip $D_{e1}$ changes significantly compared to $D_{e2}$, meaning that it is the first dip $D_{e1}$ that represents the GMR mode. Next, we performed index sensitivity measurements of the fiber-tip GMR structure in three different liquids. The slotted fiber mating sleeve (Fig. 3.6) allowed easy exposure of nanopatterned fiber tip to the chemicals. As the surrounding medium of the fiber tip was changed by introducing water ($\eta_{water} = 1.33$), acetone ($\eta_{acetone} = 1.36$),

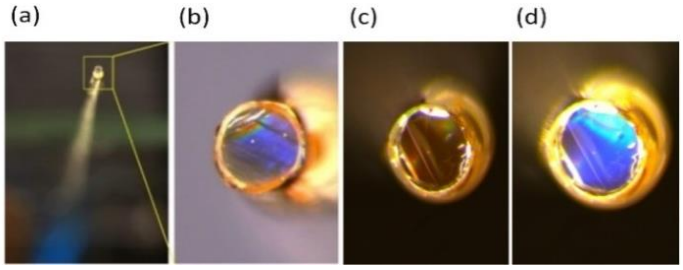


Fig. 3.3: *(a) Optical image of a multimode fiber with the tip patterned with nanostructures. (b, c, d) Reflective colors from the 2D GMR patterns at the fiber tip for different incidence angles of light.*

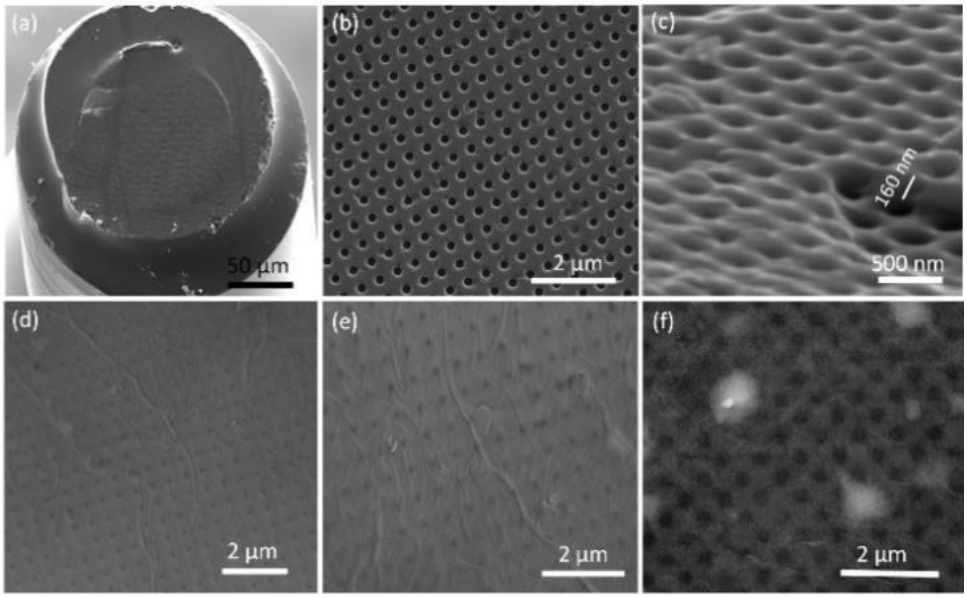


Fig. 3.4: *SEM analysis of the fiber tip: (a) optical fiber tip patterned with nanoholes, (b) zoomed-in top-view SEM image of bare (without GO/$TiO_2$ coating) nanoholes in (a), (c) coverage and thickness of $TiO_2$ coating on the nanoholes, (d-f) GO/$TiO_2$ coated nanoholes at the tips of three identical optical fibers.*

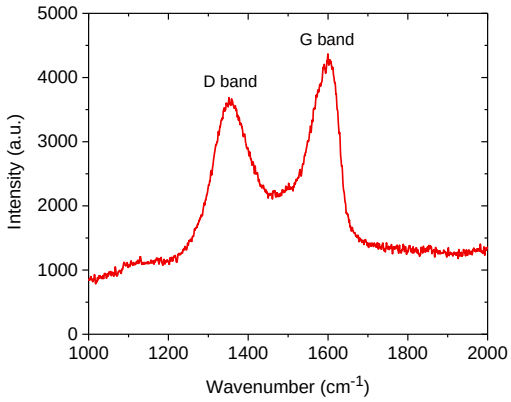


Fig. 3.5: *Raman spectrum of Graphene oxide.*

and IPA ($\eta_{IPA} = 1.38$), on the fiber tip, the resonance wavelength shifted to 813 nm, 819 nm and 821.5 nm respectively. The higher the surrounding refractive index, the larger the observed resonance shift. Based on these measurements, the device exhibited an index sensitivity of 183.3 nm/RIU (plotted in Fig. 7b).

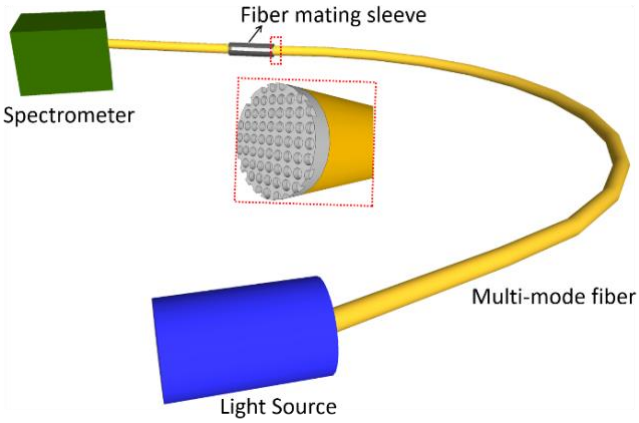


Fig. 3.6: *Optical setup for transmission measurement.*

Electromagnetic simulations were carried out using commercial software DiffractMOD (RSoft Synopsis) to analyze the optical properties of the fabricated nanopatterns at the fiber tip. The electric field enhancement of the $TiO_2$ coated GMR structure at the resonant wavelength of 810.75 nm (in air) is depicted in the inset of Fig. 3.7a. The enhancement accounts for the strong confinement of GMR mode by the high-index $TiO_2$ layer (see the field distribution of the GMR mode in the inset of Fig. 3.7a).

Further, transmittance spectra were measured for a 2D nanohole array with triangular lattice and 1D array with linear nanostamps, transferred to the fiber tip (as shown in Fig. A.2 of Supplementary Materials). These 1D and 2D gratings, when coated by $TiO_2$, a high index material, have different resonances, per the GMR theory [38], and also illustrated in Fig. A.2. Four transmittance dips at $D_{T1}$ = 507 nm, $D_{T2}$ = 634 nm, $D_{T3}$ = 711.5 nm, $D_{T4}$ = 797.5 nm and three dips at $D_{L1}$ = 433.5 nm, $D_{L2}$ = 754 nm, $D_{L3}$ = 842.5 nm were observed for the triangular array of nanoholes and linear nanostamps respectively.

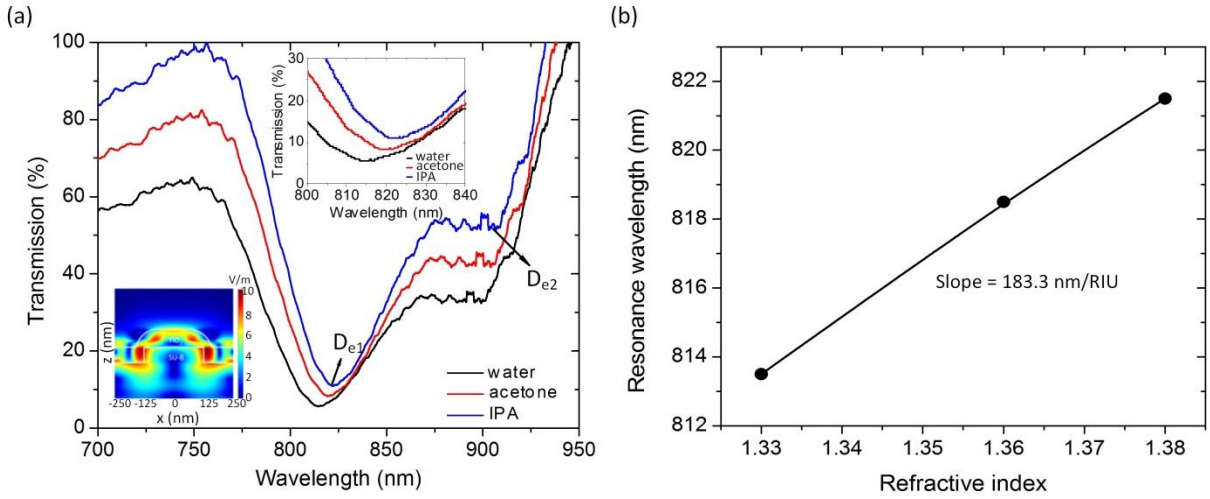


Fig. 3.7: *(a) Experimental transmittance of the device with surrounding water, acetone and IPA. Insets show the close-up of the resonance shift (upper right corner) and field distribution at the resonance mode of the GMR structure (lower left corner). (b) Refractive index sensitivity curve.*

As 2D GMR structures have higher Q-factor than 1D structures (due to low loss) and 2D square lattice resonances are independent of polarization as compared to 2D triangular lattice that produces highly polarization dependent resonances [38], we used only the 2D square array of nanoholes for gas sensing.

### 3.6 Application to Gas Sensing

In this part of the work, we demonstrated the $TiO_2$ coated nanopatterned fiber tip as a gas sensor. An extra coating of GO was applied at the fiber tip and the sensor performance was recorded with and without the GO coating. Without the presence of any gas, the sensor exhibited a resonance at approximately 810.75 nm.

The gas species (pre-diluted with nitrogen) flowed from cylinders into an aluminum chamber which contained the device fiber. The optical setup as illustrated in Fig. 6 was used to illuminate the sensor at the fiber tip as well as to collect the transmitted light. Inside the chamber, the testing gas was further diluted by the carrier nitrogen gas. The gas flow rate was controlled by a mass flow controller (GFC17, Aalborg). Ethylene with concentrations of 857

ppm, 909 ppm and methanol with concentrations of 428 ppm, 454 ppm were tested. A constant flow rate of dry nitrogen (10 ml/min) was maintained inside the closed chamber and flow rate of ethylene and/or methanol was varied to modify the concentration of the test gases at regular intervals using the mass flow meter. In order to ensure that no false spectral shifts occur due to the presence of moisture, dry nitrogen was used to drive away moisture from the chamber before exposing the sensor to gas species.

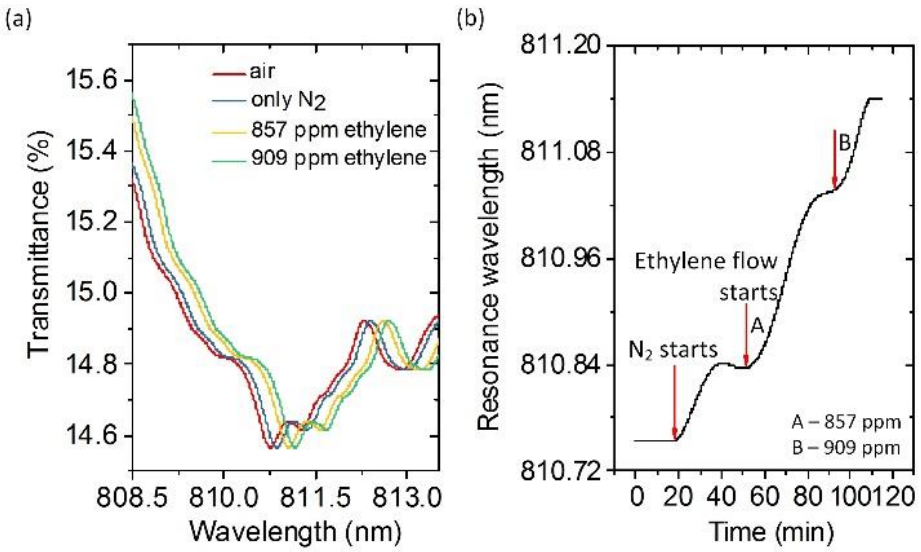


Fig. 3.8: *(a) Transmittance spectra of GMR gas sensor (without any GO coating) at fiber tip when exposed to gaseous ethylene and (b) Monitoring real-time sensing of ethylene with the sensor.*

At first, we tested without any GO coating on the sensor surface. When only nitrogen was introduced into the chamber, the resonance wavelength was red-shifted to 810.85 nm after an interval of approximately 10 min (Fig. 8). The shift in resonance wavelength can be explained theoretically with the help of eqns. (1) - (8). As the surrounding dielectric medium changes from air to nitrogen, $\eta_{avg}$ in eqn. (1) increases and hence we see an increase in GMR wavelength, $\lambda_{GMR}$. The slower response time of the sensor is attributed to the lack of a gas adsorption layer at the sensor surface leading to slower interaction of gas molecules with the

GMR structure. When the sensor response was saturated in the presence of nitrogen gas, ethylene was flown into the chamber. Due to an increase in surrounding refractive index, red-shifts of 0.2 nm and 0.1 nm were observed with 857 ppm and 909 ppm of ethylene respectively as depicted in Fig. 8b. Without any GO coating, the sensor response was quite slow and also there was a very small resonance wavelength shift upon exposure to gases. In order to get a fast, repeatable and more sensitive response, the sensor was further coated with a thin layer of GO nanosheets to form a sensitive surface for adsorbing gas molecules. An array of three sensors was designed wherein each sensor was coated with a different thickness of GO. Fig. 9 shows the resonance spectra of the three sensors with three different thicknesses of GO (48.9 nm, 97.8 nm, and 146 nm) before and after being exposed to ethylene and methanol at different concentrations. With 48.9 nm, 97.8 nm and 146 nm GO coating, the resonance wavelength shifted from 810.75 nm to 811.75 nm, 812 nm and 812.11 nm respectively (Fig. 9). The measurement setup is same as explained above without any GO. However, when a GO coating was used, the sensor response time reduced from 10 min to approximately 5 min. The large number of binding sites available on the GO coating resulted in increased absorption of gas molecules at the sensor surface. As a result, the sensor encountered a higher change in surrounding refractive index and hence a larger resonance wavelength shifts as compared to when there was no GO coating. For example, with 48.9 nm GO coating, resonance wavelength shifts of 0.5 nm and 0.5 nm were observed in response to 857 ppm and 909 ppm ethylene respectively (Fig. 9a) which are approximately 3.3 times higher than the shifts observed without any GO coating. The sensor was further exposed to gaseous methanol, and again large resonance shifts were observed with GO coating as compared to without any GO coating (Fig. 9b). However, too thick a GO coating may result in saturation of binding sites on GO farther

from the sensor surface. This may inhibit the gas molecules from coming in contact with the active portion of sensor surface, leading to a reduction in wavelength shift or no response. This effect is depicted in Fig. 9c. With 146 nm GO coating, less resonance wavelength shifts were observed for 909 ppm ethylene and 454 ppm methanol.

### 3.7 Sensitivity, Kinetics and Reproducibility Studies

We measured the sensitivity of our sensor, and compared that with existing studies. The sensitivity of the fiber-tip sensor to gaseous ethylene without any GO coating (Fig. 3.8) was found to be 0.277 pm/ppm. However, the sensitivities of the same sensor to gaseous ethylene and methanol with GO coating (Fig. 3.9c) were found to be approximately 0.92 pm/ppm and 1.37 pm/ppm respectively. Hence, the presence of GO coating resulted in a three-fold increase in sensitivity to ethylene. In addition, the response time of the GO coated sensor decreased by half as compared to no GO coating.

A fiber-tip based FP sensor exhibited a sensitivity of 3.53 pm/ppm for methanol vapor [12], which is higher than ours, but our fiber-tip sensor offers other advantages. Firstly, it is superior in terms of fabrication method. The FP sensor is comprised of a silver coating and a vapor sensitive polymer layer. The electroless plating method was used for the silver coating [12], which required precise control of plating parameters such as temperature and concentration of chemicals. In contrast, our sensor employs inexpensive and simple nanomolding and UV-NIL processes to fabricate nanopattern-based GMR structure. Furthermore, in order to selectively identify gas species, different polymer materials were used (PEG 400 and NOA 81) in the FP fiber-tip sensor. But in our work, by simply varying the thicknesses of the GO coatings on the sensing elements in a sensor array, it is possible to differentiate one gas from others in a gas mixture using pattern recognition algorithms. There is no need of changing the structures of nanoposts that otherwise will require costly nanoscale

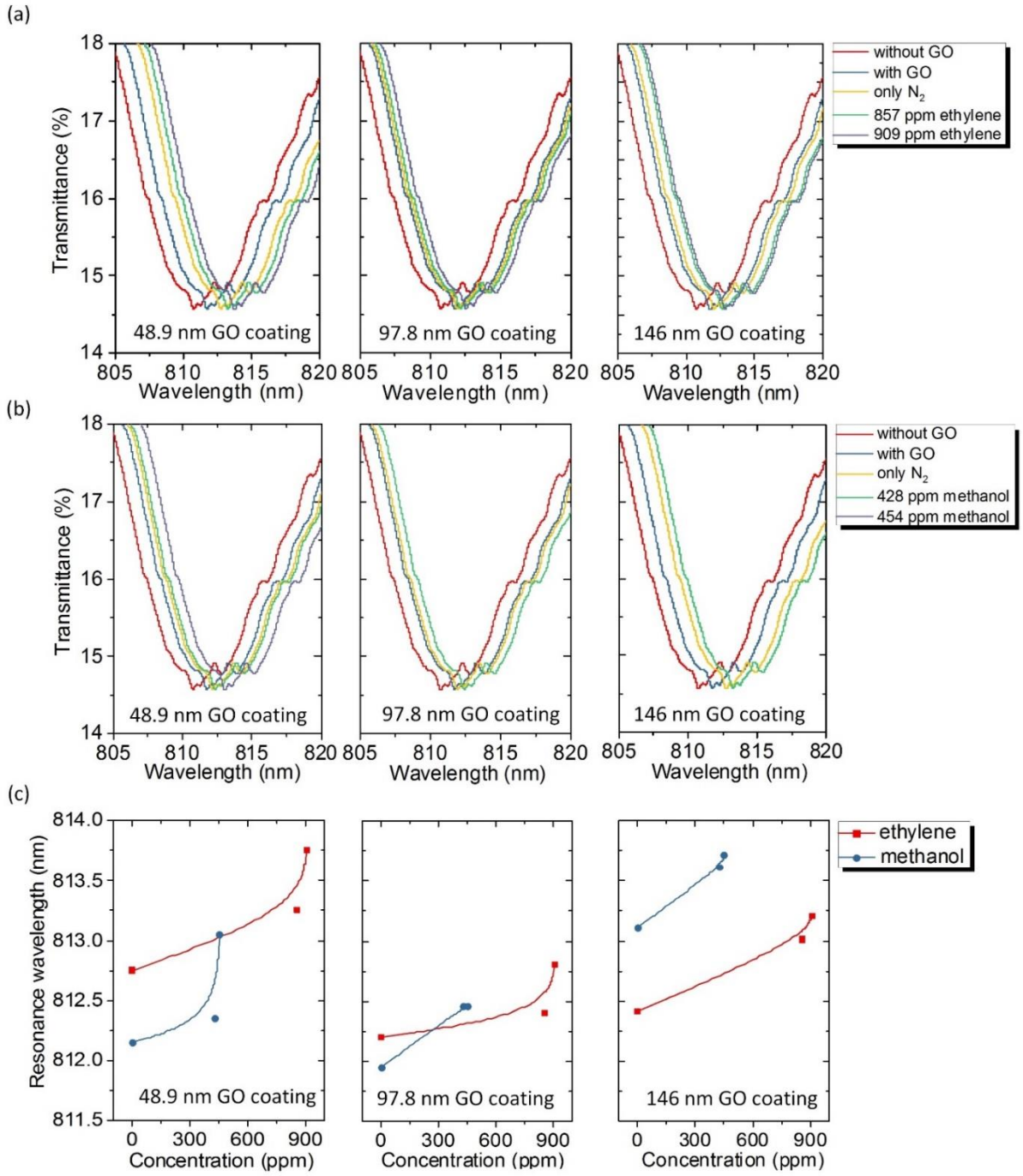


Fig. 3.9: *Transmittance spectra of fiber tip gas sensors with three different thicknesses of GO when exposed to gaseous (a) ethylene and (b) methanol. (c) Resonance wavelength shifts of three fiber tip gas sensors with different thicknesses of GO as a function of concentration of gaseous ethylene and methanol.*

master molds, or varying compositions of gas absorbing materials. In another work, an optical fiber long period grating gas sensor exhibited a sensitivity of 0.2 pm/ppm for methanol gas

[39] which is almost 15 fold less than that of our sensor. Finally, to our knowledge, no ethylene detection sensor has been reported so far based on the principle of optical resonance wavelength shift.

We further recorded absorption and desorption kinetics of the sensor with three different thicknesses of GO (48.9 nm, 97.8 nm and 146 nm) as shown in Fig. 3.10. During each experiment, the sensor was first exposed to 857 ppm and then 909 ppm of gaseous ethylene and after that thermally treated on a hot plate at $70^0$C for 2 hrs in order to allow the quick desorption of gas molecules from the GO layer. Thus thermal treatment of the fiber tip resulted in a return of the resonance wavelength to the baseline value of 812 nm as was also confirmed through experiment and shown in Fig. 3.10a. For comparison, we also performed the dynamic measurements without any GO coating (Fig. 3.10d). It is apparent from Fig. 3.10 that the sensor exhibits a much faster response and a much higher sensitivity when coated with GO nanosheets.

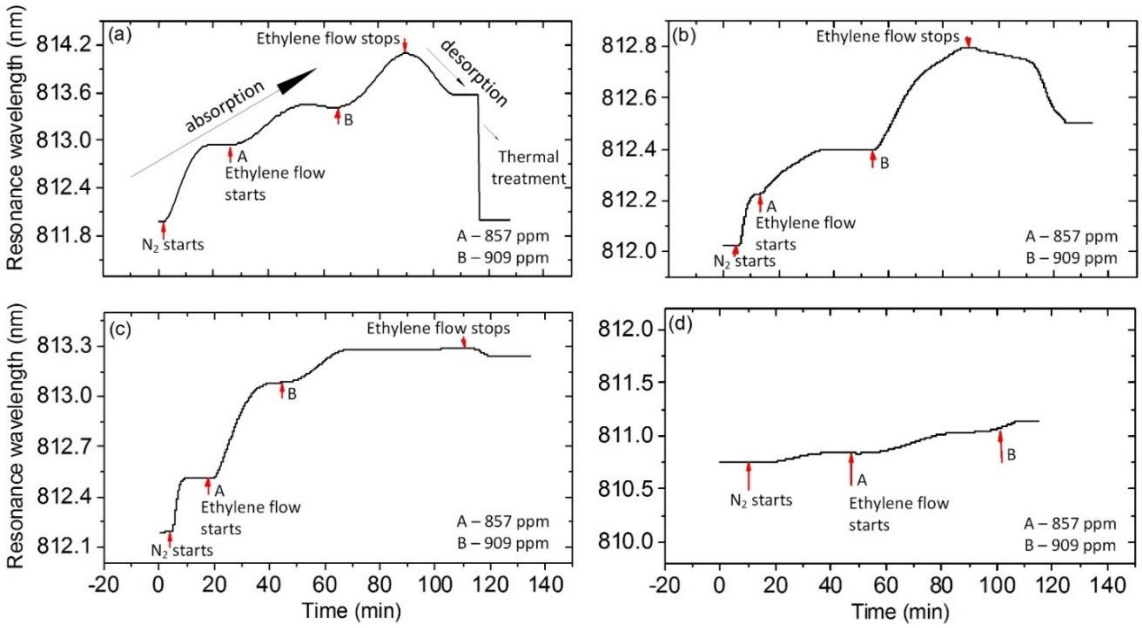


Fig. 3.10: *A 2 hr exposure test for gaseous ethylene with (a) 48.9 nm, (b) 97.8 nm, (c) 146 nm GO coating and (d) without any GO coating. A and B denote the instants when 857 ppm and 909 ppm of gaseous ethylene were introduced in the chamber.*

To test the reproducibility of the sensor, we made three identical sensors, each of them coated with 48.9 nm GO nanosheets. The three sensors exhibited resonance at the same wavelength of approximately 810.75 nm (Fig. 3.11a). Moreover, under the same condition these sensors were used to detect ethylene gas at a given concentration (857 ppm). Fig. 3.11b shows the resonance shifts obtained with each sensor when exposed to 857 ppm gaseous ethylene. Each sensor was run for three repeated measurements. A standard deviation of 0.1 nm in optical resonance was observed for all the three sensors which indicates that the sensor offered good reproducibility.

### 3.8 Comparison to Existing Fiber-Tip Gas Sensors

We presented a simple and economical method to fabricate high-resolution and repeatable nanopatterns at the optical fiber tip using UV assisted NIL, as well as a fiber-tip based GMR device integrated with GO nanosheets, to act as gas sensors. The integration of periodic nanostructures at the fiber tip facilitates light trapping at nanoscale providing a compact optical system which can be used for various sensing purposes. Previously, gas sensors have been reported at the fiber tip such as a Fabry-Perot (FP) sensor [40]. Generally, the FP sensors incorporate a single or a matrix of gas sensitive polymer layers, wherein vapor absorption at the polymer layer causes spectral shifts in the FP resonance [12], [41]. These FP sensors offer higher sensitivity, but the selective detection of different gas species entails coating the FP chamber atop the fiber tip with a gas-selective composition of polymer materials, adding to fabrication complexity, that our design avoids. Another type of fiber-tip based FP sensor consists of 3D cascade cavities, which usually increases the complications of sensor fabrication [40], [42]. An extrinsic FP cavity made of the cleaved facets of two fibers has also been reported, but the performance of such FP device relies on precise alignment of the fibers [43] and [44]. In contrast, our sensor deploys the GMR and GO layers over a planar

nanohole array, obtained by the inexpensive nanomolding and UV-NIL. Finally, ours is a "label-free" sensor, not needing a gas-selective adsorption material. We simply use varying thicknesses of the GO layer at identical fiber-tips forming an array of sensors. As shown in our prior work [45], pattern classification algorithms can be employed to analyze the measurements from the array of sensors to determine the gas species and their concentrations within a complex mixture of gases. This label-free approach keeps the fabrication process of our sensor simple, economical, yet effective.

## 3.9 Conclusion

In summary, through the current work we simplified the fabrication steps of transferring nanopatterns to an optical fiber tip, eliminating one out of four parameters (the tilt angle), as one of the design parameters. This cuts down the complexity of design space from $O(n^4)$ to $O(n^3)$, where $n$ represents the number of choices per parameter. This can lead to great savings in the time needed to select the parameters of the fabrication process. Also the non-angled normal patterning permits higher control and uniformity. We also demonstrated a $TiO_2$ coated GMR structure which is sensitive to changes in surrounding refractive index and offers shifts in its resonant wavelength. We provided a comprehensive physics-based explanation of the working principle, and also performed experiments to characterize our GMR device. The mathematical formulation showed clear dependence on the average refractive index of the grated waveguide, which changes as the grating interacts with analytes. Further the mathematical formulation also showed the dependence of the resonant wavelength on the grating period and waveguide thickness, both of which can be controlled to design an array of nanopatterns with varying sensitivities. Their combined response can be analyzed algorithmically (e.g., through pattern recognition) to achieve selectivity to gas species. To enhance sensitivity and response time, the GMR structure was further coated with a thin layer

of GO nanosheets to demonstrate the workability of the device as a gas sensor. GO's abundant functional groups contributed to the enhanced capture of gas species resulting in increased resonance wavelength shifts. A 2.6-fold increase in sensitivity and 75% reduction in response time to gaseous ethylene as compared to the case of no GO coating were observed. Moreover, the experiments were conducted to exhibit good stability and reproducibility of the sensor. This simplified and rapid nanostructuring at a fiber tip has the potential to be used in remote sensing applications, through the insertion of the nanopatterned fiber tips into aqueous and gaseous analytes which are otherwise inaccessible. Currently, efforts are being made to inscribe gratings around the fiber cladding in order to form brag reflectors.

## 3.10 References

[1] W. L. Barnes, A. Dereux, and T. W. Ebbesen, "Surface plasmon sub-wavelength optics", Nature, vol. 424, pp. 824-830, 2003.

[2] D. A. Genov, A. K. Sarychev, V. M. Shalaev, and A. Wei, "Resonant field enhancements from metal nanoparticle arrays", Nano Lett., vol. 4, pp. 153-158, 2004.

[3] N. F. Chiu, T. Y. Huang, and H. C. Lai, "Graphene oxide based surface plasmon resonance biosensors", Intech, ch. 8, 2013.

[4] J. I. L. Chen, Y. Chen, and D. S. Ginger, "Plasmonic Nanoparticle Dimers for Optical Sensing of DNA in Complex Media", J. AM. Comm. Soc., vol. 132, pp. 9600-9601, 2010.

[5] K. Aslam, J. R. Lakowicz, and C. D. Geddes, "Nanogold Plasmon Resonance-Based Glucose Sensing. 2. Wavelength-Ratiometric Resonance Light Scattering", Anal. Chem., vol. 77, pp. 2007-2014, 2005.

[6] M. A. Ali, S. Tabassum, Q. Wang, Y. Wang, R. Kumar and L. Dong, "Plasmonic-electrochemical dual modality microfluidic sensor for cancer biomarker detection", 2017 IEEE 30$^{th}$ International Conference on Micro Electro Mechanical Systems (MEMS), Las Vegas, pp. 390-393, 2017.

[7] S. K. Mishra, and B. D. Gupta, "Surface plasmon resonance-based fiber optic chlorine gas sensor utilizing indium-oxide-doped tin oxide film", Jounal of Lightwave Tech., vol. 33, pp. 2770-2776, 2015.

[8] H. Xu, P. Wu, . Zhu, A. Elbaz, and Z. Z. Gu, "Photonic crystal for gas sensing", Journal of Mat. Chem. C, vol. 1, pp. 6087, 2013.

[9] S. Tabassum, Q. Wang, W. Wang, S. Oren, M. A. Ali, R. Kumar, and L. Dong, “Plasmonic crystal gas sensor incorporating graphene oxide for detection of volatile organic compounds”, 2016 IEEE International Conference on Micro Electro Mechanical Systems (MEMS), Shanghai, pp. 913-916, 2016.

[10] Y. Lin, Y. Zou, and R. G. Lindquist, “A reflection-based localized surface plasmon resonance fiber-optic probe for biochemical sensing”, Biomed. Opt. Express, vol. 2, pp. 478-484, 2011.

[11] M. Sanders, Y. Lin, J. Wei, T. Bono, and R. G. Lindquist, “An enhanced LSPR fiber-optic nanoprobe for ultrasensitive detection of protein biomarkers”, Biosens. Bioelectron, vol. 61, pp. 95-101, 2014.

[12] J. Liu, Y. Sun, and X. Fan, “Highly versatile fiber-based optical Fabry-Perot gas sensor”, Opt. Express, vol. 17, pp. 2731-2738, 2009.

[13] Z. Li, Z. Wang, C. Wang, and W. Ren, “Optical fiber tip-based quartz-enhanced photoacoustic sensor for trace gas detection”, Appl. Phys. B, vol. 122, num. 5, pp. 1, 2016.

[14] J. T. Robinson, F. K. Perkins, E. S. Snow, Z. Wei, and P. E. Sheehan, “Reduced graphene oxide molecular sensors”, Nano Lett., vol. 8, pp. 3137-3140, 2008.

[15] X. Li, W. Cai, J. An, S. Kim, J. Nah, D. Yang, R. Piner, A. Velamakanni, I. Jung, E. Tutuc, S. K. Banerjee, L. Colombo, and R. S. Ruoff, “Large-area synthesis of high-quality and uniform graphene films on copper foils”, Sci. vol. 306, 2004.

[16] S. S. Nanda, D. K. Yi, and K. Kim, “Study of antibacterial mechanism of graphene oxide using Raman spectroscopy”, Sci. Reports, vol. 6, pp. 28443, 2016.

[17] G. Lu, L. E. Ocola, and J. Chen, “Gas detection using low-temperature reduced graphene oxide sheets”, Appl. Phys. Lett., vol. 94, pp. 083111, 2009.

[18] P. A. Pandey, N. R. Wilson, and J. A. Covington, “Pd-doped reduced graphene oxide sensing films for $H_2$ detection”, Sens. Actuators, vol. 183, pp. 478-487, 2013.

[19] M. A. A. Rosli, P. T. Arasu, A. S. M. Noor, H. N. Lim, and N. M. Huang, “Reduced graphene oxide nano-composites layer on fiber optic tip sensor reflectance response for sensing of aqueous ethanol”, Journal of the European optical society, vol. 12, 2016.

[20] M. Consales, A. Ricciardi, A. Crescitelli, E. Esposito, A. Cutolo, and A. Cusano, “Lab-on-fiber technology: Toward multifunctional optical nanoprobes”, ACS Nano, vol. 6, pp. 3163-3170, 2012.

[21] W. Jung, B. Park, J. Provine, R. T. Howe, and O. Solgaard, “Highly sensitive mobolithic silicon photonic crystal fiber tip sensor for simultaneous measurement of refractive index and temperature”, J. Lightwave Technol., vol. 29, pp. 1367-1374, 2011.

[22] P. S. Kelkar, and J. Beauvais, “Nano patterning on optical fiber and laser diode facet with dry resist”, J. Vac. Sci. Technol. A vol. 22, pp. 743-746, 2004.

[23] Micco, A. Ricciardi, M. Pisco, V. La Ferrara and A. Cusano, “Optical fiber tip templating using direct focused ion beam milling”, Nature, 2015.

[24] S. Kang, H. E. Joe, J. Kim, Y. Jeong, B. K. Min, and K. Oh, “Subwavelength plasmonic lens patterned on a composite optical fiber facet for quasi-one-dimensional bessel beam generation”, Appl. Phys. Lett., vol. 98, pp. 241103, 2011.

[25] D. J. Lipomi, R.V. Martinez, M.A. Kats, S.H. Kang, P. Kim, J. Aizenberg, F. Capasso, and G.M. Whitesides, “Patterning the tips of optical fibers with metallic nanostructures using nanoskiving”, Nano Lett., vol. 11, pp. 632-636, 2011.

[26] S. Y. Chou, P. R. Krauss, and P. J. Renstrom, “Imprint of sub-25 nm vias and trenches in polymer”, Appl. Phys. Lett., vol. 67, pp. 3114-3116, 1995.

[27] S. Scheerlinck, P. Bienstman, E. Schacht, and D.V. Thourhout, “Metal grating patterning on fiber facets by UV-based nano imprint and transfer lithography using optical alignment”, IEEE Journal of Lightwave Technology, vol. 27, pp. 10, 2009.

[28] S. Scheerlinck, D.V. Thourhout, and R. Baets, “Nano imprint lithography for photonic structure patterning”, Proceedings Symposium IEEE/LEOS Benelux Chapter, 2005.

[29] J. Viheriala, T. Niemi, J. Kontio, T. Rytkonen, and M. Pessa, “Fabrication of surface reliefs on facets of singlemode optical fibres using nanoimprint lithography”, Electron. Lett., vol. 43, pp. 150–152, 2007.

[30] G. Shambat, S. R. Kothapalli, A. Khurana, J. Provine, T. Sarmiento, K. Cheng, Z. Cheng, J. Harris, H. D. –Link, S. S. Gambhir, and J. Vučković, “A photonic crystal cavity-optical fiber tip nanoparticle sensor for biomedical applications”, Appl. Phys. Lett., vol. 100, pp. 213702, 2012.

[31] S. Tabassum, Y. Wang, J. Qu, Q. Wang, S. Oren, R. J. Weber, M. Lu, R. Kumar and L. Dong, “Patterning of nanophotonic structures at optical fiber tip for refractive index sensing”, 2016 IEEE Sensors, Orlando, Fl, pp. 1-3, 2016.

[32] S. Tabassum, R. Kumar, and L. Dong, “Nanopatterned optical fiber tip for guided mode resonance and application to gas sensing”, IEEE Sens. J., vol. 17, pp. 7262-7272, 2017.

[33] M. S. Amin, “Design, fabrication and characterization of guided-mode resonance transmission filters”, (Doctoral dissertation) ProQuest Dissertations And Theses, 2014.

[34] T. K. Gaylord, and M. G. Moharam, “Analysis and applications of optical diffraction by gratings”, Proc. IEEE, vol. 73, pp. 894-937, 1985.

[35] B. E. A. Saleh, and M. C. Teich, “Fundamentals of photonics”, Wiley series in pure and applied optics; 2nd ed., Chap. 9, pp. 330-335.

[36] D. Marcuse, “Theory of dielectric optical waveguides”, Academic, New York, 1991; 2nd ed., Chap. 1, pp. 7.

[37] R. Ramachandran, M. Saranya, P. Kollu, B. P. C. Raghupathy, S. K. Jeong, and A. N. Grace, “Solvothermal synthesis of Zinc sulfide decorated graphene (ZnS/G) nanocomposites for novel supercapacitor electrodes”, Elect. Acta, vol. 178, pp. 647-657, 2015.

[38] S. Boonruang, “Two-dimensional guided mode resonant structures for spectral filtering applications”, University of Central Florida, 2007.

[39] J. Hromadka, B. Tokay, S. James, R. P. Tatam, and S. Korposh, “Optical fibre long period grating gas sensor modified with metal organic framework thin films”, Sens. Actuators B: Chem., vol. 221, pp. 891-899, 2015.

[40] M. Quan, J. Tian, and Y. Yao, “Ultra-high sensitivity Fabry-Perot interferometer gas refractive index fiber sensor based on photonic crystal fiber and Vernier effect”, Opt. Lett., vol. 40, pp. 4891-4894, 2015.

[41] Z. Opilski, T. Pustelny, E. Maciak, M. Bednorz, A. Stolarczyk, and M. Jadamiec, “Investigations of optical interferometric structures applied in toxic gas sensors”, Bull. Pol. Ac.: Tech., vol. 53, pp. 151-156, 2005.

[42] P. Jia, G. Fang, T. Liang, Y. Hong, Q. Tan, X. Chen, W. Liu, C. Xue, J. Liu, W. Zhang, and J. Xiong, “Temperature-compensated fiber-optic Fabry-Perot interferometric gas refractive-index sensor based on hollow silica tube for high-temperature application”, Sens. Actuators B: Chem., vol. 244, pp. 226-232, 2017.

[43] G. Z. Xiao, A. Adnet, Z. Zhang, F. G. Sun, and C. P. Grover, “Monitoring changes in the refractive index of gases by means of a fiber optic Fabry-Perot interferometer sensor”, Sens. Actuators A, vol. 118, pp. 177-182, 2005.

[44] R. S. –Gelais, G. Mackey, J. Saunders, J. Zhou, A. L. –Hotte, A. Poulin, J. A. Barnes, H. –P. Loock, R. S. Brown, and Y. –A. Peter, “Gas sensing using polymer-functionalized deformable Fabry-Perot interferometers”, Sens. Actuators B: Chem., vol. 182, pp. 45-52, 2013.

[45] S. Tabassum, R. Kumar, and L. Dong, “Plasmonic crystal based gas sensor towards an optical nose design”, IEEE Sensors Journal, vol. PP, no. 99, pp. 1-1, doi: 10.1109/JSEN.2017.2740176, 2017.

# CHAPTER 4. HEATER INTEGRATED NANOPATTERNED OPTICAL FIBER-TIP TO REALIZE A REUSABLE GAS SENSOR

A paper presented in SPIE Optics and Photonics Conference

Shawana Tabassum, Liang Dong, and Ratnesh Kumar

## 4.1 Abstract

We present the first heater integrated nanostructured optical fiber of 200 µm diameter to realize a high-sensitivity and reusable fiber-optic gas sensor. In our guided mode resonance-enabled fiber-optic gas sensor, resonance shifts upon the adsorption of the analytes on the graphene oxide (GO) coated sensor surface. For repeated use of this sensor, a regeneration of the sensor surface is required by a complete desorption of the analyte molecules from the GO layer. In our presented design, this has been achieved by the integration of a controllable heater at the fiber tip. The heater was fabricated by embedding a helical thin nichrome wire wrapped along a cylindrical rod into a precursor solution of polydimethylsiloxane, and subsequently removing the rod from the cured elastomer and leaving the helical wire inside the elastomer. Thus, a cylindrical cavity of length 16 mm and diameter 4 mm surrounded by the helical wire was formed that then contains the fiber-tip sensor. For the ethylene gas analyte, we demonstrated the reversibility of the heater integrated fiber-tip sensor, with a tunable recovery time. Owing to the rapid heat transfer from the helical wire to the encased fiber-tip sensor, the heater integrated fiber-tip sensor responds to heating in only about 2.5 min. The high resonance sensitivity of the nanopatterned fiber-tip to its surrounding refractive index, in conjunction with excellent repeatability through integrated heating for surface regeneration, enables a practical fiber-tip based remote sensing.

## 4.2 Introduction

The lab-on-fiber (LOF) technology is continuously driving the development of novel multifunctional nanoprobes incorporating optical resonant structures and functional coating materials either at the tip, along the cylindrical surface, or inside the fiber core with unprecedented results in terms of sensor miniaturization and performance [1]. Moreover, different nanoparticles (e.g. gold) and coating materials (e.g. graphene and its derivatives) are employed to enable sensor interaction with analytes [2-4]. Ample research has been conducted toward the exploration of novel fabrication strategies to realize a variety of nanostructures as a route to achieve light-matter interactions, extraordinary field manipulation and field steering capabilities at nanoscale [5-12]. Such nanostructuring leads to the realization of novel optrodes for applications including optical tweezers [13-15], in-vivo single molecule imaging [16], [17], cantilevers [18] and sensing capable of detecting and discriminating among large classes of molecules [1], [19]. There has also been considerable research effort in developing LOF gas sensors[20-22]. Recently, we have developed a guided mode resonance (GMR) based sensing platform nanopatterned at the end facet of an optical fiber [23], [24]. We further coated the GMR device with a thin layer of graphene oxide (GO) nanosheets and utilized the resulting optrode to monitor different concentrations of gases (i.e. ethylene and methanol). The working principle of these LOF sensing probes depends on the interaction of functional coating attached to the sensor surface with its target analyte.

A practical limitation of graphene oxide and other polymer-based gas absorbing coating is that a complete desorption of gas molecules from the coating cannot be achieved unless it is heated for a time period. While recent research is directed towards improving the sensing performance of an optrode, little attention has been paid on integrating a miniaturized heater with a sensor probe. One approach to addressing the said limitation is to use thin-film resistive

heaters with uniform or tapered thicknesses, formed on the cylindrical surface of fiber [25]. However, the low resistivity of such thin films cannot provide sufficient heat by Joule heating. In addition, depositing an extra film on the sensor surface often interferes with the performance of the sensor itself. Ou et al. presented an optical fiber-tip coated with nano platelet $WO_3$ film to detect $H_2$ gas in which they used a localized sample heater to heat the sensor probe [26]. Such external heaters are inconvenient to use unless integrated with the sensor.

In this work, we present, a first of a kind, a simple and cost-effective miniaturized heater, integrated with our previously developed GMR-based nano-sensor at the fiber tip, that overcomes the aforementioned issues. We demonstrate that the sensor probe heated at different temperatures exhibits different recovery rates. Thus, it is possible to tune the sensor recovery time which is an important figure of merit for gas sensing applications. Overall our results demonstrate that by combining miniaturized heater with the fiber-optic sensor it is possible to develop a flexible and reusable optrode, particularly useful for gas sensing applications. While it is demonstrated here for gas sensing using fiber-tip based nano-probe, the proposed mechanism of integrated heating system can be easily incorporated into other fiber-optic platforms. This work resulted in the publication [27].

### 4.3 Heater Integrated Sensor Fabrication and Characterization

In our recent work, we fabricated nanostructures having a square lattice (of pitch 500 nm, nanohole diameter of 250 nm and depth of 210 nm), at the end facet of an optical fiber tip using ultraviolet assisted nano-imprint lithography (UV-NIL) [23], [24]. Next, a guided mode resonance (GMR) device was realized by depositing a 300-nm thick $TiO_2$ layer at the nanopatterned fiber tip. Afterwards, the nanostructures were coated with graphene oxide (GO) nanosheets to allow gas adsorption, leading to resonance shift of the GMR mode, and sensing was done by measuring those resonance shifts. A complete desorption of the gas molecules

from the sensor surface is needed to realize a reusable sensor, which we attain in this work through the integration of a controllable heater with the fiber-tip sensor.

### 4.3.1 Fabrication

Fabrication of the heater consists of five major steps, namely, i) embedding a helical thin nichrome wire wrapped along a cylindrical rod into a precursor solution of elastomer (see Fig. 4.1a), ii) removing the rod from the cured elastomer and leaving the helical wire inside the elastomer, thus realizing a cylindrical channel (see Fig. 4.1b), iii) inserting a slotted ferrule into the cylindrical channel, (iv) embedding the sensor fiber (carrying nanopatterns at the tip) and a plain fiber into two separate FC/PC fiber connectors, and (v) coupling the two fibers by inserting the two FC/PC connectors into the slotted ferrule from the opposite ends. (see Fig. 4.1c). The details of fabrication process are given below.

First, a precursor solution of polydimethylsiloxane (PDMS) was prepared by mixing Sylgard 184 (Dow Corning, Auburn, MI) and curing agent at the weight ratio of 10:1, which was subsequently degassed in a vacuum desiccator for 20 min. Next, a nichrome resistance heating wire was wrapped around a 4-mm diameter metal rod. In order to achieve uniform spacing between the neighboring turns of the coiled wire, the wire was initially wound around a screw to follow the threads. The wire was then taken off the screw, serving as a mold through which the 4-mm diameter metal rod was inserted. Subsequently, the PDMS solution was poured into a rectangular metal block with 4.2 mm circular holes at two sides (Fig. 4.2). The rod with the helical-wrapped wire was then inserted into the metal block through the side-holes. The PDMS solution was then thermally cured on a hotplate at 65 °C for 2 hr, and the cured PDMS embedded into the metal block was placed in acetone for 2 hr. The swelling of the PDMS induced by acetone enabled easy pulling of the metal rod. As a result, a cylindrical channel of length 16 mm and diameter 4 mm was formed inside the cured PDMS with the

helical wire surrounding this channel. Finally, a slotted ferrule of 2.5 mm diameter was inserted into the cylindrical channel, and the sensor fiber and the plain fiber were embedded into two FC/PC fiber connectors. Next the two fibers were coupled by inserting the two FC/PC connectors, embedded with the respective fibers, into the slotted ferrule from the opposite ends (Fig. 4.2). In addition, two holes were punched on the cured elastomer through the channel. One hole enabled the gaseous/aqueous analyte to enter the cylindrical channel from the surrounding medium while the other hole served as the analyte exit port (Fig. 4.1c). Additionally, the slotted ferrule allowed the access for the analyte entering from the entry hole to reach the nanopatterned fiber tip, and further access to it to reach the exit hole and escape. Such a gas flow path is illustrated in the zoomed-in cross section of the final device in Fig. 4.1e. The purpose of using PDMS is two-fold. First, embedding the heating coil into PDMS is simple and cost-effective. Second, PDMS is a good thermal insulator with a thermal conductivity of only 0.15 $Wm^{-1}K^{-1}$ which does not allow heat dissipation from the heater to outside medium and hence efficient heat transfer takes place from the heating coil to the sensor fiber [28].

### 4.3.2 Heater Specifications

The nichrome heating coil had a cross-sectional diameter of 230 μm and a resistivity of $1.1 \times 10^{-4}$ Ωcm. The geometry of the helical coil was determined using [29], where in (4.1) given the diameter ( $D$ =4.23 mm) of the helix and its axial pitch helix ( $S$ = 1.6 mm), the length of one helical turn ( $L_0$ =13.38 mm) is obtained.

$$L_0 = \sqrt{(\pi D)^2 + S^2} \tag{4.1}$$

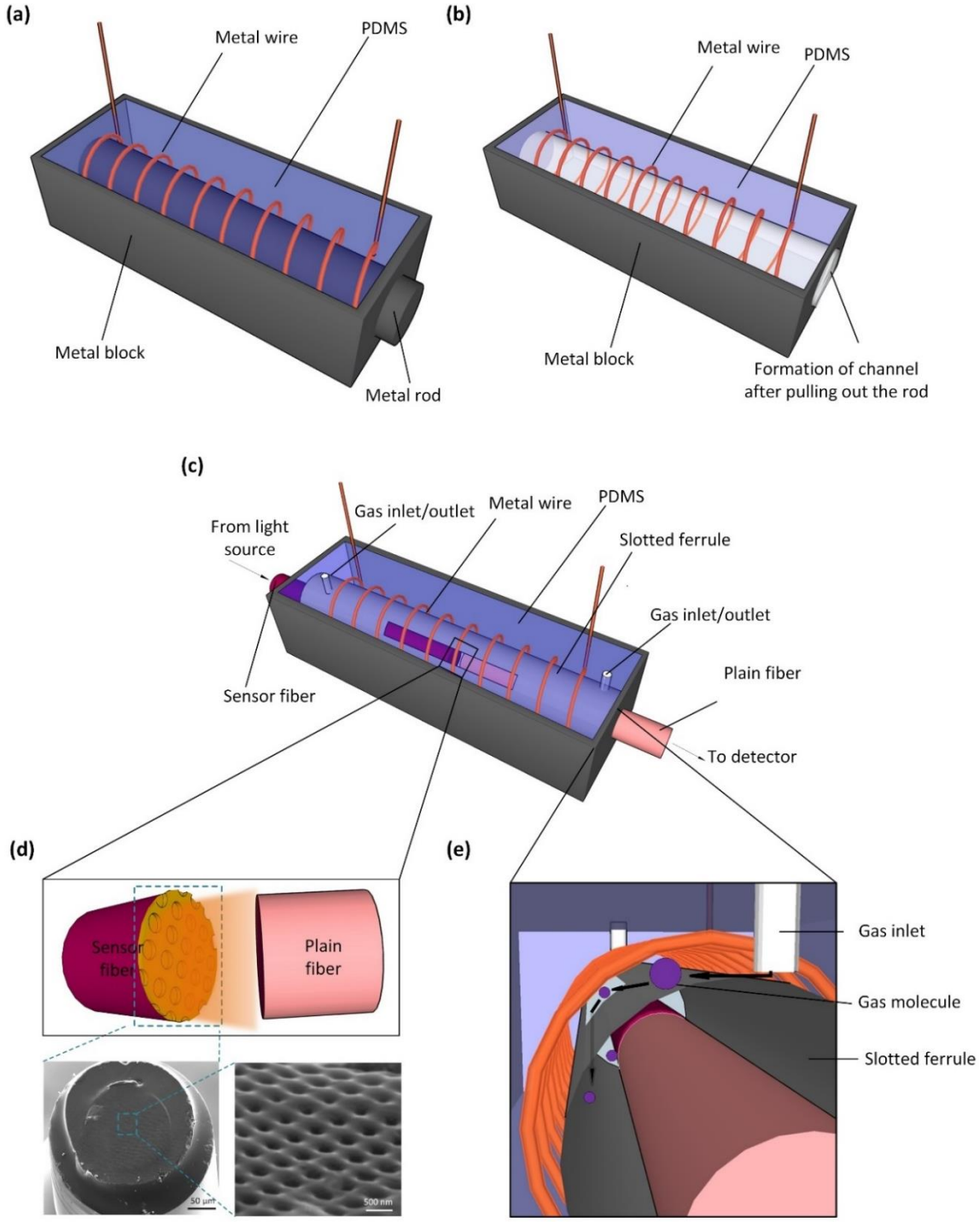


Fig. 4.1: *(a-c) Step-wise representation of the fabrication process for the heater-integrated nanopatterned fiber tip sensor. (a) Metal wire wrapped along a cylindrical rod and embedded into PDMS solution. (b) PDMS is thermally cured and the cylindrical rod is removed, thus realizing a cylindrical channel surrounded by the helical wire. (c) Coupling the sensor fiber with the plain fiber through slotted ferrule. (d) Close up of the coupled fibers with the SEM images illustrating the $TiO_2$-GO coated nanoholes at the tip of the sensor fiber. (e) Details of the gas flow path from the inlet to the tip of the sensor fiber.*

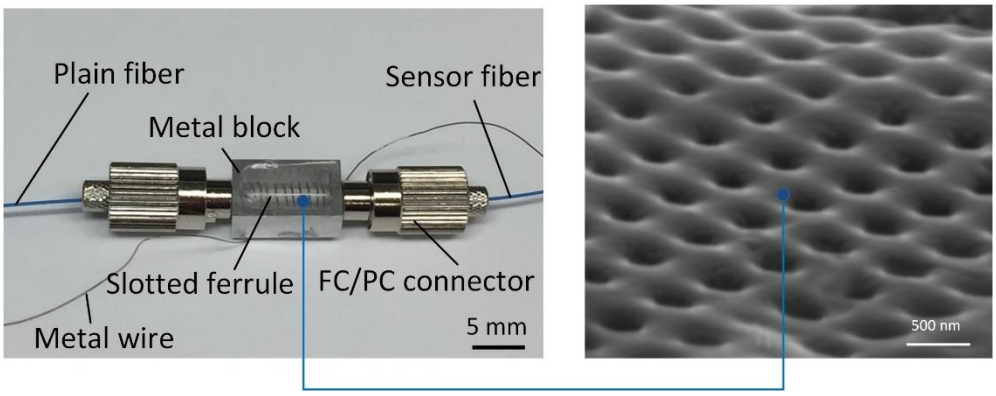


Fig. 4.2: *Fabricated heater-integrated fiber-tip sensor (left) and SEM image of optical fiber tip patterned with nanoholes (right).*

Then given the number of turns ( $N$ =10), the total length of the wire when full stretched was calculated using (4.2) and it was measured $L_n$ = 133.8 mm:

$$L_n = NL_0 \qquad (2)$$

Finally, the unstretched end-to-end length of the helix was computed using (4.3) and it was measured $L$ = 16 mm:

$$L = NS \qquad (3)$$

To access the helical coil embedded into PDMS inside the metal block (Fig. 4.2), the two ends of the coil outside the metal block were kept straight, where electrical voltage can be applied across the coil for its heating. The total length of the coil in straight mode ( $L_n$ + the two straight ends) was 30 cm, and the total resistance of the coil was 10 Ω.

When a dc voltage was applied across the coil, the current passing through the coil caused Joule heating, with a heating rate that depended on the electrical current and resistance of the coil. Each time a dc voltage was applied across the heating coil causing a dc current to flow through the coil, the temperature profile generated by the resistive heating and the sensor recovery time (time for the desorption of the gases from the sensor surface) were monitored. The results are listed in Table 4.1. Real-time monitoring of the sensor recovery time is

explained in detail under "Results and Discussion". In Table 4.1 the recovery time of the sensor are defined classically as the time corresponding to the decrease of the sensor signal by 90% of its saturation value (and after the test gas is cut off). Analogously, the response time is defined as the time taken by the sensor signal to reach 90% of its saturation value upon exposure to test gas mixed with nitrogen.

Table 4.1. *Sensor recovery achieved for four different heating temperatures.*

| **Voltage (V)** | **Current (mA)** | **Final Temperature ($^0$C)** | **Recovery Time (min)** |
|---|---|---|---|
| 3.03 | 300 | 60 | 15 |
| 3.38 | 340 | 70 | 15 |
| 4.10 | 410 | 90 | 2.5 |
| 4.50 | 450 | 100 | 2.5 |

## 4.4 Materials and Methods

### 4.4.1 Chemicals and Materials

GO nanosheets were purchased in the flakes form from ACS Material, Pasadena, CA, USA, with the elemental compositions being 40.78% and 51.26% for O (wt%) and C (wt%), respectively. Sylgard 184 Silicone elastomer kit was purchased from Dow Corning Cop., MI, USA which was used to prepare PDMS solution. SU8-2000 was purchased from MicroChem Corp., MA, USA. Deionized (DI) water with resistivity of 18.2 MΩ was obtained using Millipore's purification system from Billerica, MA, USA and utilized to prepare GO dispersion solutions. The nichrome wire (31GA-NI60) was purchased from MOR Electric Heating, Comstock Park, MI, USA.

### 4.4.2 Optical Measurements and Gas Sensing Setup

For optical measurements, a white light source (150-watt quartz halogen lamp; Luxtec Fiber Optics, Plainsboro, NJ) was used to illuminate the nanohole-structure fabricated at the

tip of a multimode fiber (FT200EMT, Thorlabs, Newton, NJ). The light scattered from the end facet of the sensor fiber was collected by a plain multimode fiber and measured by a UV/Vis spectrometer (USB-4000, Ocean Optics). Light was coupled from the sensor fiber to the plain fiber by means of a slotted ferrule (ADAF1, Thorlabs, Newton, NJ) and two FC/PC connectors (30230C, Thorlabs, Newton, NJ).

An aluminum chamber was used to enclose the heater integrated sensor fiber and do the gas sensing measurements. 1000ppm of ethylene gas flowed from a cylinder (116L-62N-1000, Cal Gas Direct Incorporated, Huntington Beach, CA) into the gas chamber which was further diluted by carrier nitrogen gas. The gas flow rate was controlled by a mass flow controller (GFC17, Aalborg, Orangeburg, NY). The flow rate of nitrogen gas was fixed at 10 ml/min and the flow rate of ethylene gas was varied by means of the mass flow controller to dilute the ethylene gas to different concentrations.

### 4.5 Sensor Recovery Results and Discussion

The detailed description of the sensor and its application to gas sensing is provided in our previous work [23], [24]. The present work is focused on exploring the sensor surface regeneration through its integrated heating.

The heater-integrated fiber tip-based GMR sensor was placed inside an aluminum gas chamber having the facility for both injection as well as evacuation of testing and carrier gases. White light from the halogen light source was directed into the sensor fiber and was collected by the plain multimode fiber at the detection end into a spectrometer (see Fig. 4.1c). At the start, the baseline resonance was measured to be 586 nm in air. Next, pre- diluted ethylene gas flowed from a cylinder into the gas chamber where it was further diluted by the carrier nitrogen gas. Figure 4.3 tracks the dynamic response of the sensor when exposed to ethylene gas with a tunable sensor recovery achieved at different heating temperatures. The sensor response to

gaseous ethylene mixed with nitrogen was monitored at room temperature. The resonance dip gradually red-shifted to a maximum wavelength of 586.65 nm. Once the response saturated at the maximum wavelength, the gas flow was stopped. It was observed that even though the gas flow was stopped, the resonance dip did not blue-shift because of the gas molecules still remaining on the GO coating.

In order to completely release the gas molecules from the GO layer, the sensor at the fiber tip was heated. As a result, the gas molecules had sufficient energy to detach from the GO coating and diffuse into the surrounding. The heater was turned on by applying a voltage across the nichrome wire several minutes after the gas flow was stopped (Fig. 4.3). This was done to confirm that sensor recovery could not be achieved without heating. Current flow through the helical coil caused Joule heating and heat transferred convectively to the sensor fiber. As the gas started to desorb, the resonance dip progressively blue shifted and finally settled at the baseline value. The blue shift is attributed to desorption of gas molecules from the GO layer resulting from radial heat transfer from the helical coil to the fiber-tip. For different applied voltages of 3.03, 3.38, 4.1 and 4.5 volts, the temperatures at the sensor fiber-tip were measured to be 60, 70, 90 and 100 degrees of Celsius respectively (see Table 4.1). The sensor recovery time also varied with varying temperatures that can provide an added flexibility in the sensor operation. As heat diffused into the fiber-tip, the resonance wavelength reached the baseline value in just two and half minutes for a temperature of $100^0$C (Fig. 4.3d).

The measurements were repeated three times in a cyclic manner when exposed to ethylene gas and for two different thicknesses of GO (48.9 nm and 97.8 nm) to check the reproducibility of the response and recovery characteristics of the sensor. The resonance wavelength was dynamically tracked during the absorption/de-absorption cycle (Fig. 4.4).

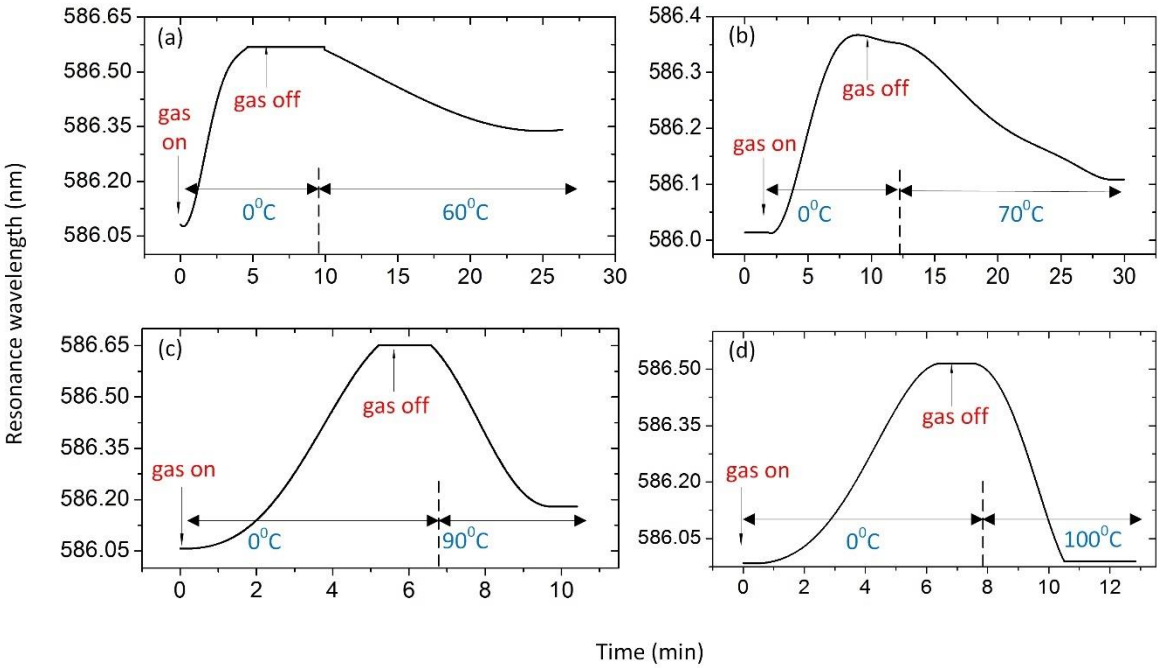


Fig. 4.3: *Dynamic tracking of resonance dip for the heater-integrated nanopatterned optical fiber tip-GMR sensor in ethylene gas mixed with nitrogen at four different temperatures (a) 60$^0$C, (b) 70$^0$C, (c) 90$^0$C, and (d) 100$^0$C. Gaseous ethylene 'on' and 'off' states are also illustrated.*

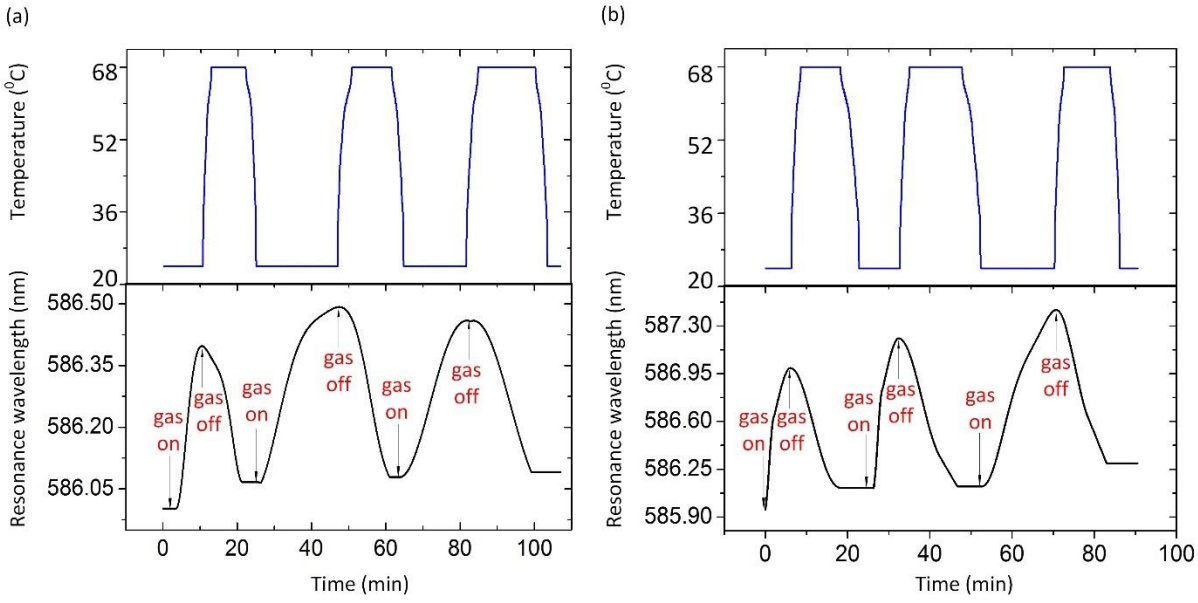


Fig. 4.4: *Reversibility test of the heater integrated fiber-tip GMR sensor when exposed to ethylene gas with (a) 48.9 nm, and (b) 97.8 nm GO coating. Top panels of (a-b) show the heater on-off cycles.*

## 4.6 Conclusion and Future Work

We reported the design, fabrication, characterization, and experimental validation of a first of a kind miniaturized and controllable heater integrated nanopatterned fiber tip-based gas sensor that is also reusable. The integrated system was characterized for different resistive heating temperatures and results were demonstrated for sensing and recovery cycles. The testing and regeneration cycle could be automated through additional electronics for maxima and minima detection. Further future work will be directed towards a more detailed device characterization, developing a gas selective coating and attaching that at the fiber tip and investigating the developmental processes in plants such as the control of fruit ripening or stress-responsive roles of plant hormones using the presented integrated heating and sensing system.

## 4.7 References

[1] Vaiano, P., Carotenuto, B., Pisco, M., Ricciardi, A., Quero, G., Consales, M., Crescitelli, A., Esposito, E. and Cusano, A., "Lab on fiber technology for biological sensing applications", Laser Photonics Rev. 10, 922-961 (2016).

[2] Aldewachi, H., Chalati, T., Woodroofe, M. N., Bricklebank, N., Sharrack, B. and Gardiner, P., "Gold nanoparticle-based colorimetric biosensors", Nnaoscale 10(18), 18-33 (2018).

[3] Suvarnaphaet, P. and Pechprasarn, S., "Graphene-based materials for biosensors: a review", Sensors 17, 2161 (2017).

[4] Tabassum, S., Dong, L. and Kumar, R., "Determination of dynamic variations in the optical properties of graphene oxide in response to gas exposure based on thin-film interference", Opt. Express 26(5), 6331-6344 (2018).

[5] Zhang, Z., Bargioni, A. W., Wu, S. W., Dhuey, S., Cabrini, S. and Schuck, P. J., "Manipulating nanoscale light fields with the asymmetric bowtie nano-colorsorter", Nano Lett. 9(12), 4505-4509 (2009).

[6] Yu, N., Genevet, P., Kats, M. A., Aieta, F., Tetienne, J. P., Capasso, F. and Gaburro, Z., "Light propagation with phase discontinuities: generalized laws of reflection and refraction", Science 334, 333-337 (2011).

[7] Lin, J., Genevet, P., Kats, M. A., Antonious, N. and Capasso, F., "Nanostructured holograms for broadband manipulation of vector beams", Nano Lett. 13(9), 4269-4274 (2013).

[8] Zhou, L., Ou, Q. D., Chen, J. D., Shen, S., Tang, J. X., Li, Y. Q. and Lee, S. T., "Light manipulation for organic optoelectronics using bio-inspired moth's eye nanostructures", Sci. Rep. 4, 4040 (2014).

[9] Tabassum, S., Wang, Q., Wang, W., Oren, S., Ali, M. A., Kumar, R. and Dong, L., "Plasmonic crystal gas sensor incorporating graphene oxide for detection of volatile organic compounds," Proc. IEEE Int. Conf. Micro Electro Mech. Syst. (MEMS), Shanghai, China, 913-916 (2016).

[10] Tabassum, S., Kumar, R. and Dong, L., "Plasmonic crystal-based gas sensor toward an optical nose design", IEEE Sens. J. 17(19), 6210-6223 (2017).

[11] Ali, M. A., Tabassum, S., Wang, Q., Wang, Y., Kumar, R. and Dong, L., "Plasmonic-electrochemical dual modality microfluidic sensor for cancer biomarker detection", Proc. IEEE Int. Conf. Micro Electro Mech. Syst. (MEMS), Las Vegas, NV, USA, 390-393 (2017).

[12] Ali, M. A., Tabassum, S., Wang, Q., Wang, Y., Kumar, R. and Dong, L., "Integrated dual-modality microfluidic sensor for biomarker detection using lithographic plasmonic crystal", Lab Chip 18(5), 803-817 (2018).

[13] Maimaiti, A., Truong, V. G., Sergides, M., Gusachenko, I. and Chormaic S. N., "Higher order microfibre modes for dielectric particle trapping and propulsion", Sci. Rep. 5, 9077 (2015).

[14] Kasztelanic, R., Filipkowski, A., Anuszkiewicz, A., Stafiej, P., Stepniewski, G., Pysz, D., Krzyzak, K., Stepien, R., Klimczak, M. and Buczynski R., "Integrating free-form nanostructured GRIN microlenses with single-mode fibers for optofluidic system", Sci. Rep. 8, 5072 (2018).

[15] Ribeiro, R. S. R., Dahal, P., Guerreiro, A., Jorge, P. A. S. and Viegas J., "Fabrication of Fresnel plates on optical fibres by FIB milling for optical trapping, manipulation and detection of single cells", Sci. Rep. 7, 4485 (2017).

[16] Hoppener, C. and Novotny, A. L., "Antenna-based optical imaging of single $Ca^{2+}$ transmembrane proteins in liquids", Nano Lett. 8, 642-646 (2008).

[17] Van Zanten, T. S., Lopez-Bosque, M. J. and Garcia-Parajo, M. F., "Imaging individual proteins and nanodomains on intact cell emmbranes with a probe-based optical antenna", Small 6, 270-275 (2010).

[18] Iannuzzi, D., Heeck, K., Salman, M., de Man, S., Rector, J. H., Schreuders, H., Berenschot, J. W., Gadgil, V. J., Sanders, R. G. P., Elwenspoek, M. C. and Deladi, S. "Fibre-top cantilevers: design, fabrication and applications", Meas. Sci. Technol. 18, 3247-3252 (2007).

[19] Consales, M., Ricciardi, A., Crescitelli, A., Esposito, E., Cutolo, A. and Cusano, A., "Lab-on-fiber technology: toward multifunctional optical nanoprobes", ACS Nano 6, 3163-3170 (2012).

[20] Liu, J., Sun, Y. and Fan, X., "Highly versatile fiber-based optical Fabry-Perot gas sensor", Opt. Express 17(4), 2731-2738 (2009).

[21] Hromadka, J., Tokay, B., James, S., Tatam, R. P. and Korposh, S., "Optical fibre long period grating gas sensor modified with metal organic framework thin films", Sens. Actuators B Chem. 221, 891-899 (2015).

[22] Hoo, Y. L., Jin, W., Shi, C., Ho, H. L., Wang, D. N. and Ruan, S. C., "Design and modeling of a photonic crystal fiber gas sensor", Appl. Opt. 42, 3509-3515 (2003).

[23] Tabassum, S., Wang, Y., Qu, J., Wang, Q., Oren, S., Weber, R. J., Lu, M., Kumar, R. and Dong, L., "Patterning of nanophotonic structures at optical fiber tip for refractive index sensing", Proc. IEEE Sensors, Orlando, FL, USA, 1-3 (2016).

[24] Tabassum, S., Kumar, R. and Dong, L., "Nanopatterned optical fiber tip for guided mode resonance and application to gas sensing", IEEE Sens. J. 17(22), 7262-7272 (2017).

[25] Rogers, J. A., Kuo, P., Ahuja, A., Eggleton, B. J. and Jackman, R. J., "Characteristics of heat flow in optical fiber devices that use integrated thin-film heaters", Appl. Optics 39(28), 5109-5116 (2000).

[26] Ou, J. Z., Yaacob, M. H., Campbell, J. L., Breedon, M., Kalantar-zadeh, K. and Wlodarski, W., "$H_2$ sensing performance of optical fiber coated with nano-platelet $WO_3$ film", Sens. Actuators B Chem. 166, 1-6 (2012).

[27] Tabassum, S., Dong, L. and Kumar, R., "Heater integrated nanopatterned optical fiber-tip to realize a reusable gas sensor", in Proc. Photonic Fiber and Crystal Devices: Advances in Materials and Innovations in Device Applications XII, San Diego, CA, USA, vol. 10755, 2018.

[28] Mark, J. E., [Polymer Data Handbook], Oxford Univ. Press, New York, (1999).

[29] Oren, S., Ceylan, H. and Dong, L. "Helical-shaped graphene tubular spring formed within microchannel for wearable strain sensor with wide dynamic range", IEEE Sens. Lett. 1(6), 2501204 (2017).

# CHAPTER 5. DETERMINATION OF DYNAMIC VARIATIONS IN OPTICAL PROPERTIES OF GRAPHENE OXIDE IN RESPONSE TO GAS EXPOSURE BASED ON THIN-FILM INTERFERENCE

A paper published in Optics Express Journal

Shawana Tabassum, Liang Dong, and Ratnesh Kumar

## 5.1 Abstract

We present an effective yet simple approach to study the dynamic variations in optical properties (such as refractive index (RI)) of graphene oxide (GO) when exposed to gases in the visible spectral region, using thin-film interference method. The dynamic variations in complex refractive index of GO in response to exposure to a gas is an important factor affecting the performance of GO-based gas sensors. In contrast to the conventional ellipsometry, this method alleviates the need of selecting a dispersion model from among a list of model choices, which is limiting if an applicable model is not known a priori. In addition, the method used is computationally simpler, and does not need to employ any functional approximations. Further advantage over ellipsometry is that no bulky optics is required, and as a result it can be easily integrated into the sensing system, thereby allowing reliable, simple, and dynamic evaluation of the optical performance of any GO-based gas sensor. In addition, the derived values of the dynamically changing RI values of the GO layer obtained from the method we have employed are corroborated by comparing with the values obtained from ellipsometry.

## 5.2 Introduction

Graphene has attracted recent attention as a versatile sensing material, due to its sensitive electronic and optical properties, and ability to bind with many analytes. Because of large surface area-to-volume ratio [1] and remarkably high carrier mobility of graphene at

room temperature (200,000 $cm^2$ $V^{-1}$ $s^{-1}$) [2], graphene-based materials have been explored extensively in sensing, e.g., for gas [3-11] and biological applications [12-15]. The enormous potential of graphene-based materials in detecting minute concentrations of chemical and biological analytes due to the changes in its optical properties caused by the adsorption of the gases or analytes has led to a rising interest in utilizing graphene and its derivatives as gas adsorption and sensing materials. When the gas-sensing performance of pristine graphene is low owing to weaker adsorption of gas molecules on its surface, further functionalization of graphene is performed to improve its sensing performance. One such derivative of graphene is graphene oxide (GO), which is a two-dimensional monolayer comprising different oxygen containing functionalities (e.g., carboxyl, hydroxyl, carbonyl, and epoxide) with a very high sensitivity to surface adsorbates [16], hence making GO a promising choice for highly sensitive sensing material.

The knowledge of the changes in the optical parameters, namely, the complex refractive indices, of a material in response to adsorbed gases is necessary in designing a sensor based on the light transmission or reflection measurements. So, for example the optical properties of GO in a GO-based optical gas sensor are an important factor affecting its sensing performance, which vary depending on the amount of adsorbed gas species in the GO layer. Accordingly, and owing to a growing interest in studying GO as a sensing material, evolution of RI values of GO nanosheets upon their exposure to the ambient environment are worthy of investigation. In our recent works, we have developed plasmonic crystal [8, 9] and guided mode resonance-based nanostructures [10, 11], integrated with GO, to work as gas sensors, wherein the dynamic response of the sensor has been studied when exposed to gases. In such applications, studying the optical properties of GO is inevitably required to predict the sensor

performance. A knowledge of the refractive index (RI) values facilitates the verification of the experimental results against a theoretical model.

The refractive index of a material is in general a complex number, corresponding to the change in propagation speed of light through it owing to the dielectric interactions plus the losses caused by the ionic interactions, and varies with the wavelength. Several research efforts have been reported which studied the complex refractive index, and among those, ellipsometry is a popular reliable method to characterize the optical properties of the GO nanosheets [17-19]. Ellipsometry exploits the changes in the polarization state of the light reflected from a thin film of the material being probed to infer the optical properties (see the details provided in the Appendix). However, this requires choosing a fitting model (from among a number of model choices) to deduce the complex RI of the material from the measured intensity of p- and s-polarizations at different phase alignments. Choosing a correct fitting model requires a priori expert knowledge about the material, which may not always be available and becomes a limitation for ellipsometry. Further the models themselves are highly complex, involving multiple equations, leading to higher chances of numerical issues (such as getting trapped in a local optimum).

There exist other methods to compute the RI of a thin film such as the ATR (attenuated total reflection) intensity, DFT (density function theory), and RS (reflection spectroscopy) measurements. Cheon et al. determined the complex RI of graphene using two independent measurements, namely (i) measuring the light absorption by a thin gold (Au) layer coated with graphene at the SPR (surface plasmon resonance) critical angle, and (ii) using the ATR to measure the reflectance ratio of p-polarized to s-polarized light ($R_p/R_s$) wherein the incident light is attenuated by a bare graphene layer [20]. Thus a reliable determination of complex RI

of graphene was possible using two independent methods, and without using any target model fitting elaboration as in the case of ellipsometry. However, the SPR and ATR measurements are based on prism-coupling which makes the optical setup bulky and expensive. The DFT approach for finding the optical properties of a material is based on simulating the interactions between electrons in the material [21]. This method is widely applied for practical reasons that its simple approximations work well in predicting the structure of a material. But, DFT based RI calculations suffer from large errors because of the approximations made in constructing the exchange-correlation functionals [22]. In another report, Ni et al. [23] employed RS to compute the thickness of graphene. But, their computation was based on an overly simplified assumption of constant RI values of graphene in the entire visible range, which is unrealistic. Later, Bruna et al. modeled only the imaginary part of complex RI of graphene while keeping the real part constant [24]. So, there exists a need for developing an alternative that is experimentally and computationally simple to determine the complex RI of GO, overcoming the aforementioned limitations.

In contrast to the above methods, the thin-film interference that we employ utilizes only the maximum and minimum of the reflectance spectrum in order to compute the RI. The method is computationally simple, and does not need to employ any functional approximations, resulting in highly accurate and reliable results. Also, to the best of our knowledge, our work provides a first systematic experimental study to characterize the *dynamically evolving* optical properties of GO nanosheets in response to exposure to gas species. (As time progresses, more gases are adsorbed, causing higher changes in the RI values.)

In this paper, we characterize the dynamic evolution of the RI values of a GO thin film in response to exposure to a gas (namely, ammonia) by the method of thin-film interference as developed by Minkov [25]. We measured reflectance spectra of a GO thin film coated on a glass substrate over the visible spectra and at room temperature. The interaction of a probe beam reflected from multiple interfaces (air-film and film-glass) results in interference fringes in the reflection spectra. These reflection spectra of a GO thin film were monitored in response to exposure to ammonia, and analyzed to determine the dynamically evolving complex RI of the GO thin film. This sensitivity of RI to exposed gas concentration is crucial to the performance of the GO-based optical sensors. Finally, we compare our findings with results obtained by ellipsometry. Note, while ellipsometry is accurate, and hence we use it for comparison, it is not practical to be employable in studying the dynamic changes in RI of GO in response to exposure to analyte. Apart from the complexity of fitting model selection, physical constraints arise with using ellopsometry: gas sensing requires an enclosed experimental setup for which it is often not possible to integrate with a commercially available ellipsometer. In contrast, using the thin-film interference method that we use is (i) computationally universal (requiring no fitting model selection) and simpler (deals with an order less number of equations), (ii) highly accurate being based on only the reflectance spectra peaks, and also (iii) physically integrable into sensing system (so dynamically changing RI can be measured while sensing is occurring). This work resulted in the publications [26] and [27]. The key contributions of our work are as follows:

- Experimentally compute the *dynamic changes* in the refractive index (RI) of GO in a relatively simple and straightforward yet effective manner utilizing the theoretical foundation laid in [25].

- Demonstrate through experimental setup that the approach is physically integrable into the sensing system, which is a required attribute for being able to observe the dynamically changing RI in response to ongoing interaction with the analyte.

## 5.3 Details of the Experimentation Methods

### 5.3.1 GO Thin Film Preparation Method

To prepare a GO thin film on a glass substrate, aqueous suspensions of GO nanosheets (1 mg/mL) were prepared by thoroughly dispersing 1 mg of the synthesized GO nanosheet flakes (purchased from Graphene Supermarket) in 1 mL of deionized water, followed by sonication at room temperature for 90 min [8]. The GO dispersion solution was then sprayed onto a microscope glass slide using an airbrush (Badger 350, Badger Air-Brush Co.) [28]. The substrate was next dried at room temperature for 6 hrs, which let the remaining GO sheets to form a uniform thin film on the glass slide.

### 5.3.2 Characterization and Measurement Methods

The complex refractive index as well as the average thickness of GO thin film coated on glass substrate were determined from the thin-film interference fringes in the reflection spectra, following the method developed by Minkov [25]. A bifurcated optical fiber (BIF 400-VIS-NIR, Ocean Optics)---see Fig. 5.1(a)---was used to illuminate the sensor from a white light source (150 watt quartz halogen lamp, Luxtec Fiber Optics) through a collimator (F220SMA-A, Thorlabs), and to collect the reflected light from the GO surface into a spectrometer (USB-4000, Ocean Optics). We measured the reflectance spectra for a normal incident light. The optical setup and the measured reflection spectrum of the GO thin film are depicted in Figs. 5.1(a) and 5.1(b) respectively.

The scanning electron microscopy (SEM) analysis was performed to characterize the GO film coated on glass. The top-view and cross-section of GO thin film on glass substrate

are shown in Fig. 5.1(c). From the cross-section view, the thickness of the GO film was found to be approximately 650 nm.

Raman spectroscopy was also conducted to further characterize the GO film on glass. The Raman spectrum of GO depicts the characteristic peaks of D and G at 1354 $cm^{-1}$ and 1598 $cm^{-1}$ respectively (Fig. 5.1(d)). The D band corresponds to the presence of disorders in the GO nanosheets, whereas the G band is associated with C-C bond stretch in sp2 carbon domains [29].

### 5.4 Determining Refractive Index from Interference Fringes

We first provide the underlying principle. Suppose the GO thin film has a thickness $t$ and a complex refractive index $\boldsymbol{\eta}=\eta+ik$, where $\eta$ is the refractive index and $k$ the extinction coefficient and can be related to the absorption coefficient $\alpha=4\pi k/\lambda$, where $\lambda$ is the wavelength of light. The glass substrate has a thickness several orders of magnitude larger than $t$ and has index of refraction, denoted $\eta_s$. The interference fringes observed in the reflection spectrum of the GO film, are shown in Fig. 5.1(b). Such fringes in the reflectance spectrum of GO have also been observed in [30]. The interference fringes occur due to the reflections from the two interfaces, namely, air-GO and GO-glass interfaces. These fringes can be used to calculate the RI values of GO, noting that the reflectance $R$ is a function of $\eta, k, \eta_s, t, \lambda$ [25]:

$$R=\frac{A'-(B_1'\cos 2\delta-B_2'\sin 2\delta)x+C'x^2}{A''-(B_1''\cos 2\delta-B_2''\sin 2\delta)x+C''x^2}+\frac{A''x^2}{A''-(B_1''\cos 2\delta-B_2''\sin 2\delta)x+C''x^2}*\frac{1}{D''-(E_1''\cos 2\delta-E_2''\sin 2\delta)x+F''x^2} \tag{5.1}$$

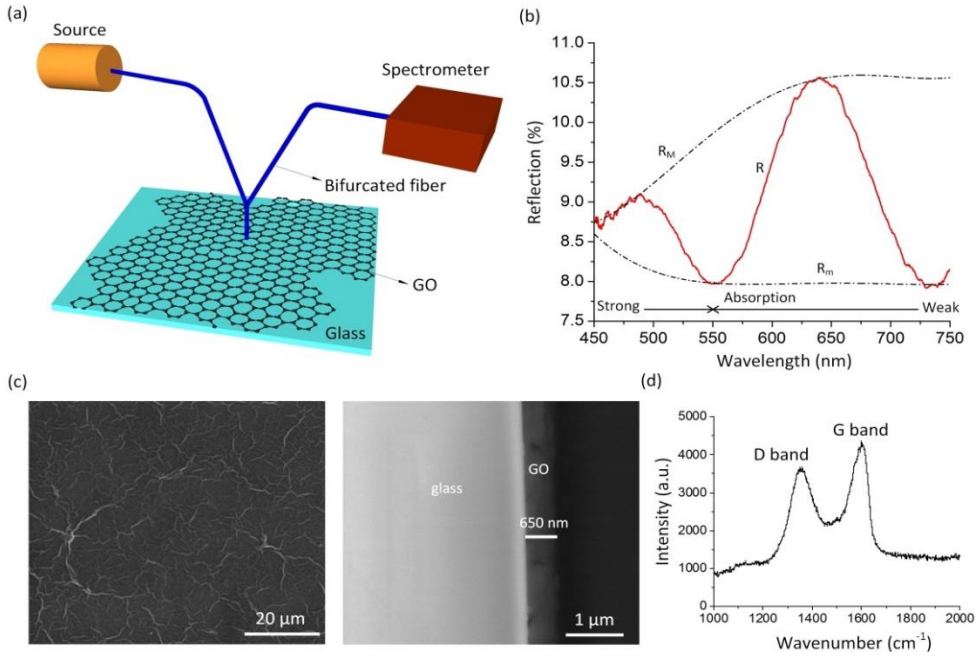


Fig. 5.1: *(a) Schematic illustration of optical setup for characterizing the optical properties of a GO thin film. (b) Reflection spectrum R of the GO thin film in air and the envelopes $R_M$ and $R_m$ as fitted to the maxima and minima of R, respectively. (c) SEM images of GO thin film on glass: top view (left) and cross section (right). (d) Raman spectrum of GO.*

where,

$$A' = [(\eta-1)^2+k^2][(\eta+\eta_s)^2+k^2]$$

$$B_1' = 2\left[\left(\eta^2+k^2-1\right)\left(\eta^2+k^2-\eta_s^2\right)+4k^2\eta_s\right]$$

$$B_2' = 4k[\eta_s\left(\eta^2+k^2-1\right)-\left(\eta^2+k^2-\eta_s^2\right)]$$

$$C' = [(\eta+1)^2+k^2][(\eta-\eta_s)^2+k^2]$$

$$A'' = [(\eta+1)^2+k^2][(\eta+\eta_s)^2+k^2]$$

$$B_1'' = 2\left[\left(\eta^2+k^2-1\right)\left(\eta^2+k^2-\eta_s^2\right)-4k^2\eta_s\right]$$

$$B_2'' = 4k\left[\eta_s\left(\eta^2+k^2-1\right)+\left(\eta^2+k^2-\eta_s^2\right)\right]$$

$$C'' = [(\eta-1)^2+k^2][(\eta-\eta_s)^2+k^2]$$

$$A''' = 64\eta_s\left(\eta_s-1\right)^2\left(\eta^2+k^2\right)^2$$

$$D'' = [(\eta+1)^2 + k^2][(\eta+1)(\eta+\eta_s^2) + k^2]$$

$$E_1'' = 2\left[\left(\eta^2 + k^2 - 1\right)\left(\eta^2 + k^2 - \eta_s^2\right) - 2k^2\left(\eta_s^2 + 1\right)\right]$$

$$E_2'' = 2k\left[\left(\eta^2 + k^2 - \eta_s^2\right) + \left(\eta_s^2 + 1\right)\left(\eta^2 + k^2 - 1\right)\right]$$

$$F'' = [(\eta-1)^2 + k^2][\left(\eta-1\right)\left(\eta - \eta_s^2\right) + k^2]$$

$x = \exp(-\alpha t)$ and $\delta = \dfrac{2\pi\eta t}{\lambda}$

Noting that $\alpha$ is a function of $k, \lambda$, the above parameters are functions of $\eta, k, \eta_s, t, \lambda$, the first 4 of which are unknowns and need to be determined, while the parameter $\lambda$ is measured.

The extremes of the interference fringes, represented by the envelopes $R_M$ and $R_m$ (see Fig. 5.1(b)) are given as [25]:

$$\begin{aligned} R_M &= \frac{(ad+bcx)^2}{(bd+acx)^2} + \frac{gx^2}{(bd+acx)^2(b^3 f + 2abcdx + a^3 ex^2)} \\ R_m &= \frac{(ad-bcx)^2}{(bd-acx)^2} + \frac{gx^2}{(bd-acx)^2(b^3 f - 2abcdx + a^3 ex^2)} \end{aligned} \tag{5.2}$$

where, $a = \eta - 1$, $b = \eta + 1$, $c = \eta - \eta_s$, $d = \eta + \eta_s$, $e = \eta - \eta_s^2$, $f = \eta + \eta_s^2$ and $g = 64\eta_s\left(\eta_s - 1\right)^2\eta^4$ .Note all these parameters are functions of $\eta$ and $\eta_s$, and since $x$ is a function of $k, t, \lambda$, ultimately, $R_M, R_m$ are functions of $\eta, k, \eta_s, t, \lambda$. So by measuring $R_M, R_m$ as functions of $\lambda$, we can determine the unknowns $\eta, k, \eta_s, t$. In particular, in the transparent region of the spectrum, the refractive index of glass substrate, $\eta_s$ can be determined as [25]:

$$\eta_s = \frac{1 + [R_m(2 - R_m)]^{1/2}}{1 - R_m} \tag{5.3}$$

Further, a basic equation for interference fringes that can be used to determine the thickness $t$ is [25]:

$$4\eta t = m\lambda \tag{5.4}$$

where, an odd order number $m$ corresponds to the wavelength for which $R$ has a maximum, and even order number $m$ corresponds to wavelength for which $R$ has a minimum (see Fig. 5.1(b) for $R$ versus $R_m$ versus $R_M$). It follows from Eq. (5.4) that if $\eta_1$ and $\eta_2$ are the refractive indices calculated from a pair of adjacent extrema that correspond to the wavelengths $\lambda_1$ and $\lambda_2$, respectively, then the film thickness can be determined using [25]:

$$t = \frac{\lambda_1 \lambda_2}{4(\lambda_1 \eta_2 - \lambda_2 \eta_1)} \tag{5.5}$$

In summary, the steps to determine the complex refractive index of GO that we used are as listed below:

1. To start, the refractive index of the glass substrate $\eta_s$ was calculated from the envelope $R_m$ in the spectral region of weak absorption, using Eq. (5.3). For example, in Fig. 5.1(b), in the weak absorption region $R_m$= 8 %, providing $\eta_s$ = 1.51, which is a typical average value of RI for glass in the visible spectral region. The reflectance (and hence refractive index) of bare glass was almost constant in the visible spectral region (using Eq. (5.3)). This is also supported by the observations in [31]. Further, we also measured the optical constants of the same sample using ellipsometry, and the results were found close to the values calculated using thin-film interference. The ellipsometry results are demonstrated later in Fig. 5.3. The proximity of the measurements from the two approaches (ellipsometry vs. thin-film interference) confirms that the refractive index change of glass, if any, was not significant to influence the results of RI measurements of the thin-film GO.

2. Next, Newton-Raphson iteration was used to solve the system of two equations Eq. (5.2) for the two unknowns $\eta$ and $x$ (where note that $\eta_s$ is known at this point from the first step above), using the measured values of $R_M$ and $R_m$ , which are the peaks and valleys of the interference spectrum respectively (values listed in Table 5.1). In order to achieve faster

convergence, computations were started for $\lambda$ in the weak absorption region ($\lambda$ = 734.6 nm), where the initial estimate $x^0$ was presumed to be 0.8, and similarly an initial estimate was chosen for $\eta^0$ [25]. For the $(j+1)$th iteration, $\eta^j$ and $x^j$ values were used from the previous $j$th iteration, and the final converged values of refractive index and absorbance were denoted $\eta$ and $x$ respectively.

3. In order to calculate $\eta$ and $x$ values for a next $\lambda$ value, $\eta$ and $x$ values obtained for the previous extremum were used as initial estimates. For example, to obtain $\eta$ and $x$ values of GO film in air and at $\lambda$ = 640.2 nm, $\eta^0$ = 1.86 and $x^0$ = 0.2289 obtained for $\lambda$ = 734.6 nm were used as initial estimates. The same procedure was followed for all the successive $\lambda$ values. Thus, the $\eta$ and $x$ columns listed in Table 5.1 were obtained.

4. The next step was to estimate the GO thickness, $t$ using the $\eta$ values of two neighboring extrema by applying Eq. (5.5). Accordingly, various estimates of thickness $t$ of the GO film as listed in Table 5.1 were obtained, and from which the averaged value $\bar{t}$ was calculated.

5. Subsequently, the order numbers $m$ were calculated by substituting $\eta$ and the average value $\bar{t}$ of thicknesses for all the wavelengths, in Eq. (5.4). The order numbers $m$ were next approximated as the consecutive integers.

6. Next, the accuracy of $t$ was significantly increased by taking the $m$ values associated to each extremum and deriving a new thickness approximation $t^f$, where $t^f$ was calculated by substituting the values of $\eta$ and $m$ in Eq. (5.4). This was also confirmed by noting that the values of $t^f$ have smaller variances compared to $t$ values ($\sigma_{t^f} \ll \sigma_t$).

7. The final value of refractive index $\eta^f$ was found from Eq. (5.4) using the calculated values of the average thickness, $\overline{t^f}$ and order numbers, $m$.

8. Finally, the value of $k$ for each $\lambda$ was found by solving Eq. (5.1) for the envelope $R_M$.

### 5.5 Experimental Description, Results, and Discussion

The RI values of GO were determined in air and in presence of ammonia ($NH_3$) gas, using the method described in the section above. Gaseous ammonia (pre-diluted with the carrier gas of dry nitrogen) flowed from a cylinder into an aluminum gas chamber which contained the GO coated glass slide. The gas flow rate was controlled by a mass flow controller (MFC) (GFC17, Aalborg). Inside the chamber, the testing gas was further diluted by the carrier nitrogen gas. A constant flow rate of dry nitrogen (10 ml/min) was maintained inside the closed chamber and flow rate of ammonia was varied at regular intervals using the MFCs to modify the concentration of the gaseous ammonia. The GO thin film was illuminated from a white light source through a bifurcated fiber and the reflected light was collected by a spectrometer. From the flow rates of ammonia and nitrogen gases, the ppm level of gaseous ammonia was obtained by doing some mathematical calculations. Also, prior to the dynamic measurements of gaseous ammonia mixed with nitrogen, the baseline response was monitored in presence of only the nitrogen gas.

No observable change in interference pattern was observed for ammonia concentrations below 200 ppm, while the response saturated at 500 ppm. So the measurement results are shown for 200, 300 and 500 ppm. Also, while the measurements were taken at four different wavelengths of 734.6 nm, 640.2 nm, 551.5 nm, and 489.9 nm, it turned out that at 489.9 nm, the optical absorption was dominant, dampening the interference fringes. Consequently, the results were not reliable, and we chose to omit the extinction coefficient data at 489.9. nm Subsequent to the measurements, we purged the GO thin film with dry nitrogen and next with heating at $70^0$C for approximately 2 hrs to completely desorb the gas molecules from the film. This is required to perform a next experiment. The heating process restored the initial refractive index of the bare GO film as confirmed by the baseline measurements.

Figs. 5.2(a) and 5.2(b) demonstrate the shift in intereference patterns of the GO with exposure to ammonia gas over a 44 min period, resulting in a dynamically evolving RI. The presence of a strong interference oscillations above 550 nm implies a spectral region of weak absorption. The onset of stronger absorption below 550 nm is represented as dampening of the fringes. The calculated values of $\eta$ and $k$ from the envelopes $R_M$ and $R_m$ of the reflectance spectrum of a GO thin film, shown in Fig. 5.2(a), are tabulated in Table 5.1. Note while the final thickness and final refractive index after iteration are more accurate, the intermediate values of refractive index and thickness are shown to illustrate all the steps of the algorithm. It shows the progress of the iterative computations, showing the completeness of the work. Only the final thickness and final refractive index were used to draw conclusions and make comparison with ellipsometry.

### 5.5.1 Dynamic Variations in $\eta^f$ and $k$ and Thickness Calculation

The dynamic variations of $\eta^f$ and $k$ values of the GO nanosheets exposed to three different concentrations of ammonia gas (200 ppm, 300 ppm, and 500 ppm), are illustrated in Figs. 5.2(c) and 5.2(d). Additionally, Table 5.1 also summarizes the dynamic variation in RI of GO by listing in successive columns, the values of $R_M$, $R_m$, $\eta$, $x$, $t$, $m$, $t^f$, $\eta^f$, $k$, while the rows list the wavelengths at which the column values are computed. The rows are further organized in successive blocks corresponding to the values after each additional 4 mins of gas exposure (so with a total of 44 mins of gas exposure, there are a total of 12 blocks, where the 1st block is for time zero).

The calculated values of $\eta^f$ and $k$ of the GO film in air are 1.8714 and 0.1613 respectively at the wavelength of 640.2 nm. Initally, the sensor was exposed to 200 ppm of

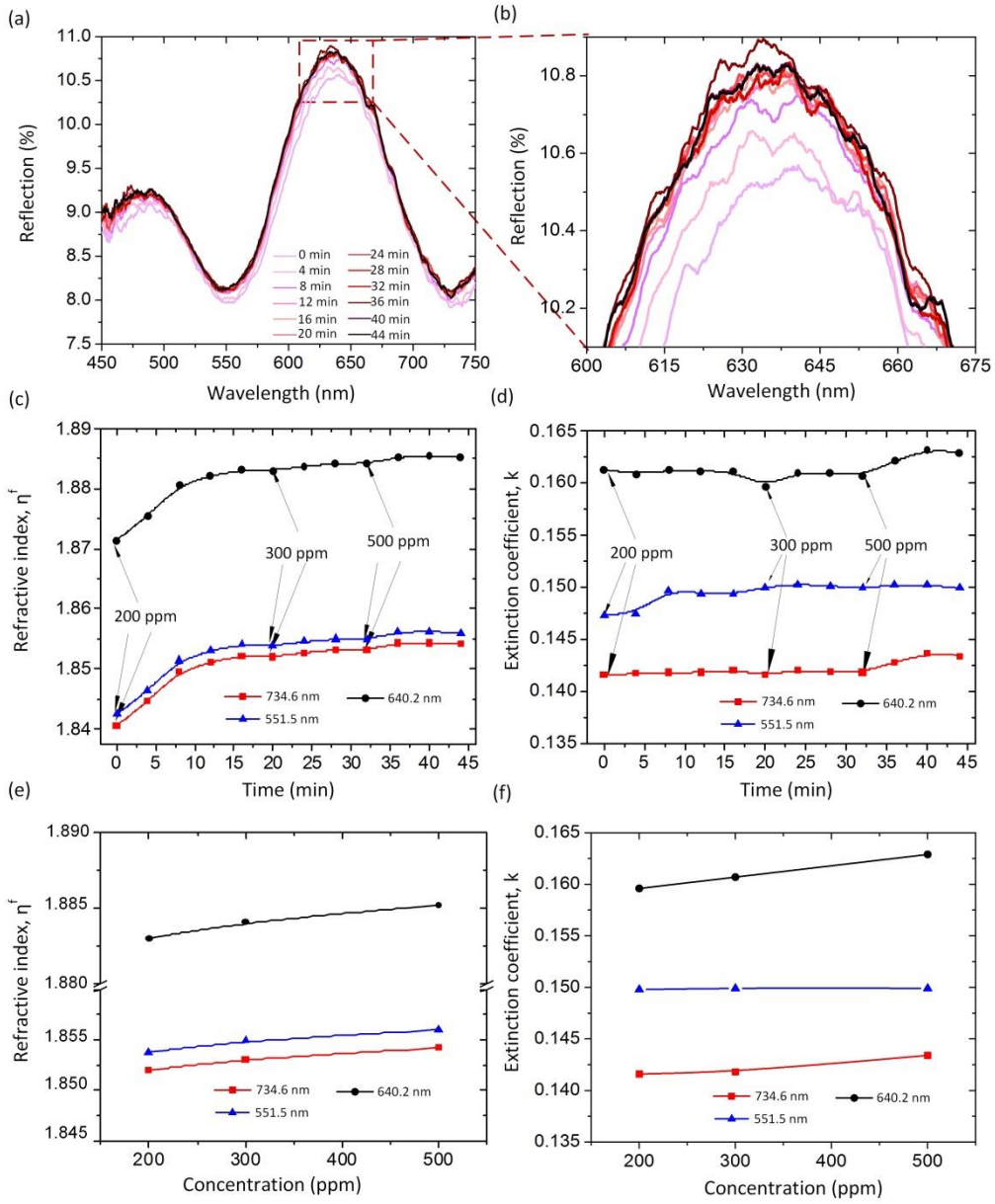


Fig. 5.2: *(a) Dynamic evolution of reflectance spectra upon exposure to ammonia gas over 44 mins. (b) Zoomed-in spectra from the region denoted by red dashes in (a), emphasizing the shifts in interference fringes in response to gas exposure. Dynamic variation of (c) refractive index and (d) extinction coefficient in exposure to ammonia gas and at different wavelengths of light. Arrows denote the instants at which the GO thin film was exposed to 200, 300 and 500 ppm of ammonia gas. Shifts in (e) refractive index and (f) extinction coefficient as a function of concentration of ammonia gas.*

gaseous ammonia. It can be observed that the $\eta^f$ values of GO increased over time as it was exposed to the gas for longer and longer times. This is expected because the large number of

functional groups at the GO surface can effectively capture the gas molecules which enhances the RI of GO [32, 33]. In the beginning, for each wavelength, the rate of increase of $\eta^f$ was high. However, after 8 min, the rate of increase slowed down and at approximately 16 min, $\eta^f$ values started to saturate, likely because the gas molecules already remaining in the GO layer inhibited further interaction and hence adsorption of newer gas molecules. After the sensor response was saturated to $\eta^f$ = 1.883 for 200 ppm of ammonia gas (for λ = 640.2 nm), the sensor was successively exposed to 300 ppm, and 500 ppm of gaseous ammonia. The $\eta^f$ values of the GO thin film increased successively by 0.0116, 0.0009, and 0.0011 refractive index unit (RIU) in response to 200 ppm, 300 ppm, and 500 ppm ammonia gas respectively. Similarly, extinction coefficient curve, $k$ which accounts for light absorption by the GO film initially increased over time and saturated after some time for each concentration of gaseous ammonia. The calculated average thickness of GO thin film in air was 624 nm (Table 5.1) which is close to 650 nm, the actual thickness observed from SEM analysis (Fig. 5.1(c)). In the plot of $\eta$ and $k$ vs. the wavelength (Fig. 5.3), the peak at 640 nm suggests the occurrence of a dielectric relaxation mode of the GO layer. Similar phenomena has also been observed in [34].

**5.5.2 Sensitivity Studies**

Figs. 5.2(e) and 5.2(f) show shifts in RI values with a change in gas concentration. The $\eta^f$ and $k$ sensitivity of the sensor in response to ammonia gas was found to be $6.5 \times 10^{-6}$ RIU/ppm and $9.86 \times 10^{-6}$ RIU/ppm respectively at λ = 640.2 nm. The lower sensitivities at wavelengths of 734 nm and 551 nm suggest that λ = 640.2 nm is better suited for optical sensing. Here, refractive index (RI) is defined in the standard way as the ratio of speed of light in vacuum to the speed of light in the medium. The sensitivity in terms of RIU/ppm provides the change in refractive index of the GO film against the change in gas concentration.

### 5.6 Comparison to Ellipsometry

The experimentally determined RI values of bare GO film (without the presence of any gas) in this work were further compared to the RI values of the same sample measured using ellipsometry. This is shown in the Fig. 5.3 below. The measured results using ellipsometry were found close to the values calculated using thin-film interference, with a maximum variation of ~0.4%, adding confidence to our method and results. This verifies the accuracy of thin-film interference method in computing RI of GO. The error bars represent a maximum standard deviation of ~±0.2%. The dynamic measurement of RI values of GO in response to exposure to gas is a unique and novel feature to our study, absent in prior studies [17-19].

Table 5.1. *The calculated values of complex refractive index ($\eta + ik$) and thickness ($t$) of GO are based on the fringe interference method [25]*

| $\lambda$ (nm) | $R_M$ (%) | $R_m$ (%) | $\eta$ | $x$ | $t$ (nm) | $m$ | $t^f$ (nm) | $\eta^f$ | $k$ |
|---|---|---|---|---|---|---|---|---|---|
| in air | | | | | | | | | |
| 734.6 | 10.55 | 7.960 | 1.8600 | 0.2289 | 667 | 6 | 592 | 1.8405 | 0.1416 |
| 640.2 | 10.55 | 7.977 | 1.8609 | 0.2268 | 573 | 7 | 602 | 1.8714 | 0.1613 |
| 551.5 | 9.878 | 7.977 | 1.8436 | 0.1770 | 633 | 8 | 598 | 1.8424 | 0.1473 |
| 489.9 | 9.112 | 8.189 | 1.8311 | 0.0895 | - | 9 | 602 | 1.8412 | - |
| $\bar{t}$ = 624 nm, $\sigma_t$ = 47 nm, $\overline{t^f}$ = 598 nm, $\sigma_{t^f}$ = 4.5 nm | | | | | | | | | |
| After 4min of exposure to ammonia gas | | | | | | | | | |
| 734.6 | 10.63 | 8.029 | 1.8654 | 0.2259 | 668 | 6 | 590 | 1.8446 | 0.1417 |
| 640.2 | 10.63 | 8.027 | 1.8653 | 0.2262 | 572 | 7 | 600 | 1.8755 | 0.1608 |
| 551.5 | 9.950 | 8.027 | 1.8478 | 0.1765 | 638 | 8 | 597 | 1.8464 | 0.1475 |
| 489.9 | 9.150 | 8.218 | 1.8334 | 0.0895 | - | 9 | 601 | 1.8452 | - |
| $\bar{t}$ = 626 nm, $\sigma_t$ = 49 nm, $\overline{t^f}$ = 597 nm, $\sigma_{t^f}$ = 4.8 nm | | | | | | | | | |
| After 8min of exposure to ammonia gas | | | | | | | | | |
| 734.6 | 10.73 | 8.091 | 1.8710 | 0.2253 | 667 | 6 | 589 | 1.8496 | 0.1418 |
| 640.2 | 10.72 | 8.084 | 1.8704 | 0.2254 | 572 | 7 | 599 | 1.8806 | 0.1612 |
| 551.5 | 10.02 | 8.084 | 1.8522 | 0.1752 | 634 | 8 | 595 | 1.8514 | 0.1497 |
| 489.9 | 9.220 | 8.292 | 1.8384 | 0.0878 | - | 9 | 599 | 1.8502 | - |
| $\bar{t}$ = 624 nm, $\sigma_t$ = 48 nm, $\overline{t^f}$ = 595 nm, $\sigma_{t^f}$ = 4.8 nm | | | | | | | | | |

Table 5.1. (continued)

| | | | | | | | | | |
|---|---|---|---|---|---|---|---|---|---|
| After 12min of exposure to ammonia gas | | | | | | | | | |
| 734.6 | 10.76 | 8.109 | 1.8726 | 0.2251 | 666 | 6 | 588 | 1.8511 | 0.1418 |
| 640.2 | 10.75 | 8.102 | 1.8720 | 0.2253 | 571 | 7 | 598 | 1.8821 | 0.1611 |
| 551.5 | 10.05 | 8.102 | 1.8538 | 0.1753 | 634 | 8 | 595 | 1.8530 | 0.1494 |
| 489.9 | 9.250 | 8.305 | 1.8398 | 0.0890 | - | 9 | 599 | 1.8518 | - |
| $\bar{t}$ = 624 nm, $\sigma_t$ = 48 nm, $\overline{t^f}$ = 595 nm, $\sigma_{t^f}$ = 4.8 nm | | | | | | | | | |
| After 16min of exposure to ammonia gas | | | | | | | | | |
| 734.6 | 10.78 | 8.119 | 1.8736 | 0.2253 | 666 | 6 | 588 | 1.8522 | 0.1420 |
| 640.2 | 10.77 | 8.112 | 1.8730 | 0.2255 | 571 | 7 | 598 | 1.8832 | 0.1611 |
| 551.5 | 10.07 | 8.112 | 1.8548 | 0.1757 | 633 | 8 | 594 | 1.8541 | 0.1493 |
| 489.9 | 9.271 | 8.321 | 1.8411 | 0.0891 | - | 9 | 598 | 1.8528 | - |
| $\bar{t}$ = 623 nm, $\sigma_t$ = 48 nm, $\overline{t^f}$ = 595 nm, $\sigma_{t^f}$ = 4.8 nm | | | | | | | | | |
| After 20min of exposure to ammonia gas | | | | | | | | | |
| 734.6 | 10.78 | 8.114 | 1.8734 | 0.2259 | 666 | 6 | 588 | 1.8520 | 0.1416 |
| 640.2 | 10.78 | 8.105 | 1.8729 | 0.2270 | 572 | 7 | 598 | 1.8830 | 0.1596 |
| 551.5 | 10.06 | 8.105 | 1.8542 | 0.1757 | 631 | 8 | 594 | 1.8538 | 0.1498 |
| 489.9 | 9.254 | 8.334 | 1.8411 | 0.0862 | - | 9 | 598 | 1.8526 | - |
| $\bar{t}$ = 623 nm, $\sigma_t$ = 47 nm, $\overline{t^f}$ = 595 nm, $\sigma_{t^f}$ = 4.8 nm | | | | | | | | | |
| After 24min of exposure to ammonia gas | | | | | | | | | |
| 734.6 | 10.79 | 8.127 | 1.8742 | 0.2250 | 665 | 6 | 588 | 1.8527 | 0.1420 |
| 640.2 | 10.78 | 8.123 | 1.8738 | 0.2248 | 572 | 7 | 598 | 1.8837 | 0.1610 |
| 551.5 | 10.07 | 8.123 | 1.8553 | 0.1744 | 634 | 8 | 594 | 1.8545 | 0.1503 |
| 489.9 | 9.265 | 8.328 | 1.8412 | 0.0878 | - | 9 | 598 | 1.8533 | - |
| $\bar{t}$ = 624 nm, $\sigma_t$ = 47 nm, $\overline{t^f}$ = 594 nm, $\sigma_{t^f}$ = 4.8 nm | | | | | | | | | |
| After 28min of exposure to ammonia gas | | | | | | | | | |
| 734.6 | 10.80 | 8.135 | 1.8749 | 0.2247 | 666 | 6 | 587 | 1.8532 | 0.1419 |
| 640.2 | 10.79 | 8.127 | 1.8742 | 0.2250 | 571 | 7 | 597 | 1.8842 | 0.1609 |
| 551.5 | 10.08 | 8.127 | 1.8558 | 0.1747 | 634 | 8 | 594 | 1.8550 | 0.1501 |
| 489.9 | 9.270 | 8.332 | 1.8415 | 0.0878 | - | 9 | 598 | 1.8538 | - |
| $\bar{t}$ = 624 nm, $\sigma_t$ = 48 nm, $\overline{t^f}$ = 594 nm, $\sigma_{t^f}$ = 4.9 nm | | | | | | | | | |
| After 32min of exposure to ammonia gas | | | | | | | | | |
| 734.6 | 10.80 | 8.134 | 1.8748 | 0.2249 | 666 | 6 | 587 | 1.8531 | 0.1418 |
| 640.2 | 10.79 | 8.126 | 1.8742 | 0.2251 | 571 | 7 | 597 | 1.8841 | 0.1607 |
| 551.5 | 10.08 | 8.126 | 1.8557 | 0.1748 | 635 | 8 | 594 | 1.8549 | 0.1499 |
| 489.9 | 9.267 | 8.330 | 1.8413 | 0.0878 | - | 9 | 598 | 1.8537 | - |
| $\bar{t}$ = 624 nm, $\sigma_t$ = 48 nm, $\overline{t^f}$ = 594 nm, $\sigma_{t^f}$ = 4.9 nm | | | | | | | | | |

Table 5.1. (continued)

| | | | | | | | | | |
|---|---|---|---|---|---|---|---|---|---|
| After 36min of exposure to ammonia gas | | | | | | | | | |
| 734.6 | 10.81 | 8.139 | 1.8753 | 0.2249 | 665 | 6 | 587 | 1.8543 | 0.1428 |
| 640.2 | 10.80 | 8.132 | 1.8747 | 0.2251 | 570 | 7 | 597 | 1.8853 | 0.1621 |
| 551.5 | 10.10 | 8.132 | 1.8565 | 0.1756 | 627 | 8 | 594 | 1.8561 | 0.1502 |
| 489.9 | 9.319 | 8.369 | 1.8444 | 0.0881 | - | 9 | 597 | 1.8549 | - |
| $\bar{t}$ = 621 nm, $\sigma_t = 47$ nm, $\overline{t^f}$ = 594 nm, $\sigma_{tf} = 4.7$ nm | | | | | | | | | |
| After 40min of exposure to ammonia gas | | | | | | | | | |
| 734.6 | 10.80 | 8.145 | 1.8754 | 0.2236 | 666 | 6 | 587 | 1.8543 | 0.1436 |
| 640.2 | 10.79 | 8.134 | 1.8746 | 0.2242 | 570 | 7 | 597 | 1.8854 | 0.1632 |
| 551.5 | 10.10 | 8.134 | 1.8566 | 0.1754 | 627 | 8 | 594 | 1.8562 | 0.1502 |
| 489.9 | 9.324 | 8.365 | 1.8444 | 0.0889 | - | 9 | 597 | 1.8550 | - |
| $\bar{t}$ = 621 nm, $\sigma_t = 48$ nm, $\overline{t^f}$ = 594 nm, $\sigma_{tf} = 4.7$ nm | | | | | | | | | |
| After 44min of exposure to ammonia gas | | | | | | | | | |
| 734.6 | 10.80 | 8.143 | 1.8753 | 0.2238 | 666 | 6 | 587 | 1.8542 | 0.1434 |
| 640.2 | 10.79 | 8.132 | 1.8745 | 0.2244 | 570 | 7 | 597 | 1.8852 | 0.1629 |
| 551.5 | 10.10 | 8.132 | 1.8565 | 0.1756 | 627 | 8 | 594 | 1.8560 | 0.1499 |
| 489.9 | 9.322 | 8.363 | 1.8442 | 0.0889 | - | 9 | 597 | 1.8548 | - |
| $\bar{t}$ = 621 nm, $\sigma_t = 48$ nm, $\overline{t^f}$ = 594 nm, $\sigma_{tf} = 4.7$ nm | | | | | | | | | |

In contrast to ellipsometry, our method of determining the RI of GO is (i) easier, requiring no model selection, and (ii) also less time consuming. Our method employs the same algorithm to determine the complex RI of GO at different time of exposure to gas. In contrast, in ellipsometry, for each time exposure, a regression analysis needs to be performed in which model parameters are varied until the calculated and the experimental data closely match. This makes the ellipsometry much tedious and time consuming, especially for dynamic RI measurements. On the other hand, thin-film intereference method is affected with small film thickness or with highly absorbing material since those affect the formation of the interference fringes suitable for measurements.

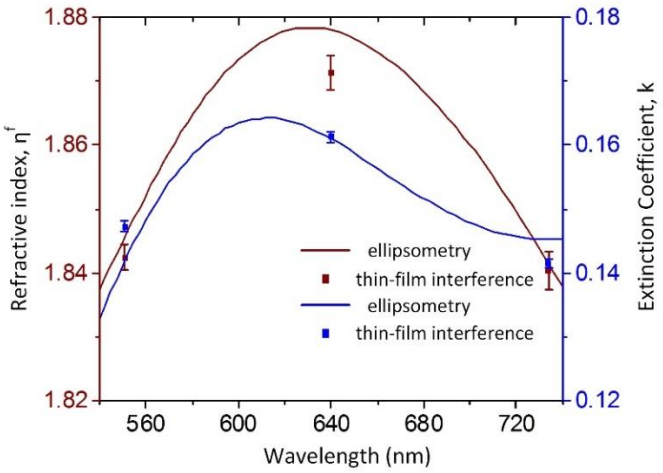


Fig. 5.3: *Comparison of the derived complex RI of bare GO film using thin-film interference with that of ellipsometry.*

## 5.7 Conclusion

We presented an effective yet simple method based on thin-film interference to determine the dynamic changes in the optical RI values of a GO thin flim in response to its exposure to the ammonia gas over time, and at multiple wavelengths. Note since the prior works only measured the RI values in air, the dynamic measurements of RI values upon exposure to gas is a unique and novel feature of our work. Also, our method, unlike ellipsometry, allows a straightforward determination of both the real and imaginary components of refractive index of GO with no need for any model fitting elaboration, is computationally simple needing an order fewer equations to solve and thus less time consuming, and is also physically integrable into the sensing system for making the dynamic RI change measurements feasible. For validating our method, we showed that the obtained RI values of the GO layer are comparable to those obtained from ellipsometry. Our method also correctly measured the film thickness, further validating its accuracy. Developing a detailed understanding of the optical properties of graphene oxide plays a significant role in characterizing the performance as an optical sensor. Thereby, the presented method of

determining the optical RI values of a GO layer helps support the principle of optical sensing for GO-based gas sensors. It also provides a way to select a wavelength where the sensivity of the RI to gas concentration is the highest.

## 5.8 References


[1] D. Chen, H. Feng, and J. Li, "Graphene oxide: preparation, functionalization, and electrochemical applications", Chem. Rev. **112**(11), 6027-6053 (2012).

[2] W. Yuan, and G. Shi, "Graphene-based gas sensors", J. Mater. Chem. A **1**(35), 10078-10091 (2013).

[3] A. Lipatov, A. Varezhnikov, P. Wilson, V. Sysoev, A. Kolmakov, and A. Sinitskii, "Highly selective gas sensor arrays based on thermally reduced graphene oxide", Nanoscale **5**(12), 5426-5434 (2013).

[4] S. Prezioso, F. Perrozzi, L. Giancaterini, C. Cantalini, E. Treossi, V. Palermo, M. Nardone, S. Santucci, and L. Ottaviano, "Graphene oxide as a practical solution to high sensitivity gas sensing", J. Phys. Chem. C **117**(20), 10683-10690 (2013).

[5] G. Ko, H. –Y. Kim, J. Ahn, Y. –M. Park, K. –Y. Lee, and J. Kim, "Graphene-based nitrogen dioxide gas sensors", Current Appl. Phys. **10**(4), 1002-1004 (2010).

[6] H. J. Yoon, D. H. Jun, J. H. Yang, Z. Zhou, S. S. Yang, and M. M. –C. Cheng, "Carbon dioxide gas sensor using a graphene sheet", Sens. Actuators B: Chem. **157**(1), 310-313 (2011).

[7] M. Cittadini, M. Bersani, F. Perrozzi, L. Ottaviano, W. Wlodarski, and A. Martucci, "Graphene oxide coupled with gold nanoparticles for localized surface plasmon resonance based gas sensor", Carbon **69**, 452-459 (2014).

[8] S. Tabassum, Q. Wang, W. Wang, S. Oren, M. A. Ali, R. Kumar, and L. Dong, "Plasmonic crystal gas sensor incorporating graphene oxide for detection of volatile organic compounds", in *Proceedings of IEEE 29$^{th}$ International Conference on Micro Electro Mechanical Systems* (IEEE, 2016), pp. 913-916.

[9] S. Tabassum, R. Kumar, and L. Dong, "Plasmonic crystal based gas sensor towards an optical nose design", IEEE Sensors J. **17**(19), 6210-6223 (2017).

[10] S. Tabassum, Y. Wang, J. Qu, Q. Wang, S. Oren, R. J. Weber, M. Lu, R. Kumar, and L. Dong, "Patterning of nanophotonic structures at optical fiber tip for refractive index sensing", in *Proceedings of IEEE Sensors* (IEEE, 2016), pp. 1-3.

[11] S. Tabassum, R. Kumar, and L. Dong, "Nanopatterned optical fiber tip for guided mode resonance and application to gas sensing", IEEE Sensors J. **17**(22), 7262-7272 (2017).

[12] M. A. Ali, S. Tabassum, Q. Wang, Y. Wang, R. Kumar and L. Dong, "Plasmonic-electrochemical dual modality microfluidic sensor for cancer biomarker detection", in *Proceedings of IEEE 30th International Conference on Micro Electro Mechanical Systems* (IEEE, 2017), pp. 390-393.

[13] M. A. Ali, S. Tabassum, Q. Wang, Y. Wang, R. Kumar and L. Dong, "Integrated dual-modality microfluidic sensor for biomarker detection using lithographic plasmonic crystal", Lab Chip, DOI: 10.1039/C7LC01211J (2018).

[14] M. A. Ali, C. Singh, S. Srivastava, P. Admane, V. V. Agrawal, G. Sumana, R. John, A. Panda, L. Dong, and B. D. Malhotra, "Graphene oxide-metal nanocomposites for cancer biobarker detection", RCS Adv. **7**(57), 35982-35991 (2017).

[15] H. Li, J. He, S. Li, and A. P. F. Turner, "Electrochemical immunosensor with N-doped graphene-modified electrode for label-free detection of the breast cancer biomarker CA 15-3", Biosens. Bioelectron. **43**(1), 25-29 (2013).

[16] S. S. Nanda, D. K. Yi, and K. Kim, "Study of antibacterial mechanism of graphene oxide using Raman spectroscopy", Sci. Rep. **6**, 28443 (2016).

[17] S. Schoche, N. Hong, M. Khorasaninejad, A. Ambrosio, E. Orabona, P. Maddalena, and F. Capasso, "Optical properties of graphene oxide and reduced graphene oxide determined by spectroscopic ellipsometry", Appl. Surface Sci. **421**, 778-782 (2017).

[18] V. G. Kravets, O. P. Marshall, R. R. Nair, B. Thackray, A. Zhukov, J. Leng, and A. N. Grigorenko, "Engineering optical properties of a graphene oxide metamaterial assembled in microfluidic channels", Opt. Express **23**(2), 1265-1275 (2015).

[19] I. Jung, M. Vaupel, M. Pelton, R. Piner, D. A. Dikin, S. Stankovich, J. An, and R. S. Ruoff, "Characterization of thermally reduced graphene oxide by imaging ellipsometry", J. Phys. Chem. C **112**(23), 8499-8506 (2008).

[20] S. Cheon, K. D. Kihm, H. goo Kim, G. Lim, J. S. Park, and J. S. Lee, "How to reliably determine the complex refractive index (RI) of graphene by using two independent measurement constraints", Sci. Rep. **4**, 6364 (2014).

[21] M. Turowski, T. Amotchkina, H. Ehlers, M. Jupe, and D. Ristau, "Calculation of optical and electronic properties of modeled titanium dioxide films of different densities", Appl. Optics **53**(4), A159-A168 (2014).

[22] A. J. Cohen, P. M. Sanchez, and W. Yang, "Insights into current limitations of density functional theory", Science **321**(5890), 792-794 (2008).

[23] Z. H. Ni, H. M. Wang, J. Kasim, H. M. Fan, T. Yu, Y. H. Wu, Y. P. Feng, and Z. X. Shen, "Graphene thickness determination using reflection and contrast spectroscopy", Nano Lett. **7**(9), 2758-2763 (2007).

[24] M. Bruna, and S. Borini, “Optical constants of graphene layers in the visible range”, Appl. Phys. Lett. **94**(3), 031901-031903 (2009).

[25] D. A. Minkov, “Calculation of the optical constants of a thin layer upon a transparent substrate from the reflection spectrum”, J. Phys. D: Appl. Phys. **22**(8), 1157-1161 (1989).

[26] S. Tabassum, L. Dong, and R. Kumar, “Dynamic variations in optical properties of graphene oxide in response to gas exposure as determined from thin-film interference”, in Proc. Fiber Optic Sensors and Applications XV, Orlando, Fl, USA, **10654** (2018).

[27] S. Tabassum, L. Dong, and R. Kumar, “Determination of dynamic variations in the optical properties of graphene oxide in response to gas exposure based on thin-film interference”, Opt. Express **26**(5), 6331-6344 (2018).

[28] S. H. Fei, W. Can, S. Z. Pei, Z. Y. Liang, J. K. Juan, and Y. G. Zhen, “Transparent conductive reduced grahene oxide thin films produced by spray coating”, Sci. China-Phys. Mech. Astron. **58**(1), 014202 (2015).

[29] R. Ramachandran, M. Saranya, P. Kollu, B. P. C. Raghupathy, S. K. Jeong, and A. N. Grace, “Solvothermal synthesis of Zinc sulfide decorated graphene (ZnS/G) nanocomposites for novel supercapacitor electrodes”, Elect. Acta **178**, 647-657 (2015).

[30] S. –H. Hong, and J. –K. Song, “Comment on “Tunable Design of Structural Colors Produced by Pseudo-1D Photonic Crystals of Graphene Oxide” and Thin-Film Interference from Dried Graphene Oxide Film”, Small **13**(15), 1603125 (2017).

[31] K. A. Aly, and F. M. A. Rahim, “Effect of Sn addition on the optical constants of Ge-Sb-S thin films based only on their measured reflectance spectra”, J. Alloys Comp. **561**, 284-290 (2013).

[32] C. -B. Yu, Y. Wu, X. –L. Liu, B. –C. Yao, F. Fu, Y. Gong, Y. –J. Rao, and Y. –F. Chen, “Graphene oxide deposited microfiber knot resonator for gas sensing”, Opt. Mater. Express **6**(3), 727-733 (2016).

[33] B. Mehta, K. D. Benkstein, S. Semancik, and M. E. Zaghloul, “Gas sensing with bare and graphene-covered optical nano-antenna structures”, Sci. Rep. **6**, 21287 (2016).

[34] S. A. Zangana, M. Iliut, G. Boran, M. Turner, A. Vijayaraghavan, and I. Dierking, “Dielectric spectroscopy of isotropic liquids and liquid crystal phases with dispersed graphene oxide”, Sci. Rep. **6**, 31885 (2016).

# CHAPTER 6. TUNABLE MID-INFRARED OPTICAL RESONATOR ON NANOPATTERNED CHALCOGENIDE GLASSES

A paper presented in SPIE Optics and Photonics Conference

Shawana Tabassum, Liang Dong, and Ratnesh Kumar

## 6.1 Abstract

We present the incorporation into the chalcogenide glasses of two-dimensional periodic nanopatterns to realize the first of a kind chalcogenide-based planar optical mid-infrared tunable resonant structure. Chalcogenide (ChG) glasses are promising for infrared photonics owing to their transparency in visible to far infrared, where various biomolecules and gases have their characteristic absorption lines, arising from rotational-vibrational transitions. The region of the electromagnetic spectrum in which this absorption occurs, the amount of absorption, and the specific characteristics of the absorption curve are unique to each gas. Thus, gases can be fingerprinted using their absorption characteristics. Utilizing the mid-IR resonance feature of our nanopatterned ChG glass, an innovative approach is proposed to achieve selective gas sensing through the tuning of the sensor resonance, providing an inbuilt selectivity. As an illustration, the presented chalcogenide-based nanostructure is customized to match its resonance wavelength with the absorption band of gaseous methanol, a key plant health indicator. The highly concentrated electromagnetic field at the nanostructure surface allows highly sensitive detection of the target analyte methanol.

## 6.2 Introduction

Analysis of the composition and concentration of gas mixtures is crucial to environmental as well as health monitoring (eg, in agriculture, animal farms, hospitals, humans). Likewise, analysis of biofluids is essential for point-of-care diagnosis. Recently,

Fourier transform infrared (FTIR) and Raman spectroscopy are increasingly being utilized for bio as well as gas analysis [1], [2]. With the advent of quantum cascade lasers (QCL) spectroscopy, broadband light sources such as FTIR can be replaced with laser operating at a narrow spectral range [3]. However, their widespread in-situ adoption requires their inexpensive miniaturization. In this regard, chalcogenide glasses (ChGs) based photonic structures offer alternatives [4-6], for being transparent over visible to far infrared where various biomolecules and gases have their characteristic absorption lines, having low processing temperatures and suitability for compositional alloying. These materials can be easily embedded into optical sensors to provide extra-ordinary light manipulations in mid-infrared (mid-IR) and depending on the chalcogen element (S, Se, Te) introduced, transparencies can be provided up to 25 μm of the light spectrum [7]. These materials are thus suitable for mid-IR gas sensors as they allow detection of all the gases with absorption signatures lying in this spectral region [8-10].

Certain research has been done on designing ChG based mid-IR gas sensors. Han et al. reported an on-chip spiral ChG glass waveguide coupled with off-chip laser and detector for mid-IR sensing of methane gas [4]. Kim et al. designed a hydrogen gas sensor by depositing ChG nanowires on anodic aluminum oxide templates [11]. In addition, thin films of ChG glasses are also being used for gas sensing applications [12], [13]. However, little research has been done on incorporating chalcogens into optical resonant based nanostructures. A nanoscale and planar optical resonant structure can play a significant role in highly sensitive detection of biomolecules or gas molecules through the interaction of analyte molecules with the highly concentrated EM field at the nanostructure surface. In this regard, we have previously proposed a surface plasmon resonance-based nanostructure on a planar substrate [14-17] and a guided

mode resonance-based nanostructure at the tip of an optical fiber making it practical for remote sensing as an endoscope [18], [19]. These structures do not have inbuilt selectivity to target gas analyte, and instead the varied thicknesses of graphene oxide generated varied sensor response by different amount of gas adsorption [20]. Those responses were fed into a pattern recognition algorithm to differentiate the analyte species in a complex mixture.

In the present work, we report the first of a kind planar mid-IR resonant structure that undergoes enhanced light absorption by the analyte adsorbed on its surface, enabling highly sensitive and selective label-free detection of gas and/or biomarkers. This approach of mid-IR based sensing is label-free, with inbuilt selectivity. Thus, selective detection of gas/biomarker can be achieved in the mid-infrared region of light spectrum since each gas/biomarker exhibits a distinct absorption signature in the near-infrared to far-infrared regime. Here we present the novel design of a nanoscale tunable planar mid-IR optical resonator, realized by solvent-casting of ChGs ($As_2S_3$). The tunability of the resonance is achieved though varying the thickness of the base ChG underneath the nanoposts, a first of its kind. Our technique of preparing nanostructure having tunable resonance at mid-IR enables the realization of mid-IR bio as well as gas sensors. As an application illustration, the design has been customized to enable the selective methanol detection at ~2.6 μm. This work resulted in the publication [21].

## 6.3 Mid-IR Sensor Design and Fabrication

### 6.3.1 Working principle

We have designed a nanoscale tunable mid-IR optical resonant structure, useful for selective monitoring of different analytes. This requires tuning the device resonance to target analyte's absorption band. For example, the gaseous methanol, an important plant health indicator, has an absorption band at ~2.6 μm. Keeping this in mind, we have designed ChG

nanopost structure with the resonance mode at ~2.64 μm, so the proposed ChG device can selectively detect gaseous methanol (through the surface enhanced near-field distribution).

The ChG nanopost structure is shown in Fig. 6.1. The nanopost structure has a square lattice with the pitch of 2 μm and the post diameter of 1 μm. The device is formed using thermal-assisted nanoimprint lithography (NIL). Light transmission through a periodic array of subwavelength diameter posts is influenced by diffractive effects such as Rayleigh anomalies (RA). RAs are spectral features associated with grating and correspond to light being diffracted at a grazing angle. When light is incident on a two-dimensional periodic grating structure at an angle $\theta_i$, the free-space incident wavelength, $\lambda_{RA}$ that excites an RA mode satisfies [22]:

$$\frac{2\pi\sqrt{\varepsilon_d}}{\lambda_{RA}} = \sqrt{\left[\left(2\pi\frac{\sin\theta_i}{\lambda_{RA}} + i\frac{2\pi}{\Lambda}\right)^2 + \left(j\frac{2\pi}{\Lambda}\right)^2\right]} \tag{6.1}$$

where, (i,j) is an integer pair that corresponds to a particular RA mode, $\Lambda$ is pitch of the grating and $\varepsilon_d$ is dielectric constant of the surrounding medium. The above equation is most accurate when the grating is thick enough that there is no coupling of resonances on the two sides of the grating [22]. However, depending on the thickness of the grating, RA modes on the two sides of the grating interact with each other. Such interaction red or blue-shifts the position of RA mode slightly, relative to Equation (6.1). McMahon et al. has studied this resonance coupling phenomena in detail [22]. For a nanopost structure with $\Lambda$ = 2μm, $\theta_i = 40^0$, and $\varepsilon_d$ =1, the first order (i,j) = (1,0) RA mode is calculated as 2.5 μm from Eqn. (6.1). The experimentally observed RA mode is found at 2.64 μm for the same structure (details appear in Results and Discussion) with a grating thickness of t = 350 nm (Fig. 6.1). Thus, the experimental resonance

is red-shifted with respect to the calculated value of 2.5 μm, as anticipated by the aforementioned coupling. As the thickness t varies, the position of RA mode also varies, relative to the value given by (6.1). Also, as is evident from Eqn. (6.1), variation in the refractive index of the surrounding medium (i.e. $\varepsilon_d$ variation), causes the RA resonance wavelength, $\lambda_{RA}$ to shift. Thus, the sensor is capable of detecting changes in ambient refractive indices, caused by the adsorption of the analyte gases.

### 6.3.2 Sensor fabrication

All operations are carried out under an atmosphere of purified nitrogen inside a glove box. The presented ChG nanoposts is fabricated using thermal-assisted NIL. The $As_2S_3$ glass powder is first mixed into ethanolamine solvent at a concentration of 0.5 g/ml. The mixture is stirred using a magnetic stirrer at 500 rpm and at a constant temperature of $65^0$ C, and stored in dark until complete dissolution takes place. Simultaneously a soft PDMS mold is created from a silicon (Si) master mold carrying the mask for nanoposts with a period of 2 μm, nanopost diameter of 2 μm and nanopost height of 400 nm using soft lithography-based nanoreplica molding process (Fig. 6.1a). A Si wafer is next coated with a 15-nm gold (Au) layer (Fig. 6.1b) using electron beam deposition to promote strong adhesion with $As_2S_3$ through the formation of Au-S bonds at the interface. Next, the prepared $As_2S_3$ solution is spin coated at 5000 rpm for 40 s over the Au coated Si wafer, and the PDMS mold is pressed against the Si wafer. The entire assembly is annealed in vacuum in three steps, a soft-bake at $70^0$ C for 1 hour, a hard-bake at $90^0$ C for 1 hour, followed by annealing at $110^0$ C for 8 hours (Fig. 6.1c). Finally, the separation of the PDMS mold from the Si wafer results in $As_2S_3$ nanoposts transferred to the Si wafer (Figs. 6.1d-e).

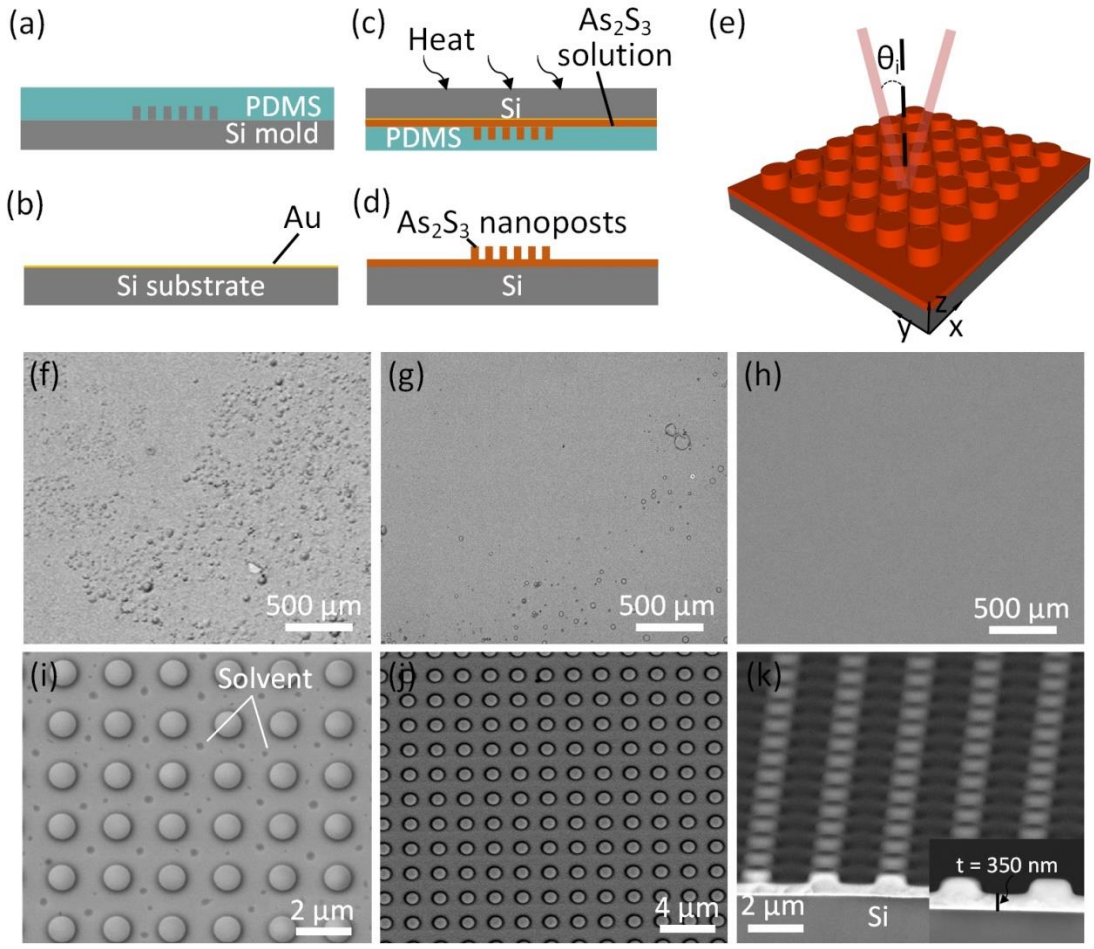


Fig. 6.1: *(a)-(d) Step-wise representation for the fabrication of $As_2S_3$ 2D nanoposts structure; (e) Schematic representation of the $As_2S_3$ 2D nanopatterns, with $\theta_i$ being the angle of incident light; (f)-(h) Top-view SEM image of solution processed $As_2S_3$ film prepared under different conditions: (f) Roughness in $As_2S_3$ film generated by fast annealing ($170^0$ C) in vacuum, (g) Crystal formation upon annealing ($170^0$ C) in air, (h) A smooth, defect free film formed with three step annealing process in vacuum; (i)-(k) Solution processed $As_2S_3$ 2D nanopatterns fabricated under different conditions: (i) Solvent molecules are trapped between nanoposts due to high temperature annealing ($170^0$ C) in air, (j) Smooth, uniform nanoposts formed with three step annealing in vacuum, (k) A perspective view of the structure in (j), where the inset shows the thickness t = 350 nm of the base $As_2S_3$ beneath the nanoposts.*

## 6.4 Materials and Methods

### 6.4.1 Chemicals and materials

184 Silicone elastomer kit was purchased from Dow Corning Cop., MI, USA which was used to prepare PDMS solution. $As_2S_3$ powder (99.999%) was obtained from VWR Scientific, PA, USA and ethanolamine was purchased from Sigma-Aldrich, MO, USA. The

silicon master mold carrying the nanopatterns was fabricated by Minnesota Nano Center, Minneapolis, MN, USA.

### 6.4.2 Optical measurements

For optical measurements Fourier transform infrared (FTIR) spectroscopy was used in the reflectance mode.

## 6.5 Results and Discussion

The fabricated $As_2S_3$ nanopatterns are imaged using scanning electron microscopy (SEM). The planar $As_2S_3$ films prepared under different annealing conditions are compared (Figs. 6.1f-h). Fast annealings at high temperature contain defects such as surface roughness and $As_2O_3$ crystals. Similarly, Figs. 6.1i-k confirm that high temperature annealing in air results in solvent molecules trapped between the nanoposts in $As_2S_3$ nanopost structure. In contrast, the aforementioned three-step annealing process in vacuum provides the best result. The higher peaks of C, N and O in the energy dispersive spectroscopy (EDS) analysis demonstrated in Fig. 6.2a indicate the presence of trapped solvent in the nanostructure annealed in air (Fig. 6.1i). No such anomaly exists for the nanopost-structure prepared in vacuum using our 3-step annealing.

The nanostructured thin film is further characterized using UV-vis and Raman spectroscopy as illustrated in Figs. 6.2b-c. These further reveal that when the solution is coated at a higher spin rate, the spacing between the fringes in the transmission spectrum decreases, confirming the decrease in film thickness with spin rate (Table 6.1). The main band at 350 $cm^{-1}$ in the Raman spectrum is attributed to the vibrations of $AsS_{3/2}$ pyramidal units due to the asymmetric stretches of $AsS_3$ units [23].

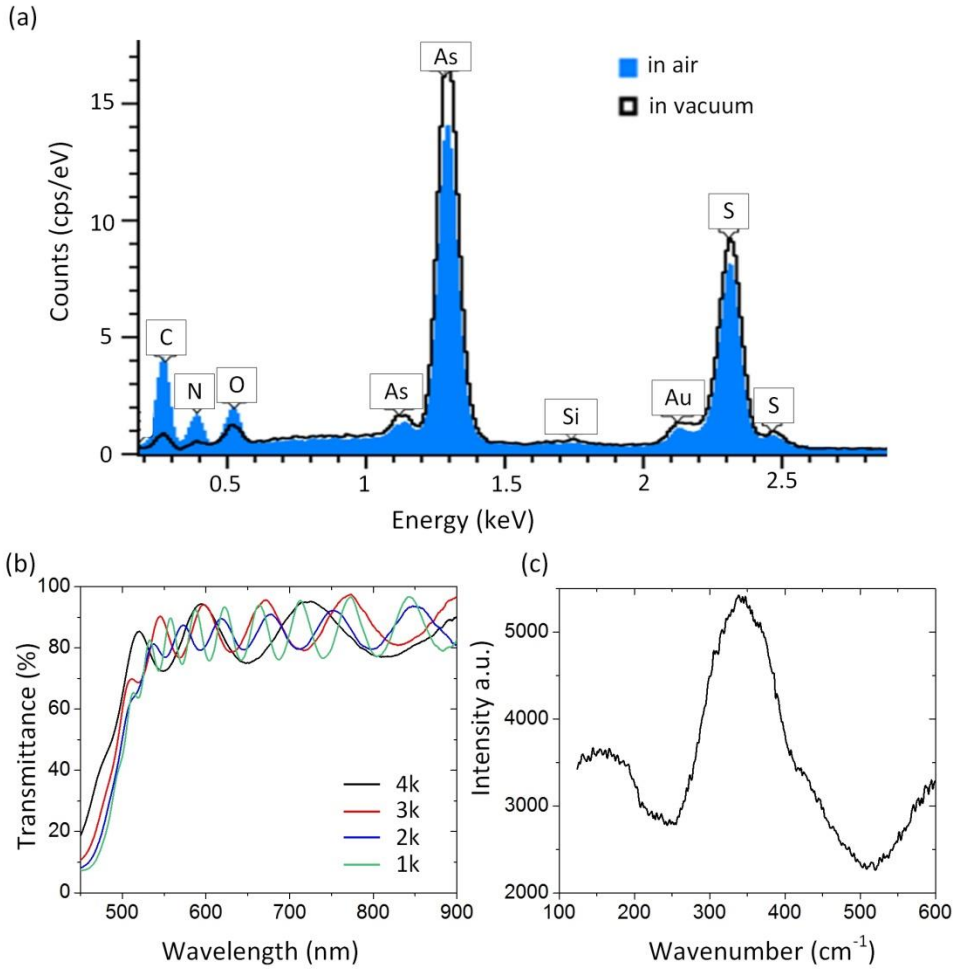


Fig. 6.2: *(a) Comparison of the EDS spectra of $As_2S_3$ nanopatterns fabricated in air and in vacuum; (b) Transmission spectra of solution processed $As_2S_3$ film in visible spectrum with varying spin speed; (c) Raman spectrum of the $As_2S_3$ film.*

IR spectroscopy (Fig 6.3a) is used to evaluate the presence of the common impurities (carbon, oxygen, hydrogen). The broad feature near 2850 nm corresponds to the –OH group, bonded as in As-OH or staying free as in interstitial $H_2O$. The absorption band in the range 3100-3583 nm is due to N-H stretch and aliphatic C-H stretches, indicating the presence of residual solvent in the film [23], [24]. The $As_2S_3$ nanoposts structure exhibits a RA mode that depends on incidence angle $\theta_i$, grating period $\Lambda$, and thickness t of $As_2S_3$ beneath the nanoposts (Fig. 6.1k). For a nanopost structure with $\theta_i = 40^0$, $\Lambda = 2$ μm and t = 350 nm, the experimentally

observed RA mode is at 2.64 µm. Figure 6.3b shows that a tunable mid-infrared optical resonator is realized by varying the thickness t.

The near-field distributions of the resonance mode in the xz-plane at 2.64 µm are calculated using the rigorous coupled wave analysis (RCWA). Fig. 6.3c shows the maximum field enhancement factor of 2.5.

Table 6.1. *Variation of $As_2S_3$ film thickness with spin speed.*

| **Spin Speed (rpm)** | 1000 | 2000 | 3000 | 4000 |
|---|---|---|---|---|
| **Film Thickness (nm)** | 2200 | 1400 | 900 | 500 |

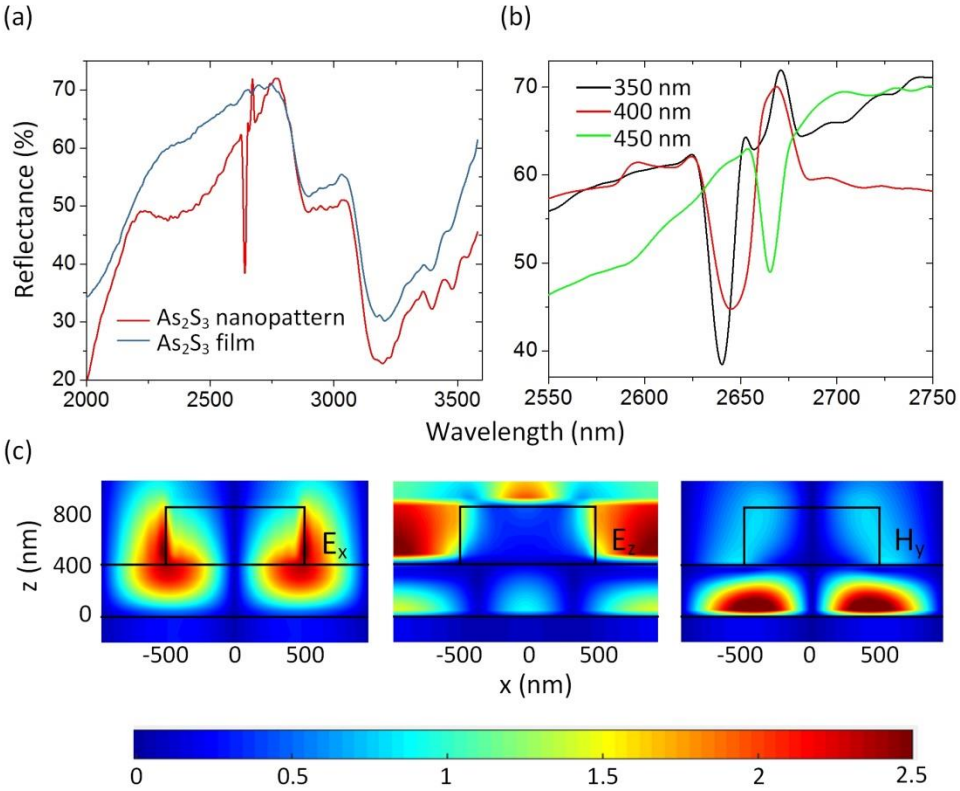


Fig. 6.3: *(a) Measured reflection spectra of the $As_2S_3$ film and 2D nanopatterns; (b) Resonance tuning of the 2D nanopatterns by varying the $As_2S_3$ thickness t beneath the nanoposts; (c) Near-field distribution of the $E_x$, $E_z$ and $H_y$ components when $\lambda_{RA}$ = 2.64 µm and $\theta_i = 40^0$.*

## 6.6 Conclusion and Future Work

In this work, we reported a first of a kind nanoscale, tunable and planar mid-IR optical resonator incorporating chalcogenide glasses. For selective detection, the nanostructure is customized to match its own resonance with the absorption-band of a target gas, namely, methanol. Future work will be directed to utilizing the proposed ChG nanostructure and functionalize it for interaction with target gas and measure the corresponding absorbance variation. This will require coating the nanopost structure with a gas absorption layer. For gas sensing, we will place the ChG nanopost structure in an enclosed chamber having windows transparent to IR light. We will build an optical setup wherein an IR laser or LED source will be used to shine light on the sensor surface and the reflected/transmitted light will be detected by an IR photodetector. We will also explore resonance enhancement by integrating localized surface plasmon resonance or GMR with the ChG nanopost structure. The exploration to a certain target gas sensing in a mixture and other applications of the proposed structure (by tuning the device to analytes' absorption band) will be explored.

## 6.7 References

[1] Patel, I.I., Harrison, W.J., Kerns, J.G., Filik, J., Wehbe, K., Carmichael, P.L., Scott, A.D., Philpott, M.P., Frogley, M.D., Cinque, G. and Martin, F.L., "Isolating stem cells in the inter-follicular epidermis employing synchrotron radiation-based Fourier-transform infrared microspectroscopy and focal plane array imaging", Anal. Bio. Chem. 404 (6-7), 1745-1758 (2012).

[2] Lloyd, G.R., Orr, L.E., Brown, J.C., McCarthy, K., Rose, S., Thomas, M. and Stone, N., "Discrimination between benign, primary and secondary malignancies in lymph nodes from the head and neck utilizing Raman spectroscopy and multivariate analysis", Analyst 138, 3900-3908 (2013).

[3] Razeghi, M., Slivken, S., Bai, Y. and Darvish, S. R., "Quantum cascade laser: a versatile and powerful tool", Opt. Photon. News 19, 4247 (2008).

[4] Han, Z., Lin, P., Singh, V., Kimerling, L., Hu, J., Richardson, K., Agarwal, A. and Tan, D.T.H., "On-chip mid-infrared gas detection using chalcogenide glass waveguide", Appl. Phys. Lett. 108, 141106 (2016).

[5] Hu, J., Carlie, N., Feng, N.N., Petit, L., Agarwal, A., Richardson, K. and Kimerling, L., "Planar waveguide-coupled, high-index-contrast, high-Q resonators in chalcogenide glass for sensing", Opt. Lett. 33(21), 2500-2502 (2008).

[6] Sanghera, J. S. and Aggarwal, I. D., "Active and passive chalcogenide glass optical fibers for IR applications: a review", J. Non-Crystalline Solids 256-257, 6-16 (1999).

[7] Starecki, F., Charpentier, F., Doualan, J. -L., Quetel, L., Michel, K., Chahal, R., Troles, J., Bureau, B., Braud, A., Camy, P., Moizan, V. and Nazabal, V., "Mid-IR optical sensor for $CO_2$ detection based on fluorescence absorbance of $Dy^{3+}$: $Ga_5Ge_{20}Sb_{10}S_{65}$ fibers", Sens. Actuators B Chem. 207, 518-525 (2015).

[8] Ari, J., Starecki, F., Pledel, C. B., Doualan, J. L., Quetel, L., Michel, K., Braud, A., Camy, P., Chahal, R., Bureau, B., Ledemi, Y., Messaddeq, Y. and Nazabal, V., "Rare-earth doped chalcogenide glasses for mid-IR gas sensor applications", SPIE 10100 (2017).

[9] Shaw, L. B., Cole, B., Thielen, P. A., Sanghera, J. S. and Aggarwal, I. D., "Mid-wave IR and long-wave IR laser potential of rare-earth doped chalcogenide glass fiber", J. Quantum Electron. 48(9), 1127-1137 (2001).

[10] Kubat, I., Petersen, C. R., Moller, U. V., Seddon, A., Benson, T., Brilland, L., Mechin, D., Moselund, P. M. and Bang, O., "Thulium pumped mid-infrared 0.9-9 μm supercontinuum generation in concatenated fluoride and chalcogenide glass fibers", Opt. Express 22(4), 3959-3967 (2014).

[11] Kim, S., Lee, Y. I., Choi, Y. M., Lim, H. R., Lim, J. H., Myung, N. V. and Choa, Y. H., "Thermochemical hydrogen sensor based on chalcogenide nanowire arrays", Nanotechnology 26, 145503 (2015).

[12] Georgieva, V., Yordanov, Tz., Pamukchieva, V., Arsova, D., Gadjanova, V. and Vergov, L., "Gas sensing properties of Ge-As-S thin films", Proc. AIP Conf. 1203, 1079 (2010).

[13] Dmitriev, S. V. and Dementiev, I. V., "Vitreous chalcogenide semiconductors for gas sensing application", Proc. Mater. Res. Soc. Symp. 828 (2005).

[14] Tabassum, S., Wang, Q., Wang, W., Oren, S., Ali, M. A., Kumar, R. and Dong, L., "Plasmonic crystal gas sensor incorporating graphene oxide for detection of volatile organic compounds," Proc. IEEE Int. Conf. Micro Electro Mech. Syst. (MEMS), Shanghai, China, 913-916 (2016).

[15] Tabassum, S., Kumar, R. and Dong, L., "Plasmonic crystal-based gas sensor toward an optical nose design", IEEE Sens. J. 17(19), 6210-6223 (2017).

[16] Ali, M. A., Tabassum, S., Wang, Q., Wang, Y., Kumar, R. and Dong, L., "Plasmonic-electrochemical dual modality microfluidic sensor for cancer biomarker detection", Proc.

IEEE Int. Conf. Micro Electro Mech. Syst. (MEMS), Las Vegas, NV, USA, 390-393 (2017).

[17] Ali, M. A., Tabassum, S., Wang, Q., Wang, Y., Kumar, R. and Dong, L., "Integrated dual-modality microfluidic sensor for biomarker detection using lithographic plasmonic crystal", Lab Chip 18(5), 803-817 (2018).

[18] Tabassum, S., Wang, Y., Qu, J., Wang, Q., Oren, S., Weber, R. J., Lu, M., Kumar, R. and Dong, L., "Patterning of nanophotonic structures at optical fiber tip for refractive index sensing", Proc. IEEE Sensors, Orlando, FL, USA, 1-3 (2016).

[19] Tabassum, S., Kumar, R. and Dong, L., "Nanopatterned optical fiber tip for guided mode resonance and application to gas sensing", IEEE Sens. J. 17(22), 7262-7272 (2017).

[20] Tabassum, S., Dong, L. and Kumar, R., "Determination of dynamic variations in the optical properties of graphene oxide in response to gas exposure based on thin-film interference", Opt. Express 26(5), 6331-6344 (2018).

[21] Tabassum, S., Dong, L. and Kumar, R., "Tunable mid-infrared optical resonator on nanopatterned chalcogenide glasses", in Proc. Infrared Sensors, Devices, and Applications VIII, San Diego, CA, USA, 10766 (2018).

[22] McMahon, J. M., Henzie, J., Odom, T. W., Schatz, G. C. and Gray, S. K., "Tailoring the sensing capabilities of nanohole arrays in gold films with Rayleigh anomaly-surface plasmon polaritons", Opt. Express 15(26), 18119-18129 (2007).

[23] Carlie, N., "A solution-based approach to the fabrication of novel chalcogenide glass materials and structures", All Dissertations 554 (2010).

[24] Song, S., [Solvent-casting of chalcogenide glasses and their applications in mid-infrared optics], Princeton Univ., (2011).

# CHAPTER 7. CONCLUSIONS AND OUTLOOK

## 7.1 Conclusions

The main contribution of this thesis is to develop cost-effective, simple and tunable novel optical sensors at nanoscale and demonstrate them for gas sensing applications. This is not only relevant for the advancement of the "Internet-Of-Things (IoT) world", but this research in the specific field of optical sensor design is important because of the increased scientific interest to establish a noninvasive, high-resolution and high-quality miniature evaluation system to assure a healthy ecosystem whether for agricultural food production or water quality or health and hygiene. The fiber-optic sensor is flexible and portable, thus allowing remote in-field measurements in biomedical, environmental, agricultural, and other applications. Based on the literature review, the pros and cons described in recent studies have been determined and a new perspectives of optical resonant nanostructures for gas sensing applications are proposed. The investigations described in this thesis are related to concepts of flexible gas sensors fabrication on nanopatterned substrates in the visible to infrared region of EM spectrum.

Chapter 2 describes a graphene oxide (GO) coated plasmonic crystal based novel gas sensor that is demonstrated to detect as well as differentiate plant volatiles in ppm levels. The gas adsorption of GO modifies the refractive index of the plasmonic structure and returns a shift in the resonance wavelength of the surface plasmon polariton excited at the GO coated plasmonic surface. An array of sensors is also developed and PCA algorithm is used to analyze the shifts and differentiate different gas species.

Chapters 3 and 4 describe a new gas sensor developed on the tip of a fiber optic cable, which can be easily inserted into hard to access remote sensing areas. The GMR sensing structure that has been integrated on a fiber tip is the very first one that allows producing fiber-

optic remote sensors for biomedical, environmental, industrial applications. This fiber-optic sensor is demonstrative of the necessity of remote sensing to best monitor gases/biomarkers in regions otherwise inaccessible. This miniaturized fiber-optic probe opens the possibilities for point-of-care diagnosis of diseases. The inherent light guiding property of optical fiber over long distances, its microscopic cross-section that has been structured to manipulate the light at nanoscale, mechanical flexibility, and low cost make the fiber-tip sensor suitable for label-free point-of-care diagnostics.

Chapter 5 describes the characterization of the dynamic evolution of the RI values of a GO thin film in response to exposure to a gas by the method of thin-film interference.

Chapter 6 describes work on improving specificity of the above mentioned sensors. We have proposed an innovative approach to achieve specificity through modification of the sensor structure. The plant volatiles will be detected selectively in the near-infrared region of electromagnetic spectrum since each gas exhibits a distinct absorption signature in the near-infrared to far-infrared regime. With this observation, the use chalcogenide, having a broad transparency window in infrared (1-20μm), has been proposed as the core material of a two-dimensional micro-patterned resonant structure. Selective detection of a gas can be achieved through customizing the nanostructures to match its resonant wavelength with the absorption band of the particular gas.

## 7.2 Outlook

The future prospects of nanostructure-based gas sensing include, in-filed measurement capabilities, improving the information obtained from sensors (i.e., sensitivity, wider dynamic range, multifunctional sensing ability), and IoT application doamins. For all developed sensors in this thesis, the sensor was illuminated by a white light source and detection was done using a spectrometer. Future work can include the development of a system suitable for in-field

application wherein the white light source and spectrometer may be replaced with an LED source and a CMOS image sensor or a diode photodetector. The methods introduced in this thesis can also be utilized in the fabrication of different types of functional materials-based sensors on different substrates to expand the range of possible IoT applications including bio-sensing, which are promising emerging areas.

### 7.3 Acknowledgements

This work was supported by the US National Science Foundation under the grants CCF-1331390 and IIP-1602089, and a Regents Innovation Fund at the Iowa State University. The authors thank Yifei Wang for assistance with initial simulation, Seval Oren for running the SEM, Qiugu Wang for inputs on GMR understanding, Md Azahar Ali for inputs on paper organization, Jikang Qu for help with cutting the fiber tip, Prof. Meng Lu for inputs on optical measurement setup and modeling discussion, and Prof. Robert J. Weber on sensor related discussions. All the above names are affiliated with the Iowa State University, Department of Electrical and Computer Engineering.

# APPENDIX. SUPPORTING INFORMATION

## Fabrication of Plasmonic Nanopost Array

The sensor fabrication steps are shown in Fig. A.1. The fabrication starts with a silicon (Si) master mold (Fig. A.1a). In order to form a PDMS mold from Si master mold we followed two steps. At first the Si master mold carrying the nanopatterns was silanized with (tridecafluoro-1, 1, 2, 2- tetrahydrooctyl)-1-trichlorosilane (T2492-KG, United Chemical Technologies) in a desiccator under active vacuum for 20 min. Then, a mixture of poly (7-8% vinylmethyl- siloxane)- (dimethylsiloxane) (Gelest # VDT-731), (1, 3, 5, 7-tetravinyl-1, 3, 5, 7-tetramethylcyclotetrasiloxane) (Gelest # SIT7900.0), platinum catalyst Xylene (Gelest # SIP6831.2) and poly (25-30% methylhydro-siloxane)- (dimethylsiloxane) (Gelest # HMS-301) at the weight ratio of 3.4: 0.1: 0.05: 1 was prepared that worked as an h-PDMS precursor solution. Next, the mixture was put in a degassing chamber for 10 min to remove the air bubbles and was then spin-coated onto the Si mold at 1000 rpm for 40 s and cured at 70$^{o}$C for 10 min. Subsequently, an s-PDMS precursor solution was prepared by mixing Sylgard 184 (Dow Corning) and curing agent at the weight ratio of 10: 1 and degassed in a vacuum desiccator for 20 min. After that, the s-PDMS mixture was poured onto the top surface of h-PDMS and cured on a hotplate at 65$^{o}$C for 2 hrs (Fig. A.1b). Finally, the PDMS slab containing a square array of nanoholes was peeled from the Si mold (Fig. A.1c).

The next step was to use a UV curable polymer (ZIPCONE™ UA or ZPUA) to imprint the nanoposts from the PDMS mold to a Si wafer [Fig. A.1(d-e)]. At first, the Si wafer was spin coated with an adhesive layer of Transpin at 3000 rpm for 40s and subsequently heated at 200 $^{0}$C for 5 min. This step is required to enhance the adhesion ability of ZPUA to Si wafer resulting in complete transfer of ZPUA nanoposts to the Si wafer. The ZPUA was dropped on

the PDMS mold (Fig. A.1d) and the mold was then placed on top of the Si wafer. Then the wafer was exposed to ultraviolet light for 5 min at an intensity of 3.3 $mW/cm^2$ (Fig. A.1e). Separation of the PDMS mold from the Si wafer resulted in nanoposts transferred to the Si wafer which was further coated with a 50 nm Au layer using e-beam evaporation.

Aqueous suspensions of GO nanosheets (2 mg/mL) were prepared by thoroughly dispersing 2 mg of the synthesized GO nanosheet flakes (purchased from Graphene Supermarket) in 1 mL of deionized water, followed by sonication at room temperature for 90 min. This solution was then diluted to make three different GO dispersion solutions (0.05 mg/ml, 0.1 mg/ml and 0.15 mg/ml). The surfaces of the three sensors were made hydrophilic by using oxygen plasma treatment before drop-coating with different amounts of GO solutions. For each coating, 100 $\mu L/cm^2$ of GO suspensions were drop coated over the sensor surface. These sensors were then dried at room temperature for one hour. The final structure is shown in Fig. A.1f.

**PCA Algorithm**

The PCA algorithm was employed to find clusters in a given dataset by projecting a feature space onto a smaller subspace with minimal loss of information. The steps for performing PCA are listed below:

1. The entire dataset consisting of an $m \times n$ matrix is taken as input for the PCA analysis. In our case, we had a $9 \times 3$ matrix consisting of the values of resonance wavelengths for three different concentrations of ethylene, methanol and $NH_3$ vapors and three different thicknesses of GO as given in Table 1.
2. The mean values are computed for each row of the entire dataset. Suppose for the $m \times$

*n* dataset, the $i^{th}$ row is given by, $x_{i1}, x_{i2}, x_{i3}, \ldots\ldots\ldots, x_{ij}, \ldots\ldots\ldots, x_{in}$. Then, the mean value along the $i^{th}$ row is calculated as follows:

$$\mu_i = \frac{1}{n}\sum_{j=1}^{n} x_{ij}.$$

3. The row mean value is subtracted from all values in the row. i.e., each $x_{ij}$ is replaced with $x_{ij} - \mu_i$. Suppose we thus get a new $m \times n$ matrix, denoted *D*.

4. The covariance matrix of the whole dataset is computed. The samples for the *m* observations (the concentrations) for the *n* variables (the thicknesses) are used to compute an $n \times n$ covariance matrix $C$, whose $jk^{th}$ entry is given by,

$$c_{jk} = \frac{1}{m-1}\sum_{i=1}^{m}\left(D_{ij} - \overline{D_j}\right)\left(D_{ik} - \overline{D_k}\right).$$

Here $D_{ij}$ is the $ij^{th}$ element of matrix, and $\overline{D_j}$ is the mean value of matrix *D* along the $j^{th}$ column.

5. The eigenvectors and the corresponding eigenvalues of the covariance matrix, $C$ are computed.
6. The eigenvectors are sorted by decreasing eigenvalues. Let, *W* be an $n \times n$ matrix wherein the columns represent eigenvectors, sorted in the descending order of eigenvalues.
7. The matrix *W* is used to transform the samples using,

$$y = WD^T,$$

where *y* is the transformed $n \times m$ dimensional sample in the new space.

8. Finally, the first *k* rows of the matrix *y* are chosen that correspond to first *k* eigenvectors with the largest eigenvalues. (For our case $k = 3$ since three gases in the mixture.)

Following the steps 1-8 described above, the matrix in Table A.1 was reduced to the two principal components PC1, PC2 as plotted in Fig. 2.9. The plot clearly shows three different separated clusters for the three gas species.

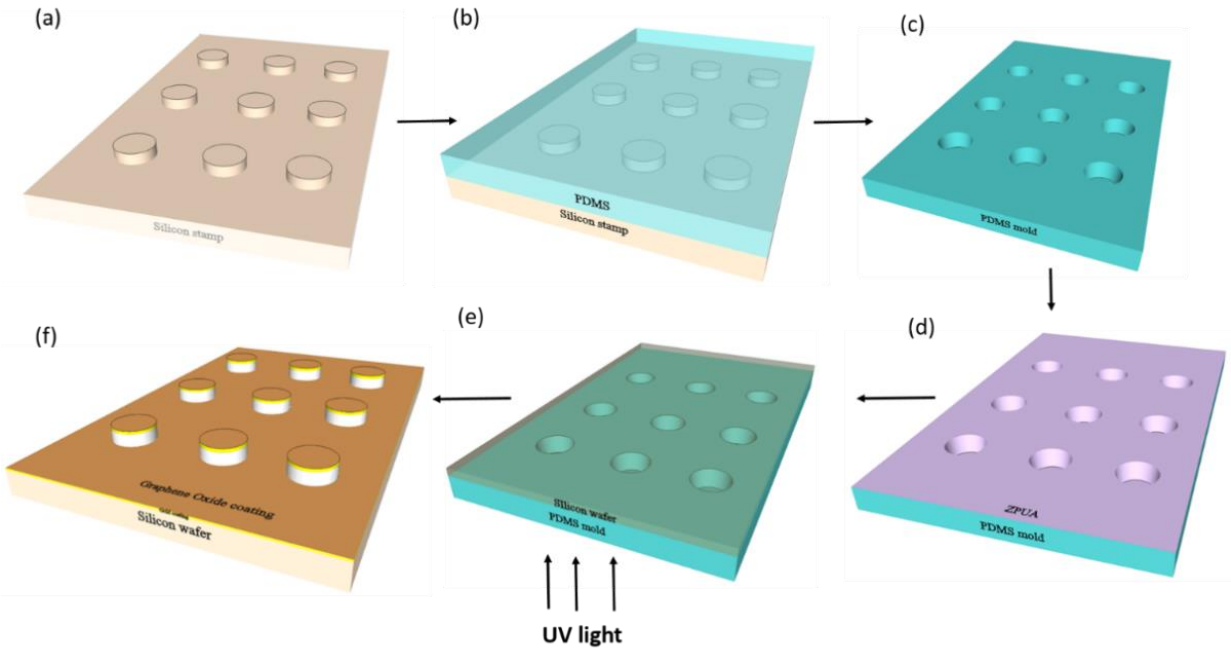


Fig. A.1. *Fabrication process of GO coated plasmonic crystal sensor. (a) Si master mold carrying nanoposts with period (ʌ=500 nm), diameter (d=250 nm), and height (h=210 nm). (b) PDMS is poured on the Si stamp. (c) PDMS is peeled off the stamp. (d) ZPUA is poured on the PDMS mold. (e) The PDMS mold is pressed against the Si wafer and exposed to UV radiation. (f) 50 nm gold coating followed by GO coating on the device.*

Table A.1. *Data matrix input to PCA algorithm*

| Concentration / Gas species | Optical Resonance Wavelength (nm) | | |
|---|---|---|---|
| | 16.3 nm-thick GO | 32.6 nm-thick GO | 48.9 nm-thick GO |
| 250 ppm / Methanol | 550.41 | 551.50 | 553.17 |
| 333.33 ppm / Methanol | 550.63 | 551.57 | 553.24 |
| 375 ppm / Methanol | 550.83 | 551.60 | 553.31 |
| 500 ppm / Ethylene | 550.87 | 555.80 | 556.40 |
| 666.66 ppm / Ethylene | 550.93 | 556.00 | 556.50 |
| 750 ppm / Ethylene | 550.95 | 556.20 | 556.75 |
| 100 ppm / Ammonia | 551.14 | 552.55 | 554.29 |
| 117 ppm / Ammonia | 551.31 | 552.59 | 554.30 |
| 120 ppm /Ammonia | 551.42 | 552.68 | 554.33 |

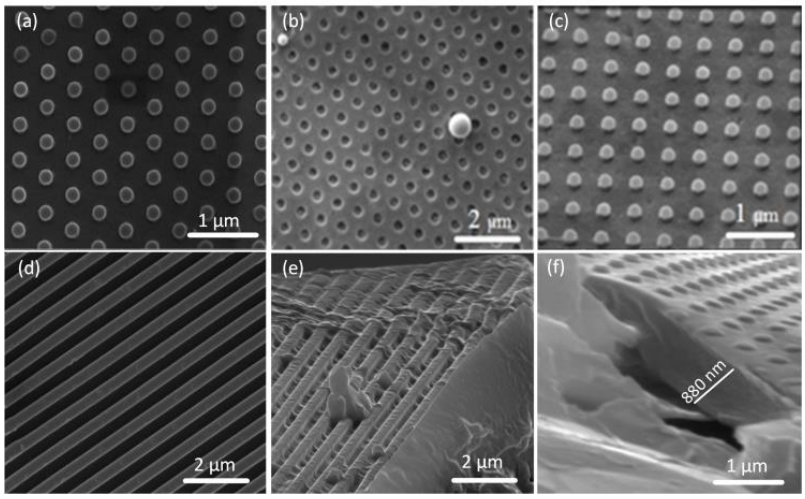


Fig. A.2: *To demonstrate reproducibility of our approach and also to conduct structural optimization for the purposes of sensing, different nanopatterns were formed at the fiber tip: (a) nanoposts with a triangular lattice (b) nanoholes with a triangular lattice, (c) nanoposts with a square lattice, (d) linear nanostamps. (e) $75^0$ side-view of the linear stamps, (f) $75^0$ side-view of nanoposts with square lattice showing the remaining polymer (SU8) thickness underneath the nanoposts.*

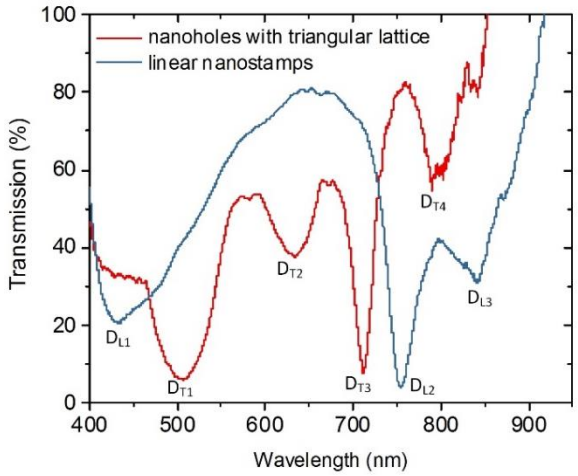


Fig. A.3: *Characterization of the alternative design structures, namely, transmittance spectra of nanoholes with a 2D triangular lattice and 1D linear nanostamps at the fiber tip coated with 160 nm of $TiO_2$. Notations $D_{T1} – D_{T4}$ and $D_{L1} – D_{L3}$ represent different modes excited at 2D triangular lattice and 1D linear nanostamps respectively.*